

**Utilization of UARS data in Validation of Photochemical and Dynamical
Mechanisms in Stratospheric Models**

Contract NAS5-32844

1/10/98
2/10/98

Appendix

Danilin, M.Y., et al. (1998) "Stratospheric cooling and Arctic ozone recovery"
Geophy. Res. Lett., **25** (12): 2141-2144

Danilin, M.Y., et al. (1998) "Trajectory hunting: Analysis of UARS
measurements showing rapid chlorine activation"

Danilin, M.Y., et al. (1998) "Nitrogen species in the post-Pinatubo stratosphere:
Model analysis utilizing UARS measurements"

**Utilization of UARS data in Validation of Photochemical and Dynamical
Mechanisms in Stratospheric Models**

Contract NAS5-32844

by

**Malcolm K. W. Ko, Jose M. Rodriguez, Wenjie Hu,
Michael Y. Danilin and Run-Li Shia
Atmospheric and Environmental Research, Inc.
840 Memorial Drive, Cambridge, MA 02139**

for

**NASA Goddard Space Flight Center
Greenbelt, MD 20771**

November 1998

Table of Contents

Executive Summary	1
Introduction and Overview	5
(I) Monthly zonally mean files of HALOE and CLAES data	6
(II) Using species correlation to obtain NO _y	7
(III) NO _y partitioning and Pinatubo aerosol	11
(IV) Utilization of HALOE data to calculate zonal-mean ozone production and loss rates in the lower and middle stratosphere	23
(V) Utilization of UARS data to analyze effects of stratospheric cooling and Arctic ozone recovery.	29
(VI) Trajectory mapping	31
(VII) Trajectory hunting: Analysis of UARS measurements showing rapid chlorine activation	34
(VIII) Wave structure of tracers, use of UARS 3B data	36
(IX) References	42

Appendix:

Danilin, M.Y., et al. (1998) "Stratospheric cooling and Arctic ozone recovery" *Geophys. Res. Lett.*, **25** (12): 2141-2144

Danilin, M.Y., et al. (1998) "Trajectory hunting: Analysis of UARS measurements showing rapid chlorine activation"

Danilin, M.Y., et al. (1998) "Nitrogen species in the post-Pinatubo stratosphere: Model analysis utilizing UARS measurements"

Executive Summary

The proposed work utilized Upper Atmosphere Research Satellite (UARS) measurements of short-lived and long-lived species, in conjunction with existing photochemical “box” models, trajectory models, and two-dimensional global models, to elucidate outstanding questions in our understanding of photochemical and dynamical mechanisms in the stratosphere. Particular emphasis was given to arriving at the best possible understanding of the chemical and dynamical contributions to the stratospheric ozone budget. Such understanding will increase confidence in the simulations carried out by assessment models.

Specific goals of this project were as follows:

1. To acquire UARS data, incorporate it into our database, and examine this data in the context of both model results and possible overlap with other available aircraft, ground-based, balloon-borne and satellite measurements, in order to select specific data time periods to carry out detailed studies.

2. To carry out photochemical studies utilizing as much of the data as possible. These studies place particular emphasis on the implications of UARS data to our understanding of chlorine and nitrogen species partitioning and budget; vertical latitudinal, and seasonal characterization of heterogeneous chemistry; impact of Pinatubo eruption on stratospheric ozone, HNO_3 and NO_x as a function of altitude; and derivation of an altitude-dependent photochemical ozone budget consistent with UARS data.

3. To compare and constrain ongoing dynamical parameterizations in 2-D models with UARS data on long-lived species, with particular emphasis on simulating the apparent transport barriers across the polar vortices and subtropics, and time constants for advection and mixing at mid-latitudes; to utilize these studies in deriving the transport contribution to the ozone budget.

The principal findings of our work are as follows:

- We created a merged UARS data set containing the zonally-averaged stratospheric trace species on daily, monthly and yaw-averaged (i.e. during the 36-day yaw cycle) bases for measurements from the HALOE and CLAES instruments. Special averaged sets have been created taken into consideration the different viewing geometries of HALOE and CLAES. In these sets, CLAES measurements are taken only if they are within 5° of latitude and from a HALOE observation on the same day.
- Daily binned data of almost-coincident HALOE and CLAES measurements have been used to examine the correlations of N₂O with CH₄ and NO_y. The obtained correlations have also been compared to those obtained from ATMOS measurements, and the AER 2-D model results. We find that, in general, all correlations agree fairly well for N₂O mixing ratios greater than 100 ppbv, although the ATMOS and UARS methane are somewhat larger than the 2-D model results for a given N₂O mixing ratio. The “bend” in the NO_y vs. N₂O mixing ratio for [N₂O] < 100 ppbv is also in fairly good agreement with data. Due to limited sampling and large data scatter, it is not possible to extract latitudinal and seasonal variability for comparison with the model results.
- The UARS data and concentrations of long-lived species derived from correlations were used to constrain photochemical, diurnal-steady state calculations for monthly-averaged conditions for the whole UARS period from 1992 to 1995. These calculations were first used to compare the calculated and measured [NO_x]/[NO_y], where the “measured” NO_y was obtained by either adding up the individual NO_y family members from UARS, or deriving it from correlations with N₂O and CH₄.
- Reasonable agreement is obtained between [NO_x]/[NO_y] calculated by models that include heterogeneous chemistry, and similar ratios derived from UARS measurements below 31 mbar, especially in the winter hemisphere. By this we mean that, although the box model calculations exhibit a slight low bias compared to ratios derived from UARS, they still fall within the monthly variability. In the summer (i.e. southern) hemisphere our model tends to under-predict the [NO_x]/[NO_y] at and above

46mb. The model systematically underestimates the $[\text{NO}_x]/[\text{NO}_y]$ above 30 mb in the both hemispheres. Reasons for this underestimation are not clear yet. However, it could be due to a deficiency in the gas-phase kinetics and/or photolytic data used (DeMore et al., 1997), since sulfate surface area density is small at these altitudes and heterogeneous chemistry plays a small role for the NO_y partitioning there.

- Our model results also reproduce the general features of the vertical profiles of NO , NO_2 and HNO_3 . However, we emphasize the model underestimation of the NO_2 content at the 30mb - 7mb levels, particularly evident in the summer hemisphere. This under-prediction translates into a 30-50% underprediction of the NO_2 column. Comparison of HNO_3 concentrations suggest a model overprediction of nitric acid in the same altitude range. Again, this suggests a deficiency in our understanding of the gas-phase chemistry regulating the partitioning of the NO_y family.
- The box model was used to calculate the photochemical removal rates of ozone due to each catalytic cycle (HO_x , NO_x , and halogen). Uncertainties in the HALOE data can translate into large uncertainties in the calculated removal rates near 100mb, but smaller at higher altitudes. These calculations suggest that the total ozone removal rate at middle latitudes increased right after the eruption of Mt. Pinatubo. The ozone loss rate by the halogen cycle can be factor of two larger in 1992 comparing with the normal aerosol conditions in 1995.
- The box model also performs well on the calculation of HO_x , NO_x and ClO_x radicals at noon by comparing with the MkIV balloon observational data. Allowing a HCl yield from the reaction of $\text{ClO} + \text{OH}$ does improve the agreement between model calculated ozone and observation above 46mb.
- It is expected that column ozone at high latitudes will increase between the year 2000 and 2050 as the chlorine content in the stratosphere decreases from 3.5 ppb to 2 ppb. UARS observations were used to provide realistic initial conditions for the air trajectory model to simulate the evolution of ozone in an air parcel in the Arctic winter. These calculations served to illustrate the potential impact of stratospheric cooling on ozone recovery. If the evolution of the ozone concentration in the air parcel is used as a proxy for ozone recovery, our calculations suggest that cooling

rates of -0.05 to -0.15K/year in the lower stratosphere could retard the recovery of ozone by as much as 15 to 20 years.

- A “trajectory hunting” technique was used to identify air parcels for which UARS, CLAES and MLS measurements could provide concentrations of key species both at the initial and final points. With the concentrations of key species fixed at the measured values at the initial point, the air trajectory model was used to calculate the concentrations for comparison with the final point, thus allowing testing of chemical and microphysical mechanisms. This technique was tested in Northern polar air parcels which exhibited chlorine activation. Model results were in better agreement with measurements if the temperatures from the UKMO analysis were reduced by 1-2K. Model calculations, and stoichiometric analysis suggest that the measured MLS ClO concentrations in version 4 may be too large at the 465K level. This discrepancy between model and observations may be resolved with MLS version 5.
- Wave analysis of the measured concentrations of N_2O and CH_4 from UARS was used to test approximations used in the eddy-diffusion formulation of transport by planetary wave breaking. This approximation would imply that the amplitudes of both tracers would have similar temporal behavior. Such behavior is observed at 56°N and 68°N , but not at 44°N . Work is ongoing to shed light on these discrepancies and their implication on 2-D model dynamical formulations.

Introduction and Overview

In this study, we make extensive use of the data from the Cryogenic Link Array Etalon Spectrometer (CLAES), Halogen Occultation Experiment (HALOE), and Microwave Link Sounder (MLS) instruments. Our purpose is to use the set of data both to provide input for our photochemical models as well as for comparison with model outputs. The suite of data from these three instruments provides most of the needed species concentrations. However, the three instruments do not sample the same air mass in their operations. To make maximum use of the data, it is necessary to derive methods to combine the data so that they can be consistently interpreted. The method we used depends on how the model is being used. In our analyses, the model is used in two modes:

- (1) simulating the mean state of the atmosphere to elucidate global-scale processes and provide a reference state for the assessment models;
- (2) process studies to simulate the behavior of specific measurements to help isolate particular mechanisms.

For the studies in mode (1), we put together a set of files from the HALOE and CLAES data, zonally averaged in latitudinal bins. This is discussed in section I. In section II, we describe how we invoke correlations between long-lived species to use the CLAES N₂O data to obtain zonal mean concentrations of total nitrogen (NO_y), total odd chlorine (Cl_y) and total odd bromine (Br_y). Section III describes our work in analyzing the impact of Pinatubo aerosols on partitioning of the nitrogen species in the lower stratosphere. The studies associated with the ozone budget in the stratosphere are presented in section IV. In section V, we make use of the temperature and Cl_y data in a study that examined the effect of future stratospheric cooling on partitioning of the chlorine species and the effects on Arctic ozone recovery.

For studies in mode (2), we reviewed the trajectory mapping technique that allow us to use data for an air mass obtained at one location to obtain information for the same air mass at locations that are not directly sampled by the instrument. This work is discussed in sections VI. Section VII reports on the results from our trajectory hunting

technique. This study made use of the CLAES and MLS data to examine the partitioning of the chlorine species in air masses traversing the high latitude lower stratosphere.

In addition, we also performed an analysis of the UARS 3B data to obtain the wave structure of N_2O and CH_4 . In Section VIII, we compare the observed structure to the wave structure predicted by our interactive three-wave model.

(I) Monthly zonal mean file of HALOE and CLAES data

We created a merged UARS data set containing the daily concentrations of trace species and temperatures measured by HALOE and CLAES, and zonally-averaged files on monthly- and yaw-averaged (i.e. during the 36-day yaw cycle) bases. HALOE and CLAES have different viewing geometries. HALOE provides 15 sunrise profiles at locations along one latitude circle, and 15 sunset profiles along a different latitude circle in the other hemisphere, corresponding to a total of 30 daily profiles. CLAES provides about 1200 profiles per day at different latitudes and local times from 34° latitude on one side of the equator to 80° on the other with 36-day yaw cycles, viewing the northern and southern high latitudes alternately. Daily CLAES version 7 measurements released on CD-ROMs, and version 18 of the HALOE data are used to create these merge files. The files contain measured concentrations of the following species: CH_4 , NO , NO_2 , H_2O , O_3 , HCl , and temperature from HALOE; N_2O , HNO_3 , ClONO_2 , and N_2O_5 from CLAES at the following 13 pressure levels: 100, 68.2, 46.4, 31.6, 21.5, 14.7, 10, 6.8, 4.6, 3.2, 2.2, 1.5, and 1 mbar. The daily files simply contain the available HALOE measurements, and the average of CLAES data within $\pm 5^\circ$ latitude and $\pm 10^\circ$ longitude distance from a HALOE point during a particular day at these levels.

There are 10 yaw-averaged files per year, since the duration of a yaw cycle is approximately 36 days. We bin the data by latitude with a 10° step from 70°S to 70°N and mark the UARS results by a mean latitude value in each bin (i.e. 65°S corresponds to the 70°S - 60°S band etc.). Available UARS data beyond the 70°S - 70°N range (namely, 80°S - 70°S and 70°N - 80°N) are ignored because they are rather sparse and cannot provide

enough coincident measurements by the CLAES and HALOE instruments in a 10° bin due to their sampling geometry. The HALOE measurements for each yaw cycle and latitude bin are averaged, thus forming a skeleton of the merge files for the sunrise and sunset data, separately. Only those CLAES daily measurements that are within 5° latitude distance from a HALOE sampling on the same day are selected for the yaw-averaged files. They are included in the merge files after simple zonal averaging. This approach should be robust for the long-lived species, like HNO_3 and N_2O . Possible errors in ClONO_2 data should be small (its diurnal variability could contribute only 3% at most in NO_y (Morris et al., 1997)). Each yaw-averaged merge file also contains variances of the measured parameters during a yaw cycle.

The same approach is used to create monthly zonally averaged merge files. Additionally, we created files of monthly zonally averaged CLAES measurements of N_2O , HNO_3 , and ClONO_2 , disregarding their proximity to the HALOE points. The use of the different files will be described in the following sections.

(II) Using species correlation to obtain NO_y

II.1. Introduction

As one measures the concentrations of trace gases in different air-parcels, one can obtain pairs of numbers corresponding to the concentrations of two species in each air-mass. If the number-pairs are displayed in a scatter diagram (using the concentration of one species for the x-axis, and the other for the y-axis), one often sees a compact curve if the local lifetime of the species are sufficient long. Plumb and Ko (1992) provided a framework to interpret these results. A compact curve can be expected when the local lifetimes of the two species are longer than the quasi-horizontal transport time in the lower stratosphere. In this case, the two species share the same mixing surface defined by the transport processes in the lower stratosphere, i.e. the mixing ratio of both species are constant on the same mixing surface. Plumb and Ko (1992) showed that the slope of the compact curve represents the ratio of the global fluxes of the trace species through the common mixing surface. In the region where the changes in fluxes of both species are

small from one mixing surface to another, the compact curve is a straight line. The existence of the compact curve (whether it is a straight line or not) in the scatter diagram allows one to predict the concentration of one species from the other. Correlation diagrams, such as linear correlations of some stratospheric tracers with N_2O , have been used as a diagnostic procedure to test chemical-transport models. The departures from the correlations also suggest effects from anomalous chemistry, such as denitrification (Fahey et al, 1990).

Correlations of N_2O vs. CH_4 and N_2O vs. NO_y are examined. These serve two purposes. First, we want to explore the possibility of deriving NO_y from UARS measurements for use in the AER box model to calculate NO_x/NO_y ratios (see section III). Secondly, we want to compare the conditions calculated by the AER 2-D model with the observational values from UARS. Data sources and analysis procedures will be discussed in Section II.2 and analysis results and discussion will be given in Section II.3.

II.2. Data Sources and Methodology

For our analysis, we used UARS level 3AT data to obtain daily HALOE (version 18) and CLAES (Version 7) data. Level 3AT data is organized by time along the orbit tracks. HALOE measures profiles for O_3 , HCl, HF, CH_4 , H_2O , NO, and NO_2 from about 15km to 60km. From CLAES measurement profiles of thirteen species (O_3 , H_2O , CH_4 , N_2O , NO, NO_2 , N_2O_5 , HNO_3 , ClONO_2 , HCl, CFC-11, CFC-12 and aerosols) are given between 10 and 60km with a vertical resolution of 2.5km. HALOE and CLAES have different viewing geometries. HALOE provides 15 sunrise and 15 sunset profiles. CLAES provides about 1,200 profiles per day at different latitudes and local time. In our analysis, we used HALOE CH_4 , NO and NO_2 , directly and interpolated CLAES data to get N_2O , HNO_3 , ClONO_2 and N_2O_5 values at the closest locations to HALOE measurements on same day. Since NO_x diurnal variation can be as large as a factor of 2 in the lower stratosphere, we only use the data from HALOE sunset measurements for this analysis. To get NO_y , we simply added up the concentrations of HALOE NO, NO_2 and CLAES HNO_3 , ClONO_2 and twice N_2O_5 . Figure II.1 shows a sample of the results of how the different components contribute to NO_y .

Since HALOE and CLAES instruments did not make simultaneous measurements, the diurnal variation of NO_x ($=\text{NO} + \text{NO}_2$), ClONO_2 and N_2O_5 measured at different local solar time would lead to an error for NO_y . HNO_3 is a diurnally stable species in the lower and middle stratosphere. HNO_3 and NO_x constitute more than 80% of total NO_y in the stratosphere (see Figure II.1). The contribution of NO_y from N_2O_5 and ClONO_2 would be under 20% (1-2-ppbv). Thus, the error from the diurnal variations of N_2O_5 and ClONO_2 is expected to be within the variability of NO_y (20 %).

We chose our approach after considering several options. We recognized that since HALOE and CLAES did not make simultaneous measurements of the same air-mass, ignoring the diurnal variation of the species by adding up concentrations from HALOE (NO and NO_2) and CLAES (ClONO_2 and N_2O_5) at different local times would lead to an error for NO_y . At the same time, taking measurements of CLAES at the same local time (i.e. same solar zenith angle) as the HALOE sunset measurement at different longitudes may introduce error if there is a wave-induced variations in the concentrations of HNO_3 . In the lower stratosphere, HNO_3 is the dominant species in the NO_y family. As shown in Figure II.1, the contribution from N_2O_5 and ClONO_2 is less than 20%. We also examined the average N_2O_5 and ClONO_2 concentrations for all the CLAES data for the whole day and convinced ourselves that the average values are very similar to the interpolated value shown. Thus, by following our approach, the error from diurnal variations of N_2O_5 and ClONO_2 is expected to be about 20%, within the variability of NO_y .

We did our analysis during the CLAES operating period from January 1992 to May 1993. The correlation of CH_4 (HALOE) vs. N_2O (CLAES) and N_2O vs. NO_y (HALOE and CLAES) were analyzed with the altitude range of 100mb to 1mb wherever data were available. The results are given in the next section, with comparisons to the ATMOS data and AER 2-D model output.

II.3. Results and Discussion

The correlations for UARS data are shown at 30°N-40°N, 10°N-10°S and 30°S-40°S latitudinal bins in January, April, July and October from January '92 to April'93, compared with the results from ATMOS and AER 2-D model. ATMOS data

was obtained from ATLAS (Mar.25-Apr.2, '92), ATLAS2 (Apr. 8-14, '93) and ATLAS3 (Nov. 3-12,'94) using trajectory models as a filter to distinguish air masses (Michelsen, et al., 1998). In the middle latitudes, ATMOS data were generally from middle and high latitudes of northern hemisphere.

The correlations of N_2O vs. CH_4 from all three ATMOS missions and the AER 2-D model are shown in Figure II.2. Model results indicate that the seasonal variations are very small. The data from UARS are given in Figure II.3 to II.6. ATMOS (red lines) and AER 2-D model outputs (blue lines) are also plotted in the same figures for comparison. The outputs of AER 2-D model are from $38^\circ N$, $38^\circ S$ and equatorial latitudinal bins individually. UARS data are indicated by plus signs. The green lines are polynomial fitting curves based on UARS data. The CH_4 - N_2O points are fitted as cubic curves for $[N_2O] < 50$ ppbv and a linear fitting is applied for $[N_2O] \geq 50$ ppbv. Generally, there is fairly good agreement between UARS, ATMOS data and AER 2-D models. However, both ATMOS and UARS data show a bias relative to the 2-D model results, with measured CH_4 being about 10-30% higher than modeled CH_4 for a given value of $[N_2O] < 200$ ppbv. UARS data points are more scattered than those from ATMOS and aircraft measurement, particularly for the month of October (Michelsen 1998; NASA Reference Publication 1292, Vol. III, 1993). This could be due to the larger samples in the UARS data, and/or the larger error bars of these data.

Figure II.7 shows the seasonal variations of correlations of N_2O vs. NO_y in the equator, and northern and southern middle latitudes for 1992-1994. There is good agreement between ATMOS and the 2-D model outputs for the NO_y - N_2O correlations for $[N_2O] > 100$ ppbv, at mid-latitudes, and a slight discrepancy at the equator. UARS data are plotted in Figure II.8 to II.11. The color coding of Figures II.8 – II.11 is the same as Figure II.3. The red, blue, and green lines are used to represent the data from ATMOS, AER 2-D model and UARS measurements respectively. Below 100ppbv of N_2O , the N_2O - NO_y points of UARS are fitted as cubic curve (green diamonds). Above 100 ppbv of N_2O , N_2O vs. NO_y points are fitted in a linear line (green line). The negative linear correlations of N_2O vs. NO_y (for $[N_2O] > 100$ ppbv) are in a better agreement between observations and models. When N_2O is less than 100 ppbv, the turning points of

N_2O - NO_y from positive to negative correlation (around 50 ppbv of N_2O) varies with latitudes from season to season. In the summer hemisphere, there are better agreements (30°S-40°S, January '92 and 30°N-40°N, July '92) between UARS, ATMOS and AER 2-D models than those in the winter hemisphere (30°N-40°N, January '92 and 30°S-40°S July '92). Since the planetary waves are more active in the winter hemisphere, the air mass of the middle latitude could be contaminated by polar air, which could cause such discrepancies. In the tropics, the discrepancies are getting larger, especially when N_2O is less than 100 ppbv. This could be associated with the interference of Mount Pinatubo sulfate aerosol layer (Roche et al 1996).

In summary, the above study suggest that there is reasonable agreement amongst the two data sets (UARS and ATMOS) and the 2-D model results for N_2O mixing ratios greater than 100 ppbv. It must be stressed, however, that the scatter in UARS data is in general much larger than for aircraft data and/or ATMOS, probably reflecting the larger error bars in the UARS data, and the lack of filtering of these data to eliminate tropical or polar intrusions. Thus, one would expect larger uncertainties in the use of correlations to derive trace species from UARS data. This fact is considered in the calculations described in the rest of the report.

(III) NO_y partitioning and Pinatubo aerosol

III.1 Introduction

Prior to the launch of the UARS in September 1991, nitrogen species in the stratosphere had been sampled by several different platforms: aircraft (e.g. recent aircraft campaigns are summarized in the following special issues: *J. Geophys. Res.*, 1989, nos. D9 and D14, 1992, no. D8, 1997, D3; *Science*, 261, 1128-1158, 1993; *Geophys. Res. Lett.*, 17, no.4, 1990; 23, no.23, 1994), balloons (e.g. Ridley et al., 1984, 1987; Kondo et al., 1996,1997; Jucks et al., 1996; Renard et al., 1996,1997; Osterman et al., 1997; Sen et al., 1998), ground-based (e.g. McKenzie et al., 1991; Johnston et al., 1992; Koike et al., 1993, 1994, 1998), limb infrared monitor of the stratosphere (LIMS) satellite (e.g. Gille et al., 1984; Russell et al., 1984), and the Atmospheric Laboratory for Applications and

Science (ATLAS) series of Shuttle missions (e.g. Kaye and Miller, 1996; Rinsland et al., 1994). The aircraft measurements revealed many interesting features of the nitrogen species behavior in the stratosphere, for example, saturation of the NO_x/NO_y ratio as a function of aerosol surface area above $\sim 5 \mu\text{m}^2/\text{cm}^3$ (Fahey et al., 1993) and denitrification in polar stratospheric cloud (PSC) regions (Fahey et al., 1990). However, such measurements are limited by the ER-2 ceiling altitude (~ 20 km), and their coverage is limited by aircraft paths and duration of flights. The balloon measurements mentioned can provide vertical profiles of several species up to 60 km (Osterman et al., 1997), but, again, these data have very limited coverage. Ground-based measurements of NO_2 and HNO_3 give the vertical profiles and column values of these species (McKenzie et al., 1991; Noltholt, 1994; Johnston et al., 1992; Koike et al., 1993, 1994). Such measurements provide data sets for long periods of time; however, they are limited to particular stations and their analysis could be affected by prevailing local meteorological conditions. The LIMS sampling has given a near-global picture of temperature, ozone, H_2O , NO_2 , and HNO_3 distributions during the October 1978-May 1979 period, which has been useful in validating global photochemical models (Jackman et al., 1987; Rood et al., 1993). The ATLAS series provide the most comprehensive set of atmospheric species sampled, but these data have limited temporal coverage (8-11 days) (Kaye and Miller, 1996).

Several special issues (see *Geophys. Res. Lett.*, 19, no.2, 1992, and 20, no.12, 1993; *J. Geophys. Res.*, no.D6, 1993, and no.D6, 1996; *J. Atmos. Sci.*, 52, 1995, no.17) have discussed different aspects of the UARS measurements. Recently, Dessler et al. (1998) summarized the principal scientific findings of the first five years from the UARS program. The UARS measurements provide a unique data set of key atmospheric species to be used for comparison of different satellite measurement techniques and validation of existing models of the atmosphere (Reber et al., 1993). The multi-year data sets of some UARS instruments (e.g. HALOE, MLS) provide not only pictures of the seasonal variability of some key stratospheric species on a near-global basis, but also an opportunity to investigate their inter-annual changes and trends.

The UARS launch about three months after the Mt. Pinatubo eruption provided a unique opportunity for atmospheric scientists to observe a near-global picture of the

response of the atmosphere to the strongest natural perturbation in this century. Figure III.1 shows sulfate aerosol surface area density (SAD) derived from the SAGE II extinction measurements in January 1992 and January 1993. As one can see, six months after the eruption the SAD is perturbed a factor of 20-30 larger than normal background values. The intrusion of volcanic gases and particles to the stratosphere can have a significant impact on stratospheric chemistry (Rodriguez et al, 1994; Koike et al, 1994; Salawitch et al, 1994). The SO₂ and H₂O injected into the stratosphere will be converted to sulfuric acid quickly and provide sites for heterogeneous reactions. Heterogeneous reactions would activate chlorine and convert reactive nitrogen species into the more stable nitric acid (see below). Meanwhile, the increased water vapor will lead to the enhanced OH and HO₂ which would further decrease NO_x and produce more HNO₃. Both these changes would change the ozone removal rate, especially in the middle latitudes.

Ground-based measurements detected an increase of HNO₃ and decrease of NO₂ columns after the arrival of the Mt. Pinatubo cloud (Johnston et al., 1992; Mills et al., 1993; Koike et al., 1993,1994; David et al., 1994; Preston et al., 1997; Slusser et al., 1996, 1998; Van Roozendaal et al., 1997), which could be explained by the considerably enhanced N₂O₅ and BrONO₂ hydrolysis on the Pinatubo aerosol:



Other heterogeneous reactions (R3-R5) on sulfate aerosol are important only at low (< 200 K) temperature:



Many modeling efforts have been undertaken to estimate different atmospheric effects of the Pinatubo aerosol (Boville et al., 1991; Brasseur and Granier, 1992; Pitari and Rizi, 1993; Bekki and Pyle, 1994; Kinnison et al., 1994; Rodriguez et al., 1994; Tie et al., 1994; Solomon et al., 1996; Rosenfield et al., 1997; Weisenstein et al., 1997). The HNO_3 and NO_2 responses to the Pinatubo eruption are consistent qualitatively with the model predictions. However, the magnitude of the observed perturbations of the HNO_3 and NO_2 columns at 45°S are almost two-fold larger than the calculated effect by the LLNL, AER, and GSFC 2-D models (Koike et al., 1994; Rosenfield et al., 1997).

The UARS data sets provide global coverage for the distributions of trace gases, and thus are very well suited for model-data intercomparison studies. We utilize UARS data to investigate whether the observed NO_x/NO_y , NO , NO_2 , and HNO_3 distributions under the wide range of aerosol loading in the post-Pinatubo stratosphere are consistent with those predicted by our model calculations. We worked closely on these issues with J.M. Mergenthaler, J.B. Kumer (CLAES team) and J.M. Russell III (HALOE team). In this chapter, we focus our study on analysis of the nitrogen species only, since they play an important role for the photochemical ozone balance in the stratosphere. Detailed analysis of the chlorine species partitioning has been done by Dessler et al. (1995,1996). Our related study in Section IV of this Report discusses the ozone photochemical tendencies in the stratosphere derived from UARS observations.

III.2. Methodology for Data Analysis

The HALOE and CLAES instruments provide 30 and approximately 1300 individual vertical profiles per day, respectively. To perform calculations for each profile for the period from January 1992 to September 1994 would be an enormous task. As an alternative, we created merge files of the CLAES and HALOE data to represent zonal monthly or yaw-averaged conditions (see Section I).

These files are used to provide input for the model runs. The measured species from these files are compared against the model results. To check the uncertainty introduced by such temporal averaging, we performed daily runs for February 1993. We picked this month because atmospheric circulation is perturbed at the end of the winter in

the northern hemisphere, thus providing potentially a worst-case scenario for our study. We calculate the monthly averaged $[NO_x]/[NO_y]$ ratios using our merge files as input.

The daily values of $\frac{[NO_x]}{[NO_y]}$ averaged over the month $\left\langle \frac{[NO_x]}{[NO_y]} \right\rangle$ is compared with a single calculation for the monthly averaged at the same level and latitude bin.

Figure III.2 depicts the relative difference of this comparison for

$$\frac{\left\langle \frac{[NO_x]}{[NO_y]} \right\rangle - \left\langle \frac{[NO_x]_{monthly}}{[NO_y]_{monthly}} \right\rangle}{\left\langle \frac{[NO_x]}{[NO_y]} \right\rangle} \text{ (in \%)}.$$

Data in the northern and southern hemispheres

correspond to HALOE sunset and sunrise measurements, respectively. In general, the difference between daily and monthly values is in the $\pm 10\%$ range almost everywhere, except for some points in the lower stratosphere. Further details of our analysis are given in Danilin et al. (1998c). Our conclusion from this test is that our approach using monthly- and yaw-averaged merge files is reasonable for the purpose of this study. A similar conclusion was obtained by Morris et al. (1997).

III.3. Model calculations

A diurnal steady-state version of the AER box model without PSC chemistry is used to calculate the concentrations of trace species. Previous analysis of aircraft data (Salawitch et al., 1994; Gao et al., 1997) shows that steady-state photochemical models can be applied almost everywhere in the stratosphere successfully, except in PSC processing regions or regions with temperature changes larger than 10-15 K/day (Kawa et al., 1993). A list of the included heterogeneous reactions on sulfate aerosol is given in Table III.1, with the updated $BrONO_2 + H_2O$ reaction probability given by $\gamma = 1 / (1/0.88 + 1/\exp(17.832 - 0.245wt\%))$ according to D.R. Hanson, (personal communication) (wt% is the weight percent of H_2SO_4 in sulfate aerosol). This change should be noted in the context of this study, since the new values of γ are larger than those in Hanson et al. (1996) by 0.3-0.4 and the $BrONO_2$ hydrolysis is not saturated even

at high volcanic aerosol loading, thus further reducing NO_x ($= \text{NO} + \text{NO}_2$) in the lower stratosphere (Danilin and McConnell, 1995; Lary et al., 1996). Other reaction rates are taken from DeMore et al. (1997).

Table III.1 Heterogeneous reactions on sulfate aerosol included in the model. The reaction probabilities are taken from DeMore et al. (1997), except the $\text{BrONO} + \text{H}_2\text{O}$ reaction (see text).

$\text{N}_2\text{O}_5 + \text{H}_2\text{O}$	\rightarrow	$\text{HNO}_3 + \text{HNO}_3$
$\text{BrONO}_2 + \text{H}_2\text{O}$	\rightarrow	$\text{HOBr} + \text{HNO}_3$
$\text{ClONO}_2 + \text{H}_2\text{O}$	\rightarrow	$\text{HOCl} + \text{HNO}_3$
$\text{ClONO}_2 + \text{HCl}$	\rightarrow	$\text{Cl}_2 + \text{HNO}_3$
$\text{HOCl} + \text{HCl}$	\rightarrow	$\text{Cl}_2 + \text{H}_2\text{O}$
$\text{HOBr} + \text{HCl}$	\rightarrow	$\text{BrCl} + \text{H}_2\text{O}$

The model is initialized with concentrations of long-lived species taken or derived from UARS data, and run over several diurnal cycles until the difference between the noon concentrations of all species are less than 2% for two consecutive days. Usually, it takes about 20 days at 100 mbar and a few days at 1 mbar to reach a steady-state.

Aerosol surface area data derived from SAGE-II measurements were kindly provided by G.K. Yue in zonal averaged format. The monthly mean values are shown in Figure III.1 for January 1992 and 1993, respectively. In January 1992 the aerosol cloud was so dense above the equator that the SAGE II retrieval algorithm could not provide reasonable data in this region (empty region at 21-24 km in Figure III.1).

Ozone, water and temperature were taken from the HALOE measurements. However, since UARS does not measure all necessary nitrogen, chlorine, and bromine

species to initialize the box model, some alternative methods are required. Table III.2 summarizes alternative methods to initialize NO_y , Cl_y , and Br_y .

Table III.2 Initialization methods for NO_y , Cl_y , and Br_y employed in this study, using the UARS data.

SPECIES		APPROACH	
	UARS	N_2O^{CLAES}	CH_4^{HALOE}
NO_y below 7 mbar	NO_y^{U}	$f_1(N_2O^{\text{C}})$	$f_4(\text{CH}_4)$
NO_y above 7 mbar	NO_y^{U}	NO_y^{U}	$f_4(\text{CH}_4)$
Cl_y	$f_2(N_2O^{\text{C}})$	$f_2(N_2O^{\text{C}})$	$f_2(N_2O^{\text{*}})$
Br_y	$f_3(N_2O^{\text{C}})$	$f_3(N_2O^{\text{C}})$	$f_3(N_2O^{\text{*}})$

Where f_1 is given by Keim et al. 1997 and Loewenstein et al. 1993; f_2 is given in Woodbridge et al., 1995; f_3 is given by Salawitch 1998; and f_4 is given by Michelsen et al. 1998.

III.3.a. NO_y initialization.

The first method is to approximate NO_y ($=\text{NO} + \text{NO}_2 + \text{NO}_3 + \text{HNO}_3 + \text{HONO} + \text{HNO}_4 + 2\text{N}_2\text{O}_5 + \text{ClONO}_2 + \text{BrONO}_2$) as $\text{NO}_y^{\text{U}} = \langle \text{NO}^{\text{H}} \rangle + \langle \text{NO}_2^{\text{H}} \rangle + \langle \text{HNO}_3^{\text{C}} \rangle + \langle \text{ClONO}_2^{\text{C}} \rangle$, where $\langle \text{NO}^{\text{H}} \rangle$ and $\langle \text{NO}_2^{\text{H}} \rangle$ are the monthly (yaw)-averaged NO and NO_2 measured by HALOE and $\langle \text{HNO}_3^{\text{C}} \rangle$ and $\langle \text{ClONO}_2^{\text{C}} \rangle$ are the CLAES-measured monthly (yaw)-averaged HNO_3 and ClONO_2 . The symbol $\langle \rangle$ denotes zonally averaged value of the bracketed species during a yaw cycle. We did not include CLAES N_2O_5 in the equation for NO_y since these measurements are recommended for use only at 3.2, 2.2, and 1.5 mbar (Kumer et al., 1996). We thus underestimate NO_y by up to 1 ppbv below these levels. Other omitted species in the equation for NO_y^{U} (NO_3 , HONO , HNO_4 , BrONO_2) may contribute only a few percent or less to NO_y , and thus are unimportant for the purposes of this study.

The second approach is to use zonally averaged values of CLAES $\langle \text{N}_2\text{O}^{\text{C}} \rangle$ to derive NO_y using equation (1) (Loewenstein et al., 1993):

$$[\text{NO}_y] = 20.7 - 0.0644 * [\text{N}_2\text{O}], \quad (1)$$

in the Northern hemisphere, and equation (2) (Keim et al., 1997)

$$[\text{NO}_y] = 21.82 - 0.0699 * [\text{N}_2\text{O}], \quad (2)$$

in the Southern hemisphere. In the above equations $[\text{NO}_y]$ and $[\text{N}_2\text{O}]$ are in ppbv. These empirical N_2O - NO_y correlations are valid for $[\text{N}_2\text{O}] > 50$ ppbv (below ~ 10 mbar) (Fahey et al., 1990; Prather and Remsberg, 1993). Above this altitude, destruction of NO_y via photolysis of NO followed by the $\text{N} + \text{NO} \rightarrow \text{N}_2 + \text{O}$ reaction cause the correlation curve to turn over. Above 7mb, we use NO_y^U or utilize the correlations derived from ATMOS (see Chapter II). These two approaches can be used to initialize our box model only until May 1993, since the CLAES cryogen supply was exhausted after that time.

The third method, which uses the HALOE measurements of CH_4 , allow us to extend our model analysis after May 1993. This approach uses the empirical correlation between NO_y , N_2O , and CH_4 based on the analysis of ATLAS/ATMOS data (Michelsen et al., 1998). Their analysis provides two sets of the equations:

tropics (20°S - 20°N) 0.4 ppmv < $[\text{CH}_4]$ < 1.28 ppmv	$[\text{NO}_y] = -1.3519 \cdot 10^{-8} + 0.05794 \cdot [\text{CH}_4] - 18544 \cdot [\text{CH}_4]^2 - 7.3339 \cdot 10^9 \cdot [\text{CH}_4]^3$
tropics (20°S - 20°N) $[\text{CH}_4] \geq 1.28$ ppmv	$[\text{NO}_y] = -7.9107 \cdot 10^{-7} + 1.4051 \cdot [\text{CH}_4] + 8.3839 \cdot 10^5 \cdot [\text{CH}_4]^2 - 1.6787 \cdot 10^{11} \cdot [\text{CH}_4]^3$
outside tropics $[\text{CH}_4] \leq 0.9$ ppmv	$[\text{NO}_y] = -1.2321 \cdot 10^{-9} + 0.02276 \cdot [\text{CH}_4] - 31866 \cdot [\text{CH}_4]^2 - 4.178 \cdot 10^{10} \cdot [\text{CH}_4]^3$;
outside tropics $[\text{CH}_4] > 0.9$ ppmv	$[\text{NO}_y] = 9.8251 \cdot 10^{-9} + 0.0418 \cdot [\text{CH}_4] - 55088 \cdot [\text{CH}_4]^2 + 1.608 \cdot 10^{10} \cdot [\text{CH}_4]^3$,

here $[\text{NO}_y]$ and $[\text{CH}_4]$ are in mixing ratio. As discussed above, we must stress the approximate nature of these correlations when applied to UARS data. Also, they do not

account for possible latitudinal and seasonal changes, which could be particularly important at higher altitudes (Keim et al., 1997).

Figure III.3 compares the NO_y fields in January 1993 calculated from the three methods outlined above. This month is chosen because it contains the largest latitudinal coverage by the sunset UARS measurements. Also, this month could be considered typical—since our analysis of similar plots for other months and years shows that principal similarities and differences between these NO_y initialization are persistent. Detailed analysis of the differences between these three methods of NO_y initialization is given in Danilin et al. (1998c). Briefly, the first way of the NO_y initialization is preferable, however, it is limited to May 1993 because of the CLAES instrument lifetime.

III.3b. Cl_y and Br_y initializations.

Initial inorganic chlorine Cl_y ($=\text{HCl} + \text{ClONO}_2 + \text{HOCl} + \text{Cl} + \text{ClO} + \text{BrCl} + 2(\text{Cl}_2 + \text{Cl}_2\text{O}_2)$) is approximated from the correlation of total organic chlorine with N_2O (Woodbridge et al., 1995; their equation (11)) and the dependence of the Cl_y fraction of total chlorine as a function of N_2O (their Figure 7). The initial values of inorganic bromine Br_y ($=\text{Br} + \text{BrO} + \text{HOBr} + \text{BrONO}_2 + \text{BrCl} + \text{HBr} + 2\text{Br}_2$) are inferred from the empirical correlation of Br_y with N_2O (R.J. Salawitch, personal communication, 1997):

120 ppbv < $[\text{N}_2\text{O}]$ < 312 ppbv	$[\text{Br}_y] = 13.009 + 0.1284 * [\text{N}_2\text{O}] - 5.452 * 10^{-4} * [\text{N}_2\text{O}]^2$
$[\text{N}_2\text{O}] = \leq 120$ ppbv	$[\text{Br}_y] = 21.0984 - 0.5317 * [\text{N}_2\text{O}] / 120,$

where $[\text{Br}_y]$ is in pptv and $[\text{N}_2\text{O}]$ is in ppbv ($\text{Br}_y=1$ pptv is assumed at $\text{N}_2\text{O} > 312$ ppbv). These values of Br_y could differ by up to 2 pptv from the recent analysis by Wamsley et al. (1998) in the stratosphere. However, this potential difference is not important for the analysis of nitrogen species presented here.

To calculate the Cl_y and Br_y contents, the N_2O values could be obtained from the yaw-averaged CLAES $\langle \text{N}_2\text{O} \rangle$ data before May 1993 or HALOE data of $\langle \text{CH}_4 \rangle$ after May 1993 using the CH_4 - N_2O correlation (Michelsen et al., 1998):

tropics (i.e. 20°S-20°N)	$[N_2O]^* = -1.2851 \cdot 10^{-7} + 0.7742 \cdot [CH_4] - 1.5510 \cdot 10^6 \cdot [CH_4]^2 + 1.3097 \cdot 10^{12} \cdot [CH_4]^3 - 3.3888 \cdot 10^{17} \cdot [CH_4]^4;$
outside the tropics	$[N_2O]^* = -2.2309 \cdot 10^{-8} + 0.1934 \cdot [CH_4] - 5.6278 \cdot 10^5 \cdot [CH_4]^2 + 7.3019 \cdot 10^{11} \cdot [CH_4]^3 - 2.34 \cdot 10^{17} \cdot [CH_4]^4,$

here $[N_2O]^*$ and $[CH_4]$ are in mixing ratio. These are differences thus in $[N_2O^C]$ and $[N_2O^*]$ when both CLAES N_2O and HALOE CH_4 are available. Thus, the contents of inorganic chlorine and bromine species could be different for the two approaches. However, the possible differences do not significantly affect nitrogen species partitioning investigated in our study.

III.4. NO_x/NO_y

We performed model runs for each yaw period from January 1992 to September 1994 for sunrise and sunset measurements, except for June 1992, when HALOE did not operate because of technical problems aboard the UARS. Latitudinal coverage of our merge files and, consequently, our model calculations differ from month to month, depending on the geometry of the HALOE and CLAES samplings. In this study we focus on analysis of the nitrogen species behavior primarily at 45°S and 45°N, since additional ground-based measurements of NO_2 and HNO_3 are available at these latitudes.

Figure III.4 shows temporal evolution of the sunset $[NO_x]/[NO_y]$ ratio and aerosol SAD at four levels: 68, 46, 31, and 22 mbar levels at 45°S (left column) and 45°N (right column). We show these levels because the lower stratosphere has the strongest perturbation due to Pinatubo aerosol (e.g. Yue et al., 1994; Lambert et al., 1997; Thomason et al., 1997). Results at the lowermost level of 100 mbar are not shown because the UARS measurements are very noisy due to retrieval problems within a dense Pinatubo aerosol cloud. Since the model $[NO_x]/[NO_y]$ ratio is insensitive to the NO_y values used in the calculation, our model results are shown only by red crosses in Figure III.4 for the CH_4 approach only. However, there are differences among UARS $[NO_x]/[NO_y]$ results because of the different ways to define $[NO_y]$ according to the UARS (yellow symbols), N_2O (blue symbols), or CH_4 (green symbols) approaches. The

monthly error bars shown represent the standard deviation of the $[\text{NO}_x]/[\text{NO}_y]$ over one month.

Comparison of the model and UARS results show a good agreement at the 68mb and 46 mbar levels throughout the whole period analyzed, although the box model calculations tend to have a low bias relative to the ratios derived from UARS. However, at the upper levels (particularly, at 22 mbar), a clear underestimation of the NO_x/NO_y ratio by the box model in summer in both hemispheres is evident. At some points (January 1993 at 45°S and July 1992 at 45°N, 22 mbar) this disagreement can be more than 30%. Similar problems were mentioned by Morris et al (1997), Sen et al. (1998), and Kondo et al. (1998).

To investigate the dependence on altitude and latitude of the $[\text{NO}_x]/[\text{NO}_y]$ ratio, we present results in Figure III.5 for January 1993 between 68 and 4.6mb. The UARS $[\text{NO}_x]/[\text{NO}_y]$ ratio is shown by the yellow, blue and green symbols for the UARS, N_2O , and CH_4 approaches, respectively (see Table III.1). The model values of $[\text{NO}_x]/[\text{NO}_y]$, calculated for the CH_4 approach, are shown by red and black lines for calculations with and without heterogeneous reactions on sulfate aerosol, respectively. We performed model runs with gas phase chemistry only to investigate a sensitivity of the model $[\text{NO}_x]/[\text{NO}_y]$ ratio to the heterogeneous reactions on sulfate aerosol. Recently, Donahue et al. (1997) argue that current recommendations (DeMore et al., 1997) overestimate the HNO_3 formation reaction rates by 10-30% at room temperature over a whole range of pressures. We thus ran our model with heterogeneous reactions on sulfate aerosol and with the reduced by 25% reaction rate of $\text{OH} + \text{NO}_2 + \text{M} \rightarrow \text{HNO}_3 + \text{M}$ (shown by the grey lines) to reflect the possibility outlined by Donahue et al. (1997), assuming that their data are valid for the stratospheric conditions.

Summarizing results in Figures III.4 and III.5, one can say that: (1) the agreement between $[\text{NO}_x]/[\text{NO}_y]$ calculated by models which include heterogeneous chemistry, and similar ratios derived from UARS measurements is reasonable below 31 mbar, especially in the winter (i.e. northern) hemisphere. By this we mean that, although the box model calculations exhibit a slight low bias compared to ratios derived from UARS, they still fall within the monthly variability. In the summer (i.e. southern) hemisphere our model tends to under-predict the $[\text{NO}_x]/[\text{NO}_y]$ at and above 46mb; (2) the model systematically

underestimates the $[\text{NO}_x]/[\text{NO}_y]$ above 30mb in the both hemispheres. Reasons for this underestimation are not clear yet, but likely they deal with gas-phase kinetics or photolytic data used (DeMore et al., 1997), since SAD is small at these altitudes and heterogeneous chemistry plays a small role for the NO_y partitioning there.

III.5. Vertical profiles of NO , NO_2 , and HNO_3 .

To investigate model underestimation of the $[\text{NO}_x]/[\text{NO}_y]$ ratio in the stratosphere more carefully, we analyze separately the sunset vertical profiles of NO , NO_2 , and HNO_3 in January 1993 at 45°S (summer) and 35°N (winter) according to the UARS initialization (see Figure III.6). The features shown in this figure are typical for other months and years. The UARS values are shown by symbols, the box model profiles for the UARS approach by solid and dashed lines for calculations with and without heterogeneous reactions on sulfate aerosol, respectively. Below 30 mbar (~ 24 km) and above 6 mbar (~ 34 km), the model reproduces the observed profiles of these nitrogen species reasonably well. Model properly reproduces the ClONO_2 vertical profile (not shown in this figure). Consistent with the results in Figure III.4 and III.5, the model could not explain the NO_x measurements in the 24-34 km range, mostly due to underestimate of NO_2 . We note that this is also accompanied by a model overestimate of HNO_3 , again suggesting a need for revision in the gas-phase kinetics of HNO_3 formation and destruction. The model under-prediction of the NO_2 distribution is translated to 30-50% under-prediction of the NO_2 column (especially noticeable during summer) (Danilin et al., 1998c).

III.6. Conclusions

We have presented analyses of the UARS measurements (HALOE and CLAES) using the AER diurnal steady-state box model from January 1992 to September 1994. It was shown that use of zonal yaw-averaged UARS measurements, which avoid high uncertainties of the UARS individual profiles and considerably reduce computer time for analysis, captures the principal features of the nitrogen species partitioning in the global post-Pinatubo stratosphere.

The AER diurnal steady-state photochemical box model, with proper constraints from the UARS measurements, was used for analysis of this data set. In general, our results show that the model results including heterogeneous chemistry are in good agreement with the UARS data below 30 mbar, thus supporting our current parameterization of the heterogeneous reactions on sulfate aerosol. Our box model results suggest a seasonally-modulated gradual increase of the $[\text{NO}_x]/[\text{NO}_y]$ ratio after the Pinatubo eruption in the lower and middle stratosphere at 45°N and 45°S. Due to the scatter in the UARS data, such an increase cannot be determined in the measurements.

Among clear discrepancies between model results and UARS measurements, we emphasize the model underestimation of the NO_2 content at the 30mb - 7mb levels, particularly evident in the summer hemisphere. This under-prediction translates into a 30-50% underprediction of the NO_2 column. Comparison of HNO_3 concentrations suggest a model overprediction of nitric acid in the same altitude range.

(IV) Utilization of HALOE data to calculate zonal-mean of ozone production and loss rates in the lower and middle stratosphere

IV.1. Introduction

The global coverage of measurements of trace species from UARS provides us with a good opportunity to further test the chemistry of ozone removal in the lower and middle stratosphere by HO_x , NO_x and ClO_x radicals. The UARS satellite was launched in September 1991, shortly after the eruption of Mt. Pinatubo in June of that year. The large amount of volcanic aerosols ejected into the atmosphere allows us to test impact of accelerated heterogeneous conversion of NO_x to HNO_3 in the enhanced stratospheric aerosol layer, and the relative contribution of the HO_x , ClO_x , and NO_x catalytic cycles to chemical ozone removal.

Up until the early 90's it was believed that nitrogen cycle dominated chemical ozone removal in the lower stratosphere. But recent studies from in-situ observations, as well as modeling work including the heterogeneous chemistry on sulfate aerosols, have challenged the idea (Wennberg et al., 1994; Salawitch, et al., 1994). The *in situ*

measurements of OH, HO₂, NO, NO₂, ClO and BrO radicals were made at the mid-latitude lower stratosphere by NASA ER-2 aircraft in the Stratospheric Photo-chemistry, Aerosols and Dynamics Expedition (SPADE) campaign in 1993. The data from these measurements show that the hydrogen and halogen radicals dominated destruction of O₃ in the mid-latitude lower stratosphere in winter/spring, while the nitrogen radicals contributed less than 20% to the total O₃ loss. In the middle and high stratosphere (above 40km), the "ozone deficit" problem still exists. Even though at that altitude ozone is expected to be in photochemical equilibrium, but the modeled photochemical ozone loss exceeds the production by 10-50%(Crutzen et al, 1995; Jucks et al, 1996; Osterman, et al, 1997).

In this portion of the report, we focus on the problem of ozone budget in the lower and middle stratosphere (up to 40km). We utilized UARS HALOE data to constrain a photochemical box model with heterogeneous chemistry. HALOE data and box model will be described in detail in Section IV.2. Since there are no simultaneous measurements of concentration of HO_x, NO_x and Cl_x radicals in the HALOE data, the results of the box model are compared to the *in-situ* measurements from balloons in Section IV.3. The relative contributions of different catalytic cycles to ozone removal are discussed in Section IV.4.

IV.2. Methods

IV.2a. Use of HALOE data to initialize the box model

The photochemical box model is initialized by monthly zonally averaged HALOE (version 18) temperature, O₃, H₂O, CH₄ and HCl from January 1992 to December 1995. The HALOE data is binned every 10 degrees (65°S-65°N). Linear correlation of CH₄-N₂O is used to derive N₂O profile, which is applied to calculate NO_y, Cl_y, Br_y respectively through their correlations with N₂O (Michelsen 1998; Woodbridge et al. 1995; and Salawitch personal communication 1997). The CH₄-N₂O and N₂O-NO_y correlations are derived from ATMOS data, which are generated from ATMOS AT-2 (April 8 to 14, 1993), AT-3 missions (November 3 to 12, 1994), grouped separately in the tropics and northern middle latitude by Michelsen (1998). For details about how the data were

binned, and NO_y , Cl_y and Br_y were calculated through N_2O , please see the discussion in Section II and III, and the manuscript by Danilin et al. (1998c; Appendix).

In the lower-most stratosphere (100 hPa), the measurements from UARS have large error bars. Meanwhile, NO_y calculated from CH_4 - N_2O - NO_y correlations also look problematic at 100 hPa, probably due to the large error bars and uncertainties in the measurements. In the middle stratosphere where $[\text{N}_2\text{O}]$ is less than 100ppbv, the correlation between N_2O and NO_y becomes nonlinear. The fitting of N_2O - NO_y correlations from ATMOS may have larger uncertainties at latitudes and seasons not measured by ATMOS when $[\text{N}_2\text{O}]$ is below 100 ppbv, which correspond approximately to pressures of above 10 hPa.

The standard pressure levels at UARS are applied in the calculation (100, 68, 46, 32, 21, 14, 10, 6.8, 4.6, 3.2, 2.1, 1.4 and 1.0 hPa). The profiles from 68 hPa to 1 hPa from the box model are used for most of analysis. The photochemical model runs to diurnal steady state to calculate the integral of ozone production and loss of each radical species over a daily 24 hour cycle. Reaction rates and absorption cross sections are from DeMore et al. (1997). A reaction probability of 0.1 is used for the hydrolysis of N_2O_5 . The aerosol surface area is obtained from SAGE II monthly zonal mean data (Yue et al. 1994). All the run included 7% channel from $\text{ClO}+\text{OH}$ to form HCl (Osterman et al, 1997; Michelsen, et.al. 1996)

IV.2b. Definitions of Catalytic Cycles

The total ozone loss is a sum of odd oxygen loss due to hydrogen, nitrogen, halogen and oxygen cycles, respectively. In our study, we define each catalytic cycle shown in Table 1.

Table IV.1: Definitions of catalytic cycles in the box model

Loss: $L_{\Sigma} = L_{O_1} + L_{HO_x} + L_{NO_x} + L_{halogen}, L_{halogen} = L_{ClO_x} + L_{BrO_x}$
$L_{O_1} = 2k_{35}(O)(O_3)$
$L_{HO_x} = k_7(OH)(O_3) + k_9(HO_2)(O_3) + k_{10}(HO_2)(O) + k_{19}(OH)(O) + k_6(H)(O_3)$
$L_{NO_x} = 2(k_{39}(NO_2)(O) + J_{NO_3 \rightarrow NO}(NO_3)) + k_{74}(HNO_4)(O) + k_{N_2O_5+H_2O}(N_2O_5) + \text{some minor terms}$
$L_{ClO_x} = 2(k_{31}(ClO)(O) + J_{Cl_2O_2}(Cl_2O_2)) + J_{HOCl}(HOCl) + k_{50}(HOCl)(O) + k_{33}(HCl)(O) + k_{67}(ClO)(OH)$
$L_{BrO_x} = 2k_{54}(BrO)(O) + (k_{BrO+ClO \rightarrow Br+Cl} + k_{BrO+ClO \rightarrow BrCl})(BrO)(ClO) + (k_{55} + k_{94})(BrO)(BrO) + J_{HOBr}(HOBr) + k_{96}(BrO)(OH)$

The rate of each catalytic cycle is defined as the rate of the slowest reaction in this cycle. We stress that, in defining the above cycles, certain algebraic approximations are adopted which may not be exactly the same as other methods, although the TOTAL chemical removal of ozone must agree.

IV.3. Calculated Radicals from Box Model: Comparison to Balloon data

HALOE measures the radicals NO and NO₂ at sunrise and sunset. Sections II and III presented results of tests of the chemistry against the UARS observations. To further verify the chemical mechanism and numerics in the box model, the input data (CH₄, H₂O, O₃, N₂O, NO_y, Cl_y) from the MkIV of balloon flight (34.5°N, 104.2°W) on September 25, 1993 in Osterman et al.'s paper (1997) were used to constrain the box model. The MkIV experiment also provided simultaneous measurement of concentrations of HO_x, NO_x. The calculated radicals from the box model are compared with the radicals (OH, HO₂, ClO and NO₂) in the Osterman's paper, which are scaled from observational radical precursors (Osterman et al. 1997). We are most interested in the altitude region relevant to our UARS analysis, i.e., , the profiles from 68 hPa to 1 hPa.

The comparisons of the radicals at noon time from the box model and Osterman et al. box model are illustrated in Figure IV.1. The output from the AER box model is plotted as dashed lines. The solid line is from Osterman's paper. The percentage

differences between AER's and Osterman's results are under 10%. The box model adopts a 7% yield of HCl from ClO + OH channel (Michelsen et al. 1996; Osterman et al. 1997). The output of ClO profile from the box model without HCl from ClO + OH channel is plotted as a dotted line. Obviously, ClO is overestimated without the loss through ClO + OH channel. The good agreements of radical profiles between the box model and the MkIV data further strengthens our assumption that the chemistry in our box model is sufficient to simulate the real stratosphere.

IV.4 Ozone Loss from Different Catalytic Processes at Middle Latitudes During 1992-1995

Ozone loss frequency is defined as the total ozone loss divided by the local ozone correlation. Ozone loss frequencies at middle latitude in the summer hemisphere (45°S, January) during 1993-1995 are compared with values in 1992 to see if there are any changes corresponding to the decrease of Pinatubo's aerosol surface areas. In Figure IV.2, the loss frequency decreased each year after 1992 at altitudes below 46mb. At 68mb, the total ozone loss in 1995 is only 70% of total ozone loss in 1992. At altitude above 32mb, the loss frequencies have little changes from 1992 to 1995.

To understand how the different catalytic cycles contribute to total ozone loss, the ozone loss frequencies from HO_x, NO_x, Cl_x and Br_x, and O_x cycles at 45°S for January are plotted individually in Figure IV.3a, in which 1993, 1994 and 1995 data are compared with the values in 1992. The ozone losses from the HO_x, Cl_x and Br_x cycles were larger in 1992 when NO_x loading was minimum in the middle latitude region due to more HNO₃ formed from the hydrolysis of N₂O₅ on sulfuric acid aerosols (Danilin et al 1998c). The ozone removal rate from NO_x cycle has increased at 32mb and 46mb since 1993. At 68mb, the ozone removal rate from HO_x cycle in 1995 is only 70% of the 1992 value while the Cl_x and Br_x cycles in 1995 are less than 50% of the 1992 values.

The relative contributions to the ozone removal rate from each cycle between 1992 and 1995 are illustrated in Figure IV.3b. The percentage contributions due to HO_x, NO_x have small changes with magnitudes of 10-15% at lower stratosphere (68mb). But the relative contributions to ozone sink from Cl_x and Br_x are different by a factor of two

between 1992 and 1995. The contribution from O_x is under 10% and no changes from 1992 and 1995.

Results for July at 45°S are shown in Figure IV.4a, IV.4b. The relative contributions to the ozone removal due to Cl_x and Br_x cycles are larger (30-45% in the lower stratosphere), while the contributions from NO_x cycle are reduced (10-15%).

IV.5 Sensitivity of model-calculated ozone loss to uncertainties in HALOE data

In addition to the limitations of the box model itself, the results of the model are affected by the uncertainties of the satellite measurements, the correlations used to calculate NO_y , Cl_y and Br_y , and even the zonal mean methods to bin the data. In order to understand how the uncertainties would effect the calculations of total ozone budget in the box model, a sensitivity study was performed by varying the CH_4 profile within the 1σ variations. This uncertainty is then propagated to uncertainties in NO_y , Cl_y and Br_y .

The profile at 45°S in January 1995 is chosen by letting CH_4 varies between the $1-\sigma$ limit. The results are shown in Figure IV.5a, IV.5b. The solid lines represent the profile of CH_4 has 1σ less than its values, while the dashed lines have 1σ more.

The variances of NO_y , Cl_y and Br_y are shown in Figure IV.5a. The 8-10% variation in CH_4 can have a very large (40% - 150%) effect on NO_y , Cl_y , Br_y at 100mb. The behavior of NO_y value at 1.4mb is probably due to the correlation function. But for most of altitude, the effects on NO_y , Cl_y and Br_y are less than 20%. Above 10mb (about 30km), the variances of CH_4 have little effects on Cl_y and Br_y values.

The variations in the calculated ozone removal rates by each catalytic cycle are plotted on Figure IV.5b. Except at 100mb, the effects on halogen and hydrogen cycles are under 5%. But the ozone loss by nitrogen cycle can vary by 20%.

IV.6 Summary

The box model calculation suggests that the total ozone removal rate at middle latitudes does increase right after the eruption of Mt. Pinatubo. With the decrease of NO_x in the lower and middle stratosphere due to more HNO_3 formation from N_2O_5 on sulfuric acid aerosols, ozone removal rates from hydrogen and halogen cycles increase. The

ozone loss rate by the halogen cycle can be factor of two larger in 1992 comparing with the normal aerosol conditions in 1995.

The box model is not constrained by measured radicals. It seems the model does well on the calculation of HO_x , NO_x and ClO_x radicals at noon by comparing with the model of Osterman et al. (1997). This implies good agreement for HO_x and ClO_x radical, but again the underestimate in NO_x described in Sen et al. (1997). Allowing HCl from $\text{ClO} + \text{OH}$ channel does improve the model fitting better with observation.

There are some limitations in our study using the box model. First, the assumption on steady state may not be valid in the high latitude winter, where PSC chemistry plays a big role. Secondly, there is the uncertainty of reaction rate constants determined in laboratory investigations (Wennberg, et al., 1994; Jucks et al. 1996; Osterman et al. 1997). Thirdly, the errors due to UARS measurements and uncertainties of the correlation-ships could bring bias in the model's calculations.

(V) Utilization of UARS data to analyze effects of stratospheric cooling on Arctic ozone recovery.

Analysis of stratospheric temperature data sets and model calculations clearly show statistically significant stratospheric cooling, particularly noticeable in the polar lower stratosphere (up to 2 K/decade). (e.g., IPCC, 1995; WMO, 1995). Since rates of heterogeneous reactions on polar stratospheric clouds (PSCs) grow exponentially as temperature drops, it is important to understand how the observed stratospheric cooling affects anticipated ozone recovery due to curbing CFCs production according to the Montreal Protocol. The existing UARS data is too short to provide a statistically meaningful analysis of the temperature or ozone trends in the stratosphere. However, the UARS data contains valuable information about spatial-temporal distribution of several important stratospheric species (O_3 , NO , NO_2 , HNO_3 , ClO , HCl , ClONO_2 , CH_4 , N_2O , H_2O etc.), which provide realistic constraints on model calculations.

We simulated the behavior of an isolated air parcel at 70°N subsiding with a rate of 1 km/month from 24 km on December 1 to 20 km on April 1 (Rosenfield et al., 1994). To investigate the sensitivity of ozone depletion to a wide range of chlorine loadings and

stratospheric coolings, we performed model calculations for 2 to 3.5 ppbv Cl_y and 0 to 5 K stratospheric cooling. This study (Danilin et al., 1998a) used HALOE measurements of ozone, methane, water vapor and HCl together with CLAES measurements of ClONO_2 , HNO_3 , and N_2O and MLS measurements of ClO to constrain our model calculations of the "present day" conditions in the Arctic lower stratosphere. The adopted initial values of NO_y (14 ppbv), Cl_y (3 ppbv), and Br_y (20 pptv) at 24 km altitude at 70°N are consistent with the CLAES N_2O measurements and the NO_y - N_2O (Loewenstein et al., 1993), Cl_y - N_2O (Woodbridge et al., 1995), and Br_y - N_2O (Wamsley et al., 1998) correlations. Also, the extent of denitrification in the Arctic polar vortex in the present day atmosphere is set to be consistent with the MLS HNO_3 . Temperature history, along idealized air parcel is shown in Figure V.1 and chosen to be consistent with the typical conditions at 70°N and 31 mbar according to the UARS measurements (Santee et al., 1996).

For the purposes of our idealized study, the effects of stratospheric cooling are investigated by lowering the whole temperature history uniformly by 1 to 5 K while keeping its shape unchanged as shown in Figure V.1. The change of O_3 mixing ratio in the air parcel on April 1 as a percentage of its initial value of 3.6 ppmv is plotted as a function of chlorine loading and stratospheric cooling in Figure V.2 for the NAT and STS PSC schemes. This figure underlines the widely accepted point that ozone content decreases with increasing levels of Cl_y (follow any horizontal line in Figure V.2). However, this figure also clearly shows that possible further stratospheric cooling (due to decrease of O_3 or increase of CO_2 and H_2O (IPCC, 1995; WMO, 1995)) has an effect equivalent to an increase of chlorine loading from the ozone balance point of view.

In order to further elucidate results in Figure V.2, we introduce chlorine-cooling equivalent (CCE) as a measure of the change in chlorine loading equivalent to a 1 K cooling for a given level of ozone depletion in the air parcel under specified ambient conditions (Danilin et al., 1998a). For the parcels considered, the values of CCE are equal to 0.7 and 0.4 ppbv (Cl_y)/K for the NAT and STS schemes, respectively. The CCE concept could be useful for further analysis of ozone recovery in the polar atmosphere under projected temperature and chlorine loading trends.

As a continuation of our sensitivity analysis, we present calculations of ozone behavior, along the idealized air parcel considered in the previous sections using anticipated future levels of chlorine loading and assumed stratospheric cooling. We follow the WMO scenarios for the Cly (shown by black line in Figure V.3) and CH₄ concentrations assuming $B_{ry}=20$ pptv. Figure V.3 shows that, ignoring stratospheric cooling, one indeed should anticipate a steady recovery of ozone (green line) in the lower stratosphere immediately after reduction of the Cly loading peaking at the level of 3.08 ppbv at 24 km (or ~3.7 ppbv at the top of the stratosphere) near the year 2000. Data analysis and model calculations (Randel and Cobb, 1994; Ramaswamy et al., 1996) show that temperature trends could be as much as -0.2 K/yr in the Arctic lower stratosphere in winter/spring. Even for the relatively modest constant temperature trend of -0.05 K/yr, ozone remains below its 1995-level for the next 40 years in the NAT scenario. For the temperature trend of -0.15 K/yr, a larger ozone depletion is calculated (more than -40%) with a longer-lasting impact. Very similar results are obtained for the STS scenario. For the scenarios considered, the maximum ozone depletion could be anticipated during the 2010-2020 period for all temperature trends and both PSC schemes. This finding is supported by Shindell et al (1998).

According to the results in Figures V.2 and V.3, ozone recovery in the Arctic is very sensitive to the choice of the "present-day" conditions. The UARS data plays an important role in making a right choice of these conditions, thus providing additional credibility to our and other model predictions.

(VI) Trajectory mapping

VI.1. Introduction and Methodology

Due to the fact that UARS measurements from different instruments are not co-located, it is important to utilize an analysis tool which allows us to obtain synoptic maps from the asynoptic data. Several methods have been developed to produce synoptic maps from asynoptically collected data: Kalman filtering (Haggard, 1986), Fourier

Transform method (Salby, 1982 a, b; Lait and Stanford, 1988), and constituent reconstruction technique (Schoeberl and Lait, 1992). Different from the above methods, trajectory mapping (Morris, et al, 1994) utilizes the meteorological analyses under fewer assumptions to produce synoptic maps by advecting measurements forward and backward. A two-dimensional trajectory model is employed in the Morris et al. study on the isentropic surface for the trajectory mapping.

The "trajectory mapping" technique, which was developed by Morris et al. (1994), has been utilized to generate synoptic maps of trace gas data from asynoptic observations. An in-house trajectory model (kinematic methods following Merrill et al., 1986 and Pickering et al., 1994) has been developed in AER under contract with NASA/ACMAP and the trajectory mapping tool was applied to analyze UARS measurement.

The trajectory mapping technique has several advantages over the other methods. The motions of real atmosphere are incorporated in the calculations. A single measurement can contribute to the constituent fields at different times. Trajectory maps can be generated outside of periods during which measurements are made as long as wind fields exist. Missing points in the constituent measurement relatively have no effects on the mapping.

The trajectory mapping tool also has some disadvantages. First, the quality of a trajectory map substantially depends upon the meteorological analysis. Inaccurate meteorological fields would degrade the quality of the original data. Second, the trajectory maps are not uniformly gridded. But generally, in the analysis of UARS data sets, the trajectory mapping technique generates synoptic maps superior to or comparable to those generated with other methods (Morris et al., 1994).

VI.2. Comparison with Morris et al. results

The comparisons with Morris' et al. results are shown in this section. To apply the trajectory mapping technique, an in-house trajectory model at AER is used to create synoptic maps for UARS data. A set of balanced wind data was used in the trajectory

model. The balanced wind fields were calculated from NMC daily analyses following the method developed by Randel (1987). We concentrate on the same cases as Morris et al. for direct comparisons: CLAES N_2O mapping on September 9, 1992 and MLS H_2O mapping during period of February 18-23, 1993. Morris et al.'s calculations were also based on NMC meteorological data, but different wave numbers were chosen in his calculation of balanced winds.

The measurements during periods of September 6-13, 1992 were used. The data points measured before noon on September 9, 1992 were calculated forwardly using the trajectory model while those measured after noon on September 9, 1992 were done backwardly. The asynoptic map of N_2O at 800K is shown in Figure VI.1a, in which measurements are from 00UT, September 9, to 00UT, September 10 by CLAES. The synoptic maps calculated from AER's and Morris et al.'s trajectory model are shown in Figure VI.1b and Figure VI.1c respectively. The smaller dots represent the parcels added more than 12 hours from the time of the synoptic map while larger dots represent the parcels have been advected by the trajectory models in less than 12 hours. In comparison with the asynoptic map, data coverage is largely improved in the synoptic maps which combine the data of several days. The mapping of N_2O from AER trajectory model is very close to the Morris et al.'s result.

Barnes' scheme was applied to get the gridded product of trajectory map (Barnes, 1964). The result from AER model is shown in Figure VI.2. The wave-breaking event in the middle latitude of Southern Hemisphere is clearly evident from the N_2O synoptic map. The potential vorticity on 800K isentropic surface (calculated from NMC analysis) at 00UT, September 9, 1992, is given in Figure VI.3. If the vortex edge in the southern polar region is defined as $3.0 \times 10^{-4} \frac{K \times m^2}{kg \times s}$ PV contour, we can see that the gradients of N_2O across the vortex boundary are well maintained in the synoptic map (Figure VI.2).

The trajectory mapping technique has been used to study the history of atmospheric events, such as the time sequence of the wave breaking. The large scale intrusion of tropical air to middle and high latitude in the Northern Hemisphere in

February 1993 is detected very well in MLS H₂O data. The sequence synoptic maps of MLS H₂O at 800 K isentropic surface from both AER and Morris trajectory models are shown in Figure VI.4a-b. The low concentration from the tropics (the dots in dark green color) gradually moved to middle and high latitudes (where red color dots are in the background) from February 20, 1993 to February 23, 1993. The thick black line represents 3.0×10^{-4} (Km²/kgs) NMC PV contour line. The gradients of H₂O and NMC PV show high correlations in both results, which provide the validity of trajectory mapping technique.

(VII) Trajectory hunting: Analysis of UARS measurements showing rapid chlorine activation

Trajectory hunting is a technique to find air parcels sampled at least twice over the course of a few days. This technique provides measured initial and final concentrations for such parcels, and allows us to investigate the effects of the chemical processing between initial and final points (since dynamical effects are eliminated). Previously similar approaches have been used for the analysis of the ozonesonde data (von der Gathen et al., 1995; Rex et al., 1998) and for comparison the ER-2 and HALOE measurements (Pierce et al., 1997). Comparison of passive (i.e. long-lived) tracers in the initial and final points along matched parcels could be carried out directly. However, analysis of short-lived species along parcel trajectories requires a photochemical model.

We have utilized UARS the Cryogenic Limb Array Etalon Spectrometer (CLAES) and Microwave Limb Sounder (MLS) data combined with a photochemical box model. This approach looks particularly promising given the large number of measured species (O₃, HNO₃, ClO, ClONO₂, N₂O, CH₄, H₂O) and very frequent sampling (~1300 profiles per day). This study has been performed in cooperation with M.L. Santee (MLS team), J.M. Mergenthaler and J.B. Kumer (CLAES team).

We have applied the trajectory hunting technique to analyze UARS measurements in conjunction with the AER photochemical box model. Our goal is to compare the AER box model representation of photochemical and PSC processes with the UARS measurements for air parcels sampled twice and to check the consistency between CLAES and MLS data. As an example of the trajectory hunting technique application, we investigate rapid chlorine activation in the Arctic on 29 December 1992 at 465K (~46mb) and 585K (~22mb) associated with a polar stratospheric cloud (PSC) event (see Figure VII.1). Details of finding air parcels, sampled twice by UARS, are given in Danilin et al. (1998b).

The AER trajectory box model is initialized using MLS version 4 (v.4) O_3 (profiles and column above 100 hPa) and HNO_3 , prototype non-linear retrievals of MLS H_2O (Pumphrey, 1998), and CLAES v.8 $ClONO_2$, N_2O , and CH_4 . Total inorganic chlorine, Cl_y , is defined from the Cl_y-N_2O correlation according to Woodbridge et al. (1995) using CLAES measurements of N_2O at the initial points; this approach produces 2.0-2.5 ppbv and 2.9 ppbv of Cl_y at 465 K and 585 K, respectively. For all trajectories, ClO is initialized to ClO^{MLS} . Since no HALOE HCl measurements are available for the points of interest, initial HCl is set to $Cl_y - ClONO_2^{CLAES}$. Total inorganic bromine, Br_y , is defined according to Wamsley et al. (1998) with initial $BrO=BrONO_2=Br_y/2$. Since no reliable $NO_x (= NO + NO_2)$ measurements are available for the points considered, we perform a sensitivity study in which NO_x is set to 2 pptv or 0.2 ppbv (based on aircraft measurements (Kawa et al., 1992)), and we assume that initial $NO=NO_2=NO_x/2$. Total reactive nitrogen, NO_y , is taken to be $HNO_3^{MLS} + ClONO_2^{CLAES} + NO_x$. Sulfate aerosol surface area is initialized according to Massie et al. (1998) using the CLAES aerosol extinction measurements at 780 cm^{-1} .

Six air parcels sampled twice and shown in Figure VII.1 were found at both levels. Figure VII.2 compares model results and measurements for ClO and $ClONO_2$ along the air parcel #A at 585K and parcel #a at 465K. Our sensitivity analysis (described in detail in Danilin et al (1998b)) allows us to draw the following conclusions: (1) model results are in better agreement with UARS measurements if the UKMO temperature is decreased by at least 1-2 K; (2) the NAT PSC scheme produce results in better agreement

with observations than the STS scheme; (3) our model can explain the UARS measurements at 585 K, but underestimates the ClO abundance at 465 K. Our stoichiometric calculations (Danilin et al., 1998b) confirms some inconsistency between CLAES v.8 ClONO₂ and MLS v.4 ClO at the 465 K level. It is very likely that the latest versions of MLS (v.5) and CLAES (v.9) will be consistent at this level, mostly due to improvement of the v.5 vertical resolution and reduction of the ClO maximum (M.L. Santee, personal communication).

This study shows that not only measurements could be useful for the validation of model calculations, but also the models could help to look more carefully at the quality of the measurements, especially under difficult for retrieval conditions (like PSC events). Trajectory hunting technique employed in this study could also be used to investigate, for example, mechanisms of denitrification in the polar stratosphere or for extended validation studies of the new instruments and satellites (like SAGE III or EOS MLS). We are planning to continue our cooperation with the MLS and CLAES teams to address these issues.

(VIII) Wave structure of tracers, use of UARS 3B data

VIII.1. Scientific background

The origin of the zonal asymmetries (i.e., eddies) in the trace distributions in the stratosphere, the sources and damping mechanism of the zonal waves, their relations to the planetary waves and to the zonal mean tracer distributions and the interactions between the waves of different tracers are important for understanding the response of atmosphere to the natural and anthropogenic perturbations. Currently, our knowledge in this area is far from complete. In two-dimensional models the longitudinal variations of tracer distributions are not calculated directly and their contribution to the tendency of zonal mean concentration is parameterized as an eddy diffusion. To achieve the parameterization, a series of assumptions and approximations are made. Some of these

are reasonable or can be justified while others are made ad hoc so as to simplify the parameterization.

In principle, the longitudinal variations in tracer distributions can be simulated and related issues can be investigated intensively using 3-D models. However, recent 3-D model simulations show that while the zonal-mean ozone distributions compare well with observations, the simulated longitudinal behavior of ozone distribution are unacceptable (Yung, et al., AGU Fall Meeting, 1996). The spatial and temporal coverage, the quality of the measurements and the variety of the tracers measured simultaneously make the UARS observations a valuable database to study waves in the trace distributions. These studies will help us understand the dynamic and photochemical processes which control the tracer distributions and the responses of the stratosphere to the chemical perturbations. We intend to use the knowledge obtained from these studies to improve the eddy parameterization in 2-D models and to validate 3-D model results. As the first step in this direction, the UARS data has been used to test some assumptions required to derive the eddy diffusion coefficients in AER three-wave interactive model.

VIII.2. The wave equations for tracer

By separating the mixing ratio into zonal mean and eddy in the tracer continuity equations, the resulting linearized tracer eddy equation is:

$$\frac{\partial \mu'}{\partial t} + \bar{u} \frac{\partial \mu'}{\partial x} + \bar{v} \frac{\partial \mu'}{\partial y} + \bar{w} \frac{\partial \mu'}{\partial z} + v' \frac{\partial \bar{\mu}}{\partial y} + w' \frac{\partial \bar{\mu}}{\partial z} = P' - \bar{L} \mu' - \bar{\mu} L' \quad (1)$$

In order to simplify the equation, we assume:

a. $\bar{v} \frac{\partial \mu'}{\partial y} + \bar{w} \frac{\partial \mu'}{\partial z} \ll \bar{u} \frac{\partial \mu'}{\partial x};$

b. $w' \frac{\partial \bar{\mu}}{\partial z} \ll v' \frac{\partial \bar{\mu}}{\partial y};$

c. P' and $-\bar{\mu}L'$ are negligible., thus obtaining (2).

$$\frac{\partial \mu'}{\partial t} + \bar{u} \frac{\partial \mu'}{\partial x} + v' \frac{\partial \bar{\mu}}{\partial y} = -\bar{L} \mu' \quad (2)$$

The eddy of the horizontal wind in the latitudinal direction, v' can be expressed as the sum of waves.

$$v' = \sum_m \sum_l v_m^l e^{i(k_m x - \omega_m^l t)} = \sum_m v_m e^{ik_m x} ,$$

where

$$k_m = \frac{m}{a \cdot \cos \theta} \quad \text{and} \quad v_m = \sum_l v_m^l e^{-i\omega_m^l t} , \quad (3)$$

and m is the wave number and the summation of l is over waves with different frequencies but the same wave number m . Accordingly, the solution for Eqn. (2) can be written as

$$\mu' = \sum_m \sum_l \mu_m^l e^{i(k_m x - \omega_m^l t)} = \sum_m \mu_m e^{ik_m x} , \quad \text{where} \quad \mu_m = \sum_l \mu_m^l e^{-i\omega_m^l t} , \quad (4)$$

with

$$\mu_m = \left(\sum_l \frac{v_m^l}{i(\omega_m^l - \bar{u}k_m - i\bar{L})} e^{-i\omega_m^l t} \right) \cdot \frac{\partial \bar{\mu}}{\partial y} ,$$

$$\mu_m^l = \frac{v_m^l}{i(\omega_m^l - \bar{u}k_m - i\bar{L})} \cdot \frac{\partial \bar{\mu}}{\partial y} . \quad (5)$$

The magnitudes of v_m^l and μ_m^l are the wave amplitude for wind and tracer respectively. They are the function of the time, latitude and altitude. From Eqn. (5), the tracer wave amplitude $|\mu_m^l|$ is proportional to the wave amplitude of wind $|v_m^l|$. So the tracer waves and wind wave have the same decaying rate, which is one of the assumptions required in the eddy diffusion parameterization (Garcia, et al., 1992; Shia, et al., 1998). Equation (5)

can be simplified for inert tracers (e.g., SF₆ and CO₂, O₃) since the right-hand side of Eqn. (2) can be neglected, given Eqn. (6):

$$\frac{\partial \mu'}{\partial t} + \bar{u} \frac{\partial \mu'}{\partial x} + v' \frac{\partial \bar{\mu}}{\partial y} = 0, \quad (6)$$

and its solution is

$$\mu' = \sum_m \sum_l \mu_m^l e^{i(k_m x - \omega_m^l t)} = \sum_m \mu_m e^{i k_m x},$$

where

$$\mu_m^l = \frac{v_m^l}{i(\omega_m^l - \bar{u} k_m)} \cdot \frac{\partial \bar{\mu}}{\partial y}. \quad (7)$$

For two long-lived species μ and χ ,

$$\mu_m^l / \frac{\partial \bar{\mu}}{\partial y} = \chi_m^l / \frac{\partial \bar{\chi}}{\partial y} = \sum_l \frac{v_m^l}{i(\omega_m^l - \bar{u} k_m)} e^{-i \omega_m^l t}. \quad (8)$$

However, as described in the sub-appendix, very small difference in the L's will invalidate the relationship in Eqn. (8). In the next section, we examine the UARS data to see if Eqn. (8) is satisfied for N₂O and CH₄

VIII.3. Tracer waves in UARS observations

We use UARS data to test whether the tracer waves and wind wave have the same decaying rate as shown in Eqn. (7). Because the suitable data for the horizontal wind are not immediately available, we compare the wave amplitudes of different species. The assumption implies that they should have the same time dependency if they are generated by the same planetary waves. Usually, in order to identify every single wave μ_m^l , the UARS 3A data are analyzed using the algorithms (Kalman 1961 a,b; Salby 1982a, b) developed for asymptotically gathered data. However, the UARS 3B data supplies the

daily waves $\mu_m = \sum_l \mu_m^l e^{-i\omega_m^l t}$ for wave number $m = 0$ to 6, at the selected latitudes and altitudes for different tracers. They can be used to test Eqn. (8). We have examined two time periods at the lower stratosphere that are known to have strong waves and one of them is shown here. Plotted in Figure VIII. 1-3 is the magnitude of $\mu_m / \left\langle \frac{\partial \bar{\mu}}{\partial y} \right\rangle$ for N_2O and CH_4 at 46 hPa, for different time periods. In the expression, μ_m is the amplitude of the daily waves from UARS 3B data and $\left\langle \frac{\partial \bar{\mu}}{\partial y} \right\rangle$ is the time averaged latitudinal gradient over the 28 day period. It can be seen that the amplitudes of N_2O and CH_4 follow each other very well at 56°N . and 68°N . This shows that the planetary waves in these regions are the source of the waves in the tracer distributions . The situation is less satisfactory at 44°N . It is probably due to the interference of waves with different frequencies (μ_m^l with different l). This work is still in progress.

Sub Appendix: Wave Interference

We will demonstrate in this Appendix that a small difference in the local chemical loss rate, \bar{L} can destroy the relation between the wave amplitudes of two species shown in Eqn. (8). In order to simplify the process, we assume that the zonal mean zonal velocity $\bar{u} = 0$ and one of the species is inert. Also we assume that there are only two waves for the wave number m , and their frequency are ω^1 and ω^2 , generated by the planetary waves v^1 and v^2 respectively. Now the ratio of their amplitudes, after being divided by the latitudinal gradient, is

$$\left(\frac{v^1 \cdot e^{i\omega^1 t}}{i\omega^1} + \frac{v^2 \cdot e^{i\omega^2 t}}{i\omega^2} \right) / \left(\frac{v^1 \cdot e^{i\omega^1 t}}{i(\omega^1 - i\bar{L})} + \frac{v^2 \cdot e^{i\omega^2 t}}{i(\omega^2 - \bar{L})} \right) =$$

$$\left(1 + \frac{v^2 \omega^1}{v^1 \omega^2} e^{i(\omega^2 - \omega^1)t}\right) / \left(\frac{1}{(1 - i \frac{\bar{L}}{\omega^1})} + \frac{1}{(1 - i \frac{\bar{L}}{\omega^2})} \frac{v^2 \omega^1}{v^1 \omega^2} e^{i(\omega^2 - \omega^1)t} \right).$$

For $\bar{L} = 0$ the ratio is 1. If \bar{L} is not equal to zero, the ratio changes with time. For long-lived species, \bar{L} is much smaller than ω 's, and the ratio can be expressed as

$$\left(1 + \frac{v^2 \omega^1}{v^1 \omega^2} e^{i(\omega^2 - \omega^1)t}\right) / \left((1 + i \frac{\bar{L}}{\omega^1}) + (1 + i \frac{\bar{L}}{\omega^2}) \frac{v^2 \omega^1}{v^1 \omega^2} e^{i(\omega^2 - \omega^1)t} \right)$$

The magnitude of this ratio can be far away from 1 even \bar{L} / ω 's is much small than 1. As a special case, e. g. $\frac{v^2 \omega^1}{v^1 \omega^2} = 1$. Then for some special moments, ($e^{i(\omega^2 - \omega^1)t} = -1$), the amplitude of the first species, $\left(1 + \frac{v^2 \omega^1}{v^1 \omega^2} e^{i(\omega^2 - \omega^1)t}\right)$ is equal to zero (This is the results of wave interference). However, at the same time the amplitude of the other species is $\left(\frac{\bar{L}}{\omega^1} - \frac{\bar{L}}{\omega^2}\right)$, which is not equal to zero.

(IX) References

- Barnes, S.L., A technique for maximizing details in numerical weather map analysis, *J. Appl. Meteorology*, **3**, 396, 1964.
- Bekki, S. and J.A. Pyle, A two-dimensional modeling study of the volcanic eruption of Mount Pinatubo, *J. Geophys. Res.*, **99**, 18,862-18,869, 1994.
- Boville, B.A., J.R. Holton, and P.W. Mote, Simulation of the Pinatubo aerosol cloud in GCM, *Geophys. Res. Lett.*, **18**, 2281-2284, 1991.
- Brasseur, G.P. and C. Granier, Mount Pinatubo aerosols, chlorofluorocarbons, and ozone depletion, *Science*, **257**, 1239-1242, 1992.
- Crutzen, P.J., et al., A reevaluation of the ozone budget with HALOE UARS data: No evidence for the ozone deficit, *Science*, **268**, 705, 1995.
- Danilin, M.Y., and J.C. McConnell, Stratospheric effects of bromine activation on/in sulfate aerosol, *J. Geophys. Res.*, **100**, 11-237-11,234, 1995.
- Danilin, M.Y. et al., Stratospheric cooling and Arctic ozone recovery, *Geophys. Res. Lett.*, **25**, 2141-2144, 1998a.
- Danilin, M.Y., et al. Trajectory hunting: Analysis of UARS measurements showing rapid chlorine activation, *Geophys. Res. Lett.*, submitted, 1998b.
- Danilin, M.Y. et al. Nitrogen species in the post-Pinatubo stratosphere: Model analysis utilizing UARS measurements, *J. Geophys. Res.*, submitted 1998c
- Danilin, M.Y., N.D. Sze, M.K.W. Ko, J.M. Rodriguez, and M.J. Prather, Bromine-chlorine coupling in the Antarctic ozone hole, *Geophys. Res. Lett.*, **23**, 153-156, 1996.
- David, S.J., F.J. Murcray, A. Goldman, C.P. Rinsland, and D.G. Murcray, The effect of the Mt. Pinatubo aerosol on the HNO₃ column over Mauna Loa, Hawaii, *Geophys. Res. Lett.*, **21**, 1003-1006, 1994.
- DeMore, W.B. et al, Chemical kinetics and photochemical data for use in stratospheric modeling. Evaluation number 11. JPL Publication 94-26, 1994.
- DeMore, W.B. et al, S.P. Sander, D.M. Golden, R.F. Hampson, M.J. Kurylo, C.J. Howard, A.R. Ravishankara, C.E. Kolb, and M.J. Molina, Chemical kinetics and photochemical data for use in stratospheric modeling. Evaluation number 12. JPL-Publication 97-4, 1997.

- Dessler, A.E. et al., A test of the partitioning between ClO and ClONO₂ using simultaneous UARS measurements of ClO, NO₂, and ClONO₂, *J. Geophys. Res.*, **101**, 12,515-12,521, 1996.
- Dessler, A.E., et al., Correlated observations of HCl and ClONO₂ from UARS and implications for stratospheric chlorine partitioning, *Geophys. Res. Lett.*, **22**, 1721-1724, 1995.
- Dessler, A.E., et al., Selected science highlights from the first 5 years of the UARS program, *Rev. Geophys.*, **36**, 183-210, 1998.
- Donahue, N.M., M.K. Dubey, R. Mohrschladt, K.L. Demerjian, and J.G. Anderson, High-pressure flow study of the reactions OH + NO_x → HONO_x: Errors in the falloff region, *J. Geophys. Res.*, **102**, 6159-6168, 1997.
- Fahey, D.W. et al., A diagnostic for denitrification in the winter polar stratosphere, *Nature*, **345**, 698-702, 1990.
- Fahey, D.W. et al., *In situ* measurements constraining the role of sulfate aerosols in mid-latitude ozone depletion, *Nature*, **363**, 509-514, 1993.
- Gao, R.S. et al., Partitioning of the reactive nitrogen reservoir in the lower stratosphere of the southern hemisphere: Observations and modeling, *J. Geophys. Res.*, **102**, 3935-3949, 1997.
- Garcia, R.R., F. Strodal, S. Solomon, and J.F. Kiehl, A new numerical model of the middle atmosphere 1. Dynamics and transport of tropospheric source gases, *J. Geophys. Res.*, **97**, 12,967-12,991, 1992.
- Gille, J.C., et al., Accuracy and precision of the nitric acid concentrations determined by the limb infrared monitor of the stratosphere experiment on Nimbus 7, *J. Geophys. Res.*, **89**, 5179-5190, 1984.
- Haggard, K. V., E. E. Remsberg, et al, Description of Data on the Nimbus 7 LIMS Map Archival Tape, Technical Report No. 2553, NASA, 1986.
- Hanson, D.R., A. R. Ravishankara, and E.R. Lovejoy, Reaction of BrONO₂ with H₂O on submicron sulfuric acid aerosol and the implications for the lower stratosphere, *J. Geophys. Res.*, **101**, 9063-9069, 1996.
- Jackman, C.H., et al., An intercomparison of nitrogen-containing species in Nimbus 7, LIMS and SAMS data, *J. Geophys. Res.*, **92**, 995-1008, 1987.

- Johnston, P.V. et al., Observations of depleted stratospheric NO₂ following the Pinatubo volcanic eruption, *Geophys. Res. Lett.*, **19**, 211-213, 1992.
- Jucks, K.W., D.G. Johnson, K.V. Chance, W.A. Traub, R.J. Salawitch, and R.A. Stachnik, Ozone production and loss rate measurements in the middle stratosphere, *J. Geophys. Res.*, **101**, 28,785-28,792, 1996.
- Kalman, R. E. and R.S. Bucy, New Results in Linear Filtering and Prediction Theory. Trans. ASME, Ser. D, J. Basic Eng., 83:95-108, 1961a.
- Kalman, R. E., A New Approach to Linear Filtering and Prediction Problems. Trans. ASME, Ser. D, J. Basic Eng., 82:35-45, 1961b.
- Kawa, S.R., et al., Interpretation of NO_x/NO_y observations from AASE-II using a model of chemistry along trajectories, *Geophys. Res. Lett.*, **20**, 2507-2510, 1993.
- Kawa, S.R., et al., Photochemical partitioning of the reactive nitrogen and chlorine reservoirs in the high-latitude stratosphere, *J. Geophys. Res.*, **97**, 7905-7923, 1992.
- Kaye, J.A. and T.L. Miller, The ATLAS series of Shuttle missions, *Geophys. Res. Lett.*, **23**, 2285-2288, 1996.
- Keim, E.R., et al., Measurements of the NO_y-N₂O correlation in the lower stratosphere: Latitudinal and seasonal changes and model comparisons, *J. Geophys. Res.*, **102**, 13,193-13,212, 1997.
- Kinnison, D.E. et al., The chemical and radiative effects of the Mt. Pinatubo eruption, *J. Geophys. Res.*, **99**, 22,705-22,731, 1994.
- Koike, M. et al., Decrease of stratospheric NO₂ at 44°N caused by Pinatubo volcanic aerosols, *Geophys. Res. Lett.*, **20**, 1975-1978, 1993.
- Koike, M., N. B. Jones, W. A. Matthews, P. V. Johnston, R. L. McKenzie, D. Kinnison and J. Rodriguez, Impact of Pinatubo Aerosols on the Partitioning between NO₂ and HNO₃, *Geophys. Res. Lett.*, **21**, 597-600, 1994.
- Koike, M., Y. Kondo, W.A. Matthews, P.V. Johnston, H. Nakajima, A. Kawaguchi, H. Nakane, I. Murata, A. Budiyno, M. Kanada, and N. Toriyama, Assessment of the uncertainties in the NO₂ and O₃ measurements by visible spectrometers, *J. Atmos. Chem.*, in press, 1998.

- Kondo, Y., et al., Effect of Pinatubo aerosol on stratospheric NO, *J. Geophys. Res.*, **102**, 1205-1213, 1997.
- Kondo, Y., et al., NO_y correlation with N₂O and CH₄ in the mid-latitude stratosphere, *Geophys. Res. Lett.*, **23**, 2369-2372, 1996.
- Kondo, Y., et al., Partitioning of reactive nitrogen in the midlatitude lower stratosphere, *J. Geophys. Res.*, to be submitted, 1998.
- Kumer, J.B., et al., Comparison of CLAES preliminary N₂O₅ data with correlative data and a model, *J. Geophys. Res.*, **101**, 9657-9677, 1996.
- Lait, L.R. and J.L. Stanford, Applications of Asynoptic Space-Time Fourier Transform Methods to Scanning Satellite Measurements. *J. Atmos. Sci.*, **45**, 3784-3799, 1988.
- Lambert, A., et al., Global evolution of the Mt. Pinatubo volcanic aerosols observed in the infrared limb-sounding instruments CLAES and ISAMS on the UARS, *J. Geophys. Res.*, **102**, 1495-1512, 1997.
- Lary, D.J., M.P. Chipperfield, R. Toumi, and L. Lenton, Heterogeneous atmospheric bromine chemistry, *J. Geophys. Res.*, **101**, 1489-1504, 1996.
- Loewenstein, M. et al., New observations of the NO_y/N₂O correlation in the lower stratosphere, *Geophys. Res. Lett.*, **20**, 2531-2534, 1993.
- Massie, S.T., et al., Estimation of PSC volume and area densities from UARS, SAM II, and POAM II extinction data, *J. Geophys. Res.*, **103**, 5773-5783, 1998.
- McKenzie, R.L., P.V. Johnston, C.T. McElroy, J.B. Kerr, and S. Solomon, Altitude distributions of stratospheric constituents from ground-based measurements at twilight, *J. Geophys. Res.*, **96**, 15,499-15,511, 1991.
- Merrill, J. T., R. Bleck and D. Boudra, Techniques of Lagrangian Trajectory Analysis in Isentropic Coordinates. *Mon. Wea. Rev.*, **114**, 571-581, 1986.
- Michelsen, H. A., R. J. Salawitch, M. R. Gunson, C. Aellig, N. Kampfer, M. M. Abbas, M. C. Abrams, T. L. Brown, A. Y. Chang, A. Goldman, F. W. Irion, M. J. Newchurch, C. P. Rinsland, G. P. Stiller, and R. Zander, Stratospheric chlorine partitioning: Constraints from shuttle-borne measurements of [HCl], [ClNO₃], and [ClO]. *Geophys. Res. Lett.* **23**, 2361 (1996).

- Michelsen, H.A., G.L. Manney, M.R. Gunson, C.P. Risland, and R. Zander, Correlations of stratospheric CH₄ and N₂O derived from ATMOS measurements made during the ATLAS space shuttle missions, *Geophys. Res. Lett.*, **25**, 2777-2780, 1998.
- Mills, M.J. et al., On the relationship between stratospheric aerosols and nitrogen dioxide, *Geophys. Res. Lett.*, **20**, 1187-1190, 1993.
- Morris, G. A, A Demonstration and Evaluation of Trajectory Mapping, Ph.D. thesis, Rice University, 1994.
- Morris, G.A., et al., Nitrogen partitioning in the middle stratosphere as observed by UARS, *J. Geophys. Res.*, **102**, 8955-8965, 1997.
- Noltholt, J., The Moon as a light source for FTIR measurements of stratospheric trace gases during the polar night: Application for HNO₃ in the Arctic, *J. Geophys. Res.*, **99**, 3607-3614, 1994.
- Osterman, G.B. et al., Balloon-borne measurements of stratospheric radicals and their precursors: Implications for the production and loss of ozone, *Geophys. Res. Lett.*, **24**, 1107-1110, 1997.
- Pickering, K. E. and A. M. Thompson, D. P. McNamara and M. R. Schoeberl, An Intercomparison of Isentropic Trajectories over the South Atlantic. *Mon. Wea. Rev.*, **122**, 864-879, 1994.
- Pierce, R.B., et al., Photochemical calculations along air mass trajectories during ASHOE/MAESA, *J. Geophys. Res.*, **102**, 13,153-13,168, 1997.
- Pitari, G. and V. Rizi, An estimate of the chemical and radiative perturbation of stratospheric ozone following the eruption of Mt. Pinatubo, *J. Atmos. Sci.*, **50**, 3260-3276, 1993.
- Plumb, R.A. and M.K.W. Ko, Interrelationships between mixing ratios of long-lived stratospheric constituents, *J. Geophys. Res.*, **97**, 10,145-10,156, 1992.
- Prather, M.J. and E.E. Remsberg (eds), The atmospheric effects of stratospheric aircraft: report of the 1992 models and measurements workshop, NASA Ref. Publ. 1292, vol.III, Chapter H, 1993.
- Preston, K.E., R.L. Jones, and H.K. Roscoe, Retrieval of NO₂ vertical profiles from ground-based UV-visible measurements: Method and validation, *J. Geophys. Res.*, **102**, 19,089-19,098, 1997.

- Pumphrey, H.C., Validation of a new prototype water vapor retrieval for UARS MLS, *J. Geophys. Res.*, submitted, 1998.
- Ramaswamy, V. et al., Fingerprint of ozone depletion in the spatial and temporal pattern of recent lower-stratospheric cooling, *Nature*, **382**, 616, 1996.
- Randel, W. J., The Evolution of Winds from Geopotential Height Data in the Stratosphere. *J. Atmos. Sci.*, **44**, 3097-4120, 1987.
- Randel, W.J. and J.B. Cobb, Coherent variations of monthly mean total ozone and lower stratospheric temperature, *J. Geophys. Res.*, **99**, 5433, 1994.
- Reber, C.A., et al., The upper atmosphere research satellite mission, *J. Geophys. Res.*, **98**, 10,643-10,647, 1993.
- Renard, J-B., et al., Nocturnal vertical distribution of stratospheric O₃, NO₂, and NO₃ from balloon measurements, *J. Geophys. Res.*, **101**, 28,793-28,804, 1996.
- Renard, J-B., et al., Vertical distribution of night-time stratospheric NO₂ from balloon measurements: comparison with models, *Geophys. Res. Lett.*, **24**, 73-76, 1997.
- Rex, M. et al., *In situ* measurements of stratospheric ozone depletion rates in the Arctic winter 91/92: A Lagrangian approach, *J. Geophys. Res.*, **103**, 5843-5853, 1998.
- Ridley, B.A., et al., Seasonal differences in the vertical distributions of NO, NO₂, and O₃ near 50°N, *J. Geophys. Res.*, **92**, 11,919-11,929, 1987.
- Ridley, B.A., et al., Stratospheric add nitrogen: measurements of HNO₃, NO, NO₂, and O₃ near 54°N in winter, *J. Geophys. Res.*, **89**, 4797-4820, 1984.
- Rinsland, C.P. et al., Heterogeneous conversion of N₂O₅ to HNO₃ in the post-Mt. Pinatubo eruption stratosphere, *J. Geophys. Res.*, **99**, 8213-8219, 1994.
- Roche, A.E. et al., Validation of CH₄ and N₂O measurements by the CLAES instrument on the UARS, *J. Geophys. Res.*, **101**, 9679-9710, 1996.
- Rodriguez, J.M. et al., Ozone response to enhanced heterogeneous processing after the eruption of Mt. Pinatubo, *Geophys. Res. Lett.*, **21**, 209-212, 1994.
- Rodriguez, J.M., M.K.W. Ko, and N.D. Sze, Role of heterogeneous conversion of N₂O₅ on sulfate aerosol in global ozone loss, *Nature*, **352**, 134-137, 1991.
- Rood, R.B., A.R. Douglass, J.A. Kaye, and D.B. Considine, Characteristics of wintertime and autumn nitric acid chemistry as defined by LIMS data, *J. Geophys. Res.*, **98**, 18,533-18,545, 1993.

- Rosenfeld, J.E. et al., Computations of diabatic descent in the stratospheric polar vortex, *J. Geophys. Res.*, **99**, 16677, 1994.
- Rosenfeld, J.E., et al., Stratospheric effects of Mount Pinatubo aerosol studied with a coupled 2-D model, *J. Geophys. Res.*, **102**, 3649-3670, 1997.
- Russell, J.M. III, et al., The variability of stratospheric and mesospheric NO₂ in the polar winter night observed by LIMS, *J. Geophys. Res.*, **89**, 7267-7275, 1984.
- Salawitch, R.J. et al., The distribution of HO_x, NO_x, and Cl_x radicals in the lower stratosphere: Implications for changes in O₃ due to emission of NO_y from supersonic aircraft, *Geophys. Res. Lett.*, **21**, 2547, 1994.
- Salby, M. L., Sampling Theory for Asynoptic Satellite Observations. Part I: Space-Time Spectra, Resolution and Aliasing, *J. Atmos. Sci.* **39**, 2577-2600, 1982a.
- Salby, M. L., Sampling Theory for Asynoptic Satellite Observations. Part II: Fast Fourier Synoptic Mapping, *J. Atmos. Sci.*, **39**, 2601-2614, 1982b.
- Santee, M. L. , R.J. Salawitch, G. L. Manney, W. G . Read, L. Froidevaux, J . E. Waters , and A. Tabazadeh, Microwave limb sounder HNO₃ observations: implications for PSC compositions, *Abstract submitted to Quadr. Ozone Symp., Italy, Sept. 1996.*
- Schoeberl M. R. and L. R. Lait, Conservative Coordinate Transformations for Atmospheric Measurements, Proceedings of the International School of Physics; The use of EOS for Studies of Atmospheric Physics', New York, Elsevier Science Publishing Company, Inc., 1992.
- Sen, B. et al., Measurements of reactive nitrogen in the stratosphere, *J. Geophys. Res.*, **103**, 3571-3585, 1998.
- Shia, R.L., S. Zhou, M.K.W. Ko, N.D. Sze, D. Salstein, and K. Cady-Pereira, A three-wave model of the stratosphere with coupled dynamics, radiation and photochemistry, in preparation, 1998.
- Shindell, D.W. et al., Increased polar stratospheric ozone losses and delayed eventual recovery owing to increasing greenhouse gas concentrations, *Nature*, **392**, 589, 1998.
- Slusser, J., et al., High-latitude stratospheric NO₂ and HNO₃ over Fairbanks (65°N) 1992-1994, *J. Geophys. Res.*, **103**, 1549-1554, 1998.

- Slusser, J.R., D.J. Fish, E.K. Strong, R.L. Jones, H.K. Roscoe, and A. Sarkissian, Five years of NO₂ vertical column measurements at Faraday (65°S): Evidence for the hydrolysis of BrONO₂ on Pinatubo aerosol, *J. Geophys. Res.*, **102**, 12,987-12,993, 1997.
- Solomon, S. et al., The role of aerosol variations in anthropogenic ozone depletion at northern midlatitudes, *J. Geophys. Res.*, **101**, 6713-6727, 1996.
- Thomason, L.W., L.R. Poole, and T. Deshler, A global climatology of stratospheric aerosol surface area density deduced from SAGE II measurements: 1984-1994, *J. Geophys. Res.*, **102**, 8967-8976, 1997.
- Tie, X.X. et al., Two-dimensional simulation of Pinatubo aerosol and its effect on stratospheric ozone, *J. Geophys. Res.*, **99**, 20,545-20,562, 1994.
- Van Roozendaal, M., et al., Ground-based observations of stratospheric NO₂ at high and mid-latitudes in Europe after the Mt Pinatubo eruption, *J. Geophys. Res.*, **102**, 19,171-19,176, 1997.
- von der Gathen, P. et al., Observational evidence for chemical ozone depletion over the Arctic in winter 1991-92, *Nature*, **375**, 131-134, 1995.
- Wamsley, P.R., et al., Distribution of halon-1211 in the upper troposphere and lower stratosphere and the 1994 total bromine budget, *J. Geophys. Res.*, **103**, 1513-1526, 1998.
- Weisenstein, D.K., et al., A two dimensional model of sulfur species and aerosols, *J. Geophys. Res.*, **102**, 13,019-13,035, 1997.
- Wennberg, P.O. et al., Removal of stratospheric O₃ by radicals in situ measurement of OH, HO₂, NO, NO₂, ClO and BrO, *Science*, **266**, 398, 1994.
- Woodbridge, E.L., et al., Estimates of total organic and inorganic chlorine in the lower stratosphere from *in situ* and flask measurements during AASE II, *J. Geophys. Res.*, **100**, 3057-3064, 1995.
- Yue, G.K., L.R. Poole, Stratospheric aerosol acidity, density, and refractive index deduced from SAGE II and NMC temperature data, *J. Geophys. Res.*, **99**, 3727-3738, 1994.
- Yung, Y.L., Y. Jiang and Z. Hu, Climatology of longitudinal structure of column ozone from TOMS, AGU Fall Meeting, 1996.

Percentage Contribution to NO_y (HALOE, CLAES data in July 92 30N-40N)

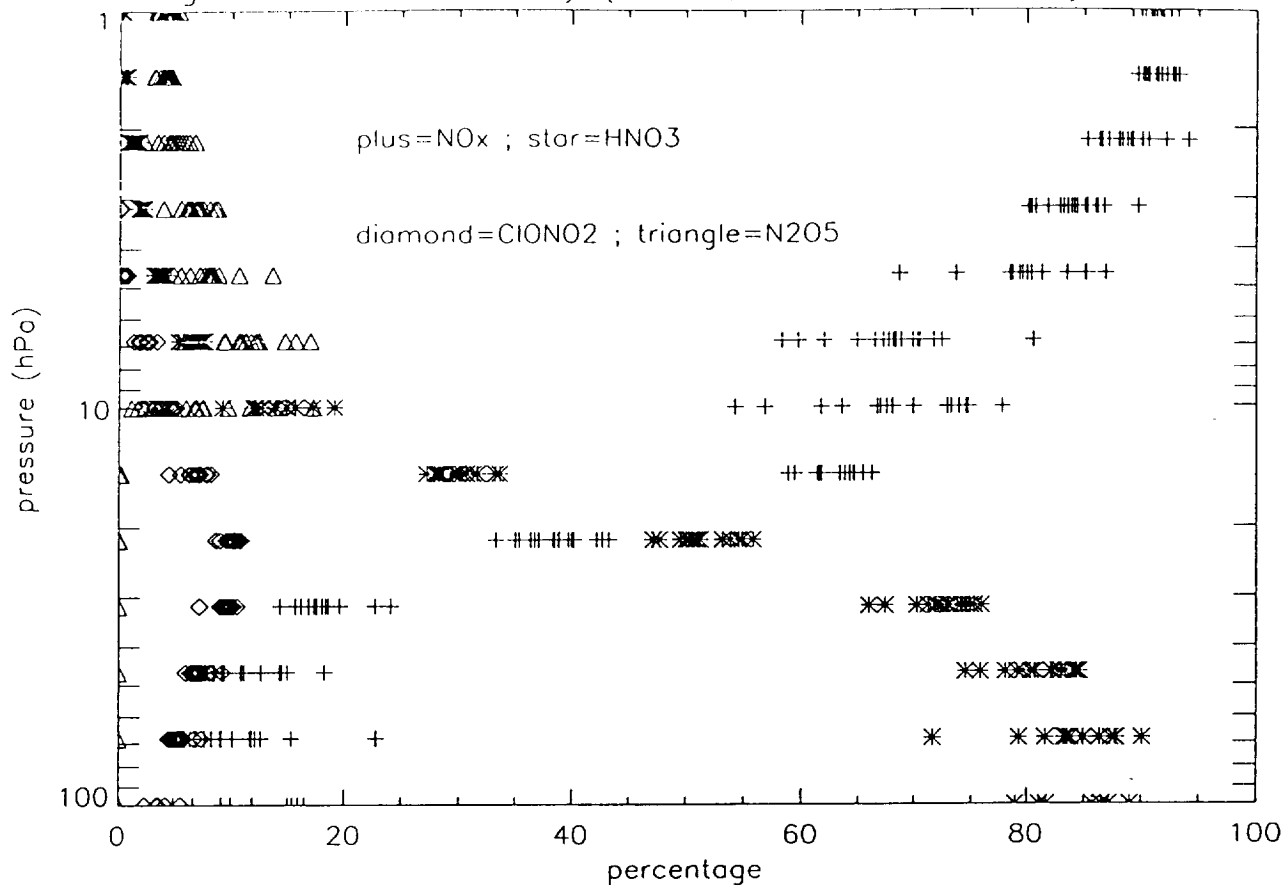


Figure II.1: The percentage contributions to NO_y from NO_x (NO+NO₂), HNO₃, ClONO₂ and N₂O₅ from UARS HALOE and CLAES measurement in July, 1992 between 30°N-40°N.

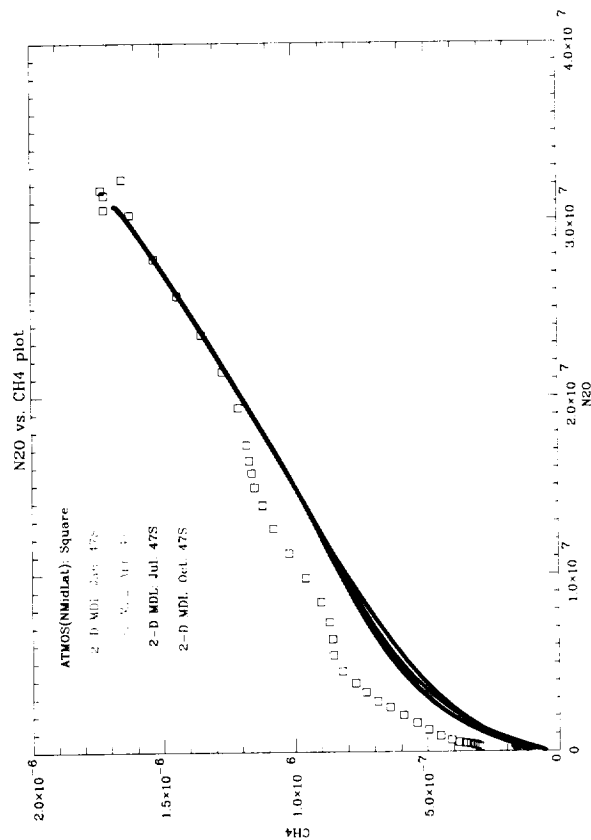
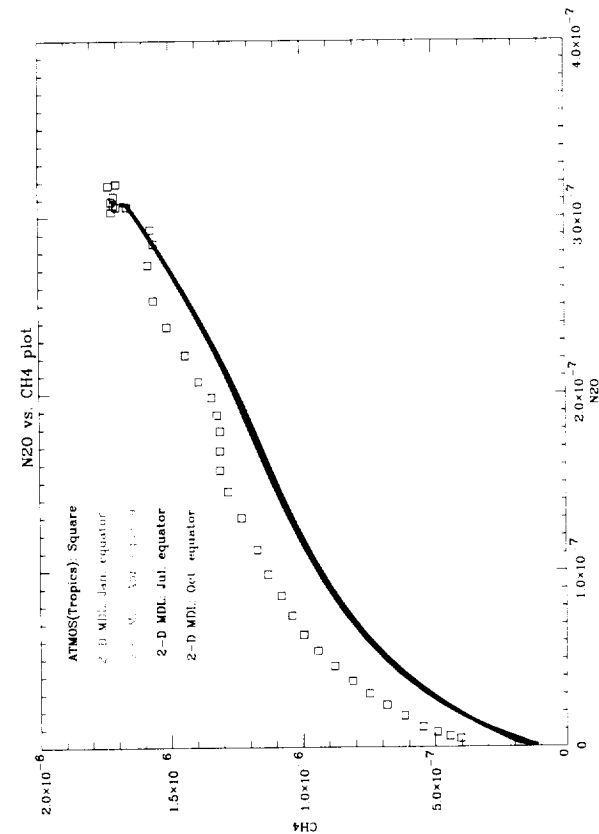
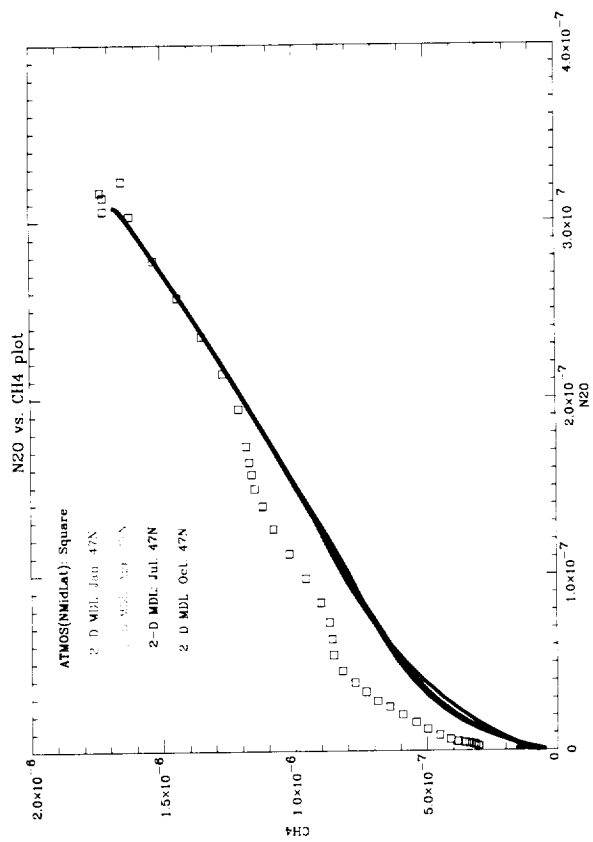


Figure II.2: N_2O vs CH_4 correlation from ATMOS and AER 2-D model in January, April, July and October at 47°N (a), equator (b), and 47°S (c).

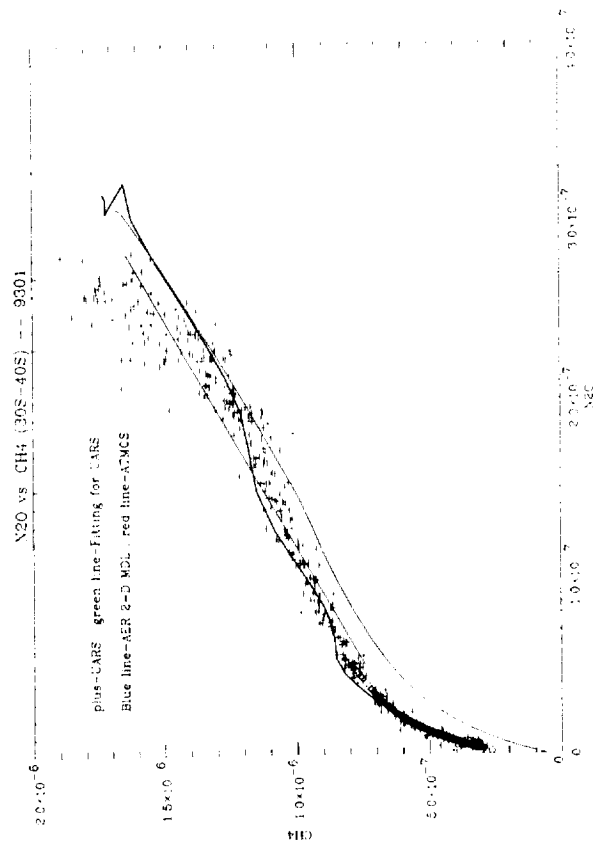
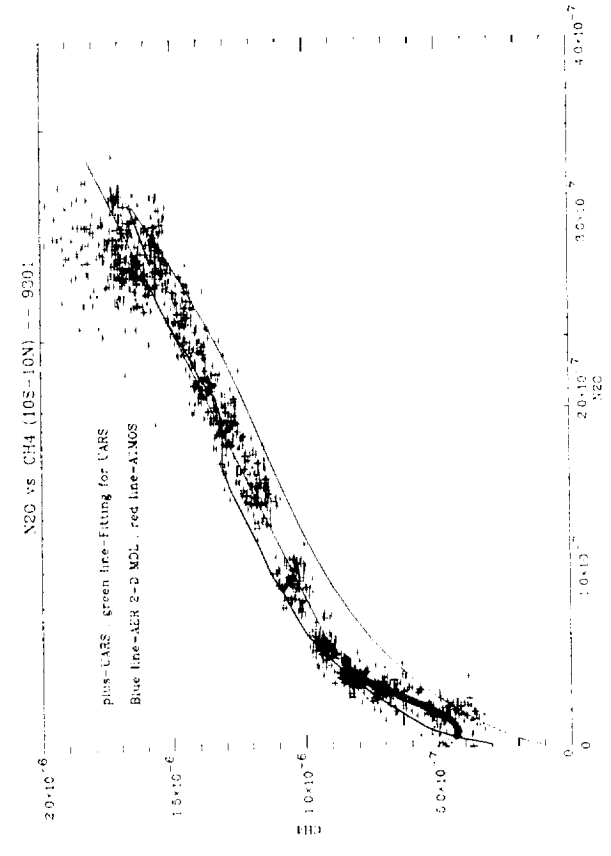
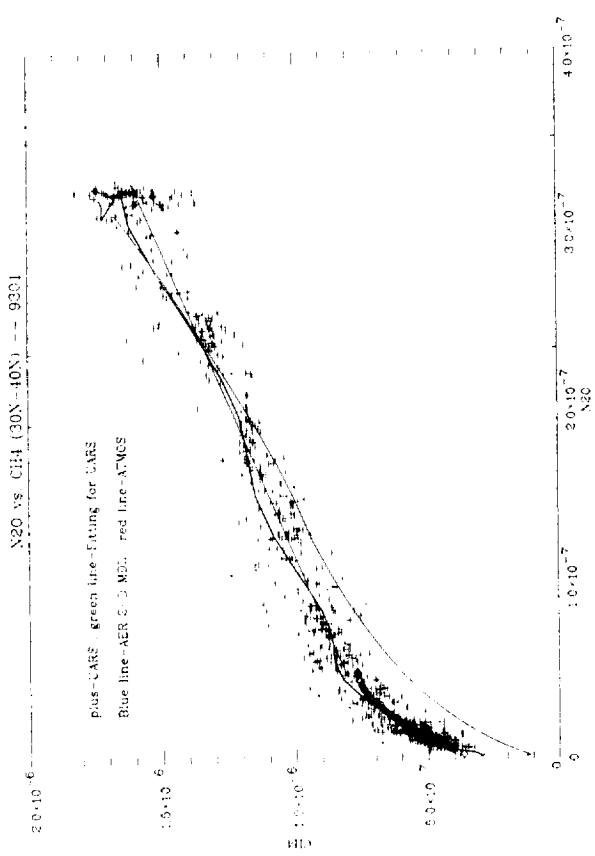


Figure II.3: N₂O vs CH₄ correlation from UARS measurements in January, at 30°N-40°N(a), 10°N-10°S(b), and 30°S-40°S (c) in comparison with ATMOS, and AER 2-D model output (using data at 38°N (a), Equator (b) and 38°S (c) respectively).

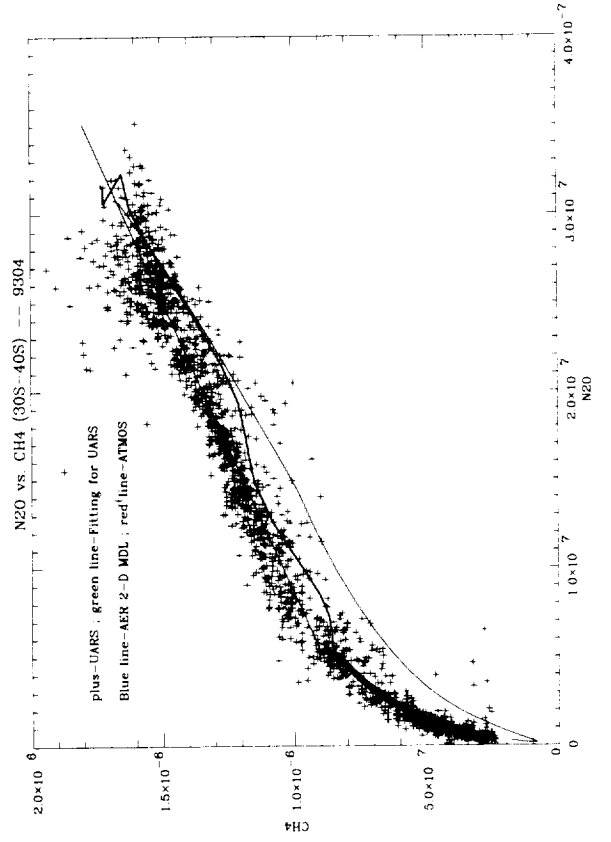
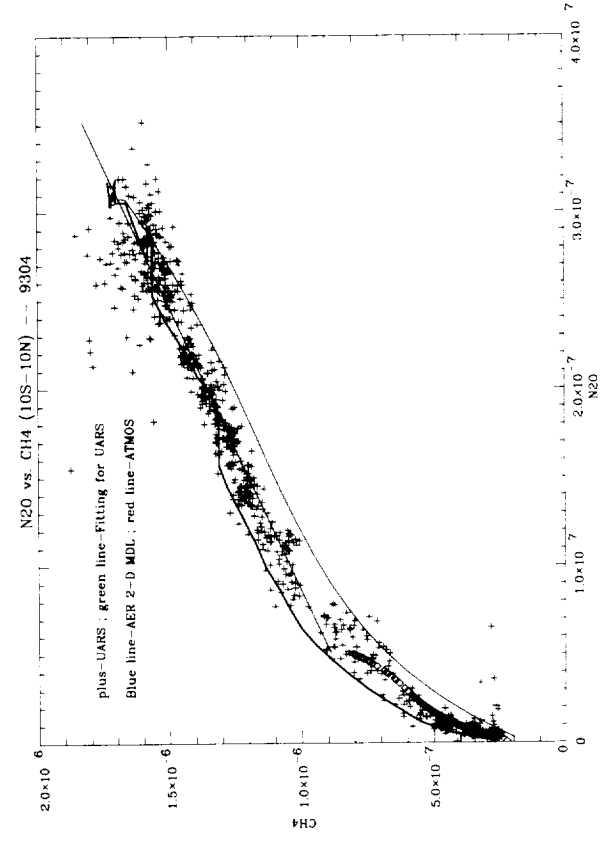
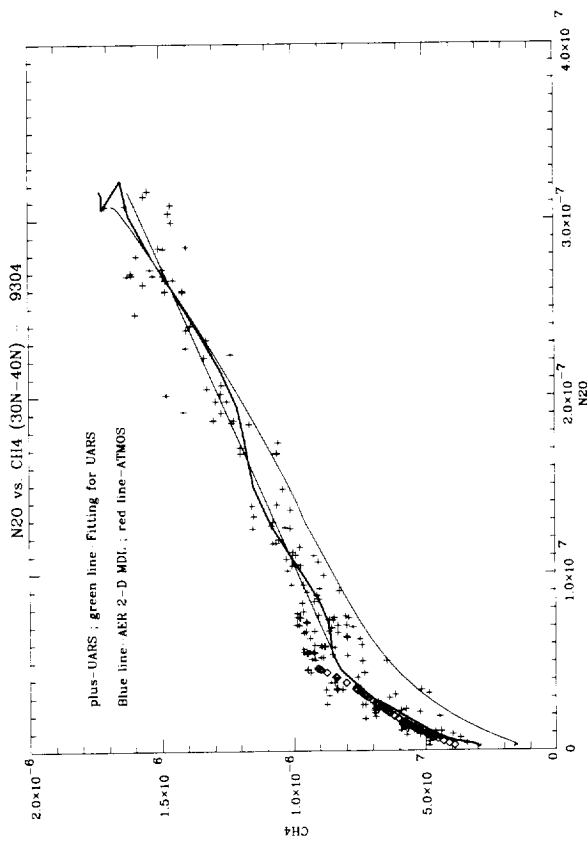


Figure II.4: N_2O vs CH_4 correlations from UARS measurements in April, at $30^\circ N-40^\circ N$ (a), $10^\circ N-10^\circ S$ (b), and $30^\circ S-40^\circ S$ (c) in comparison with ATMOS, and AER 2-D model output (using data at $38^\circ N$ (a), Equator (b) and $38^\circ S$ (c) respectively).

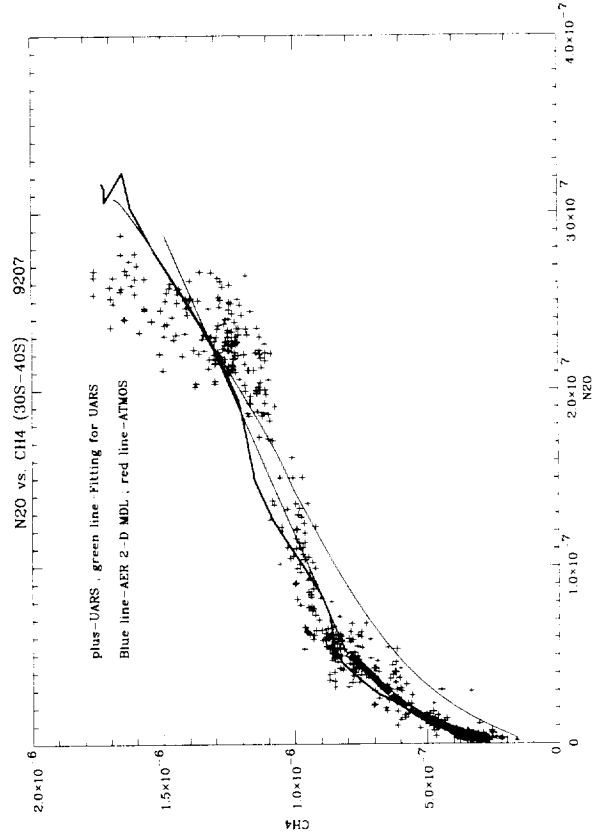
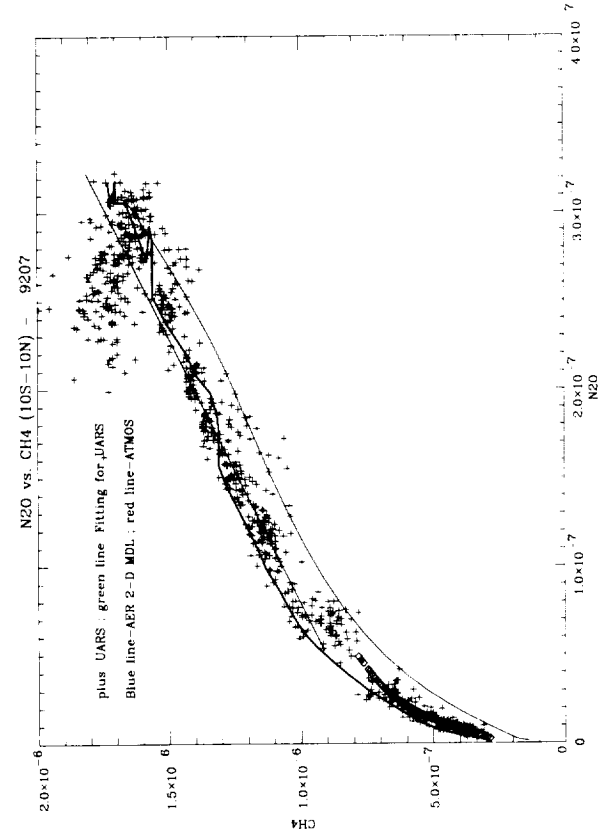
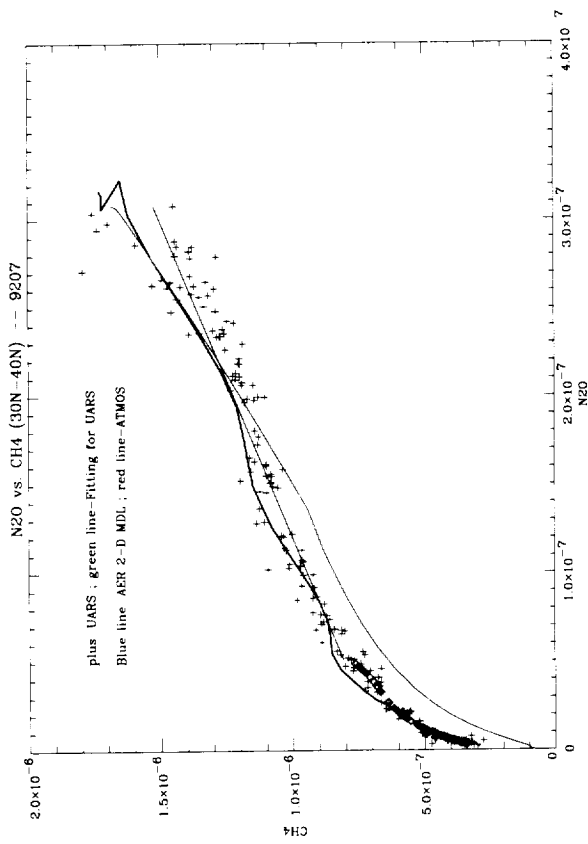


Figure II.5: N_2O vs CH_4 correlations from UARS measurements in July, at $30^\circ N-40^\circ N$ (a), $10^\circ N-10^\circ S$ (b), and $30^\circ S-40^\circ S$ (c) in comparison with ATMOS, and AER 2-D model output (using data at $38^\circ N$ (a), Equator (b) and $38^\circ S$ (c) respectively).

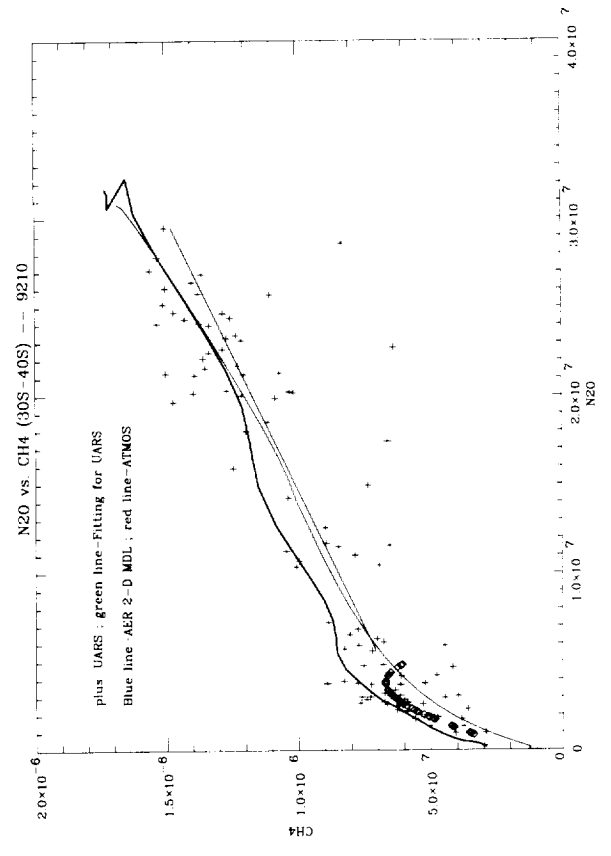
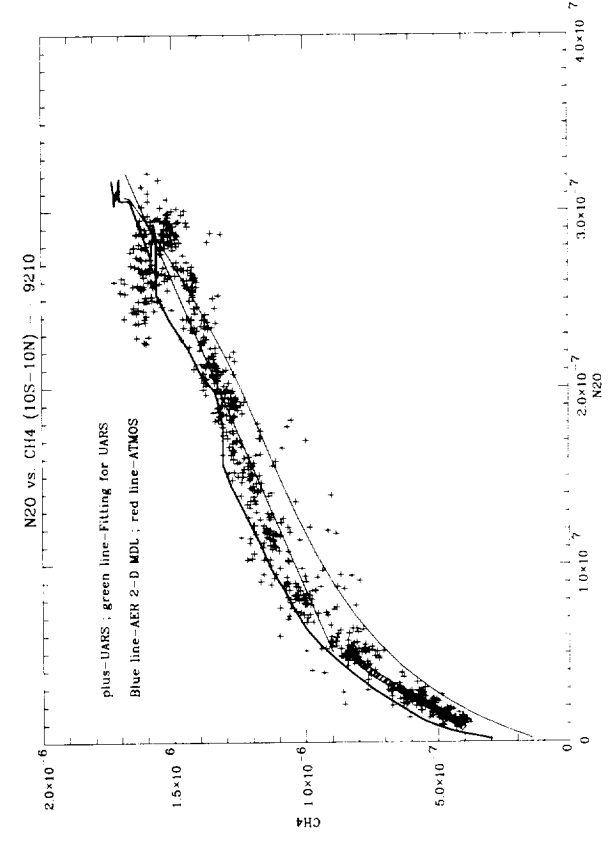
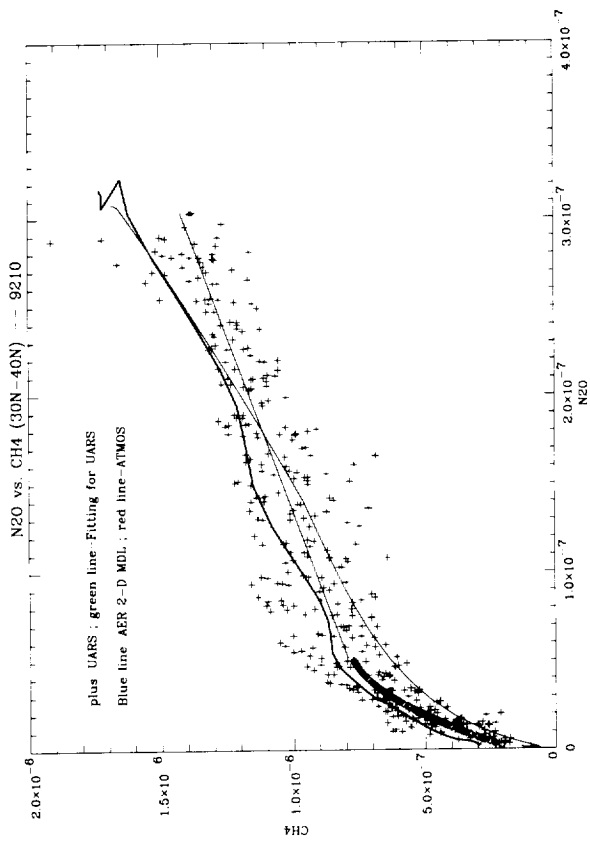


Figure II.6: N_2O vs CH_4 correlations from UARS measurements in October, at $30^\circ N-40^\circ N$ (a), $10^\circ N-10^\circ S$ (b), and $30^\circ S-40^\circ S$ (c) in comparison with ATMOS, and AER 2-D model output (using data at $38^\circ N$ (a), Equator (b) and $38^\circ S$ (c) respectively).

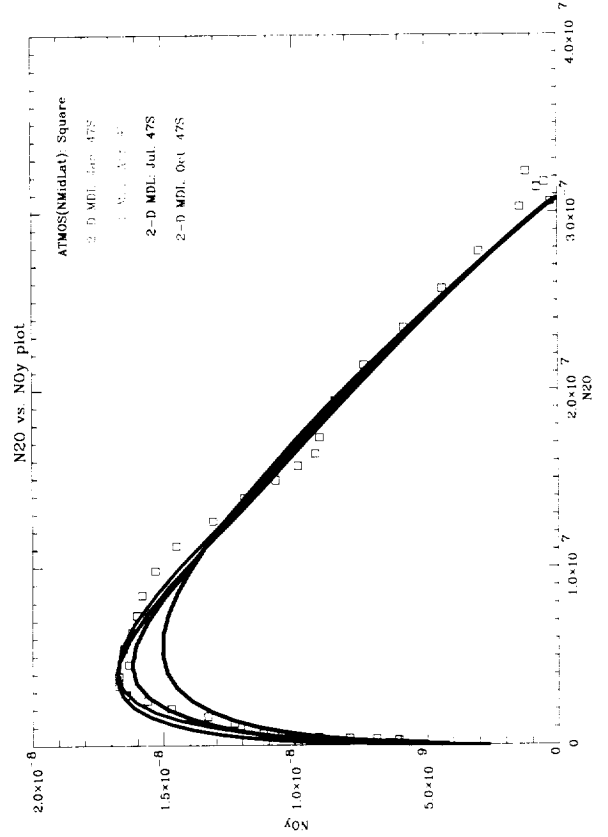
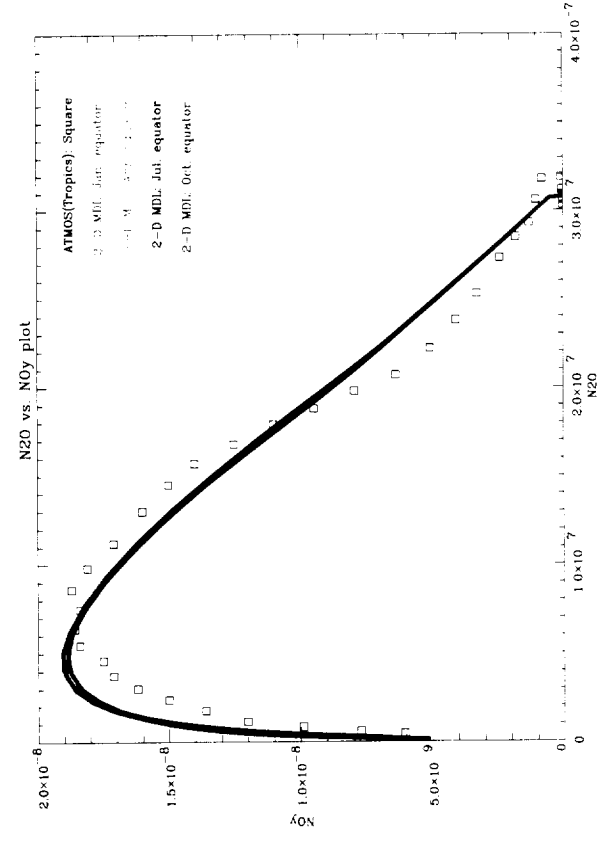
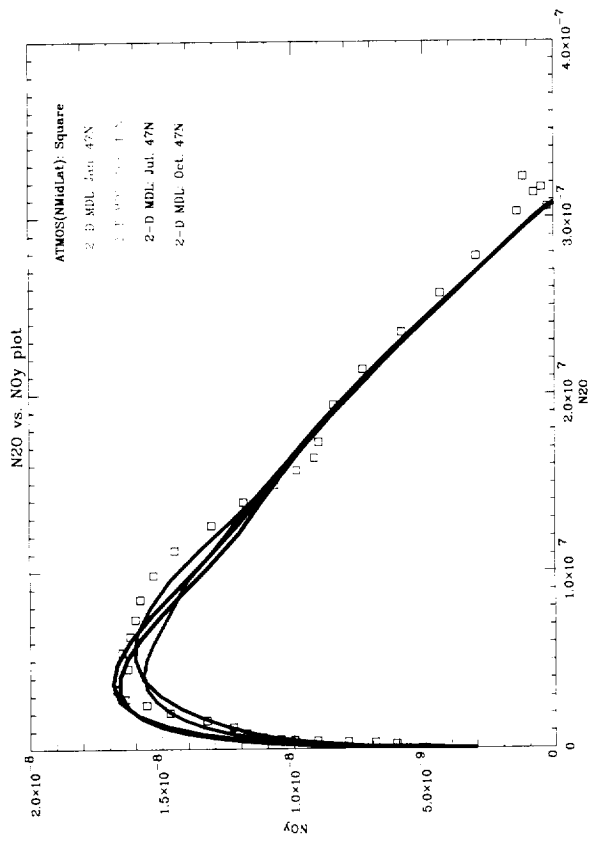


Figure II.7: N₂O vs. NO_y correlation from ATMOS and AER 2-D model in January, April, July and October at 47°N (a), equator (b), and 47S (c).

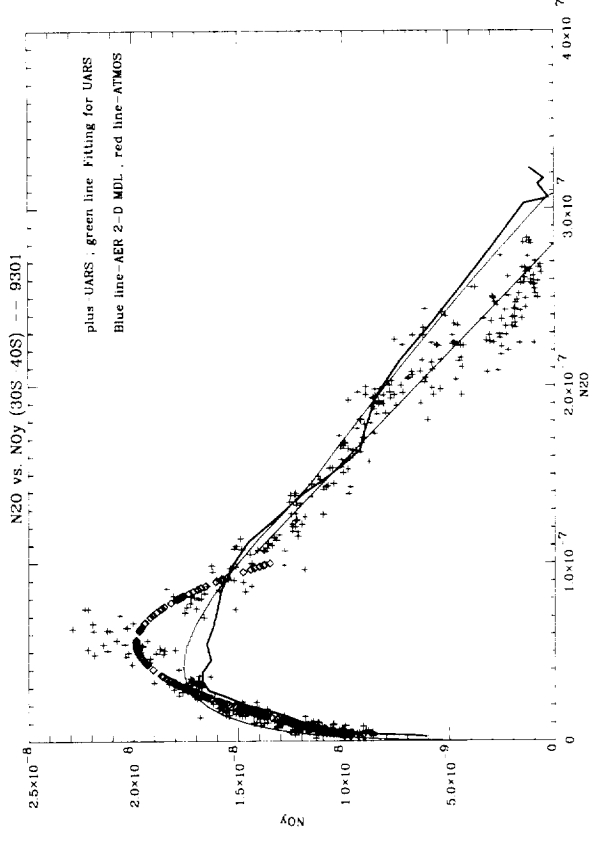
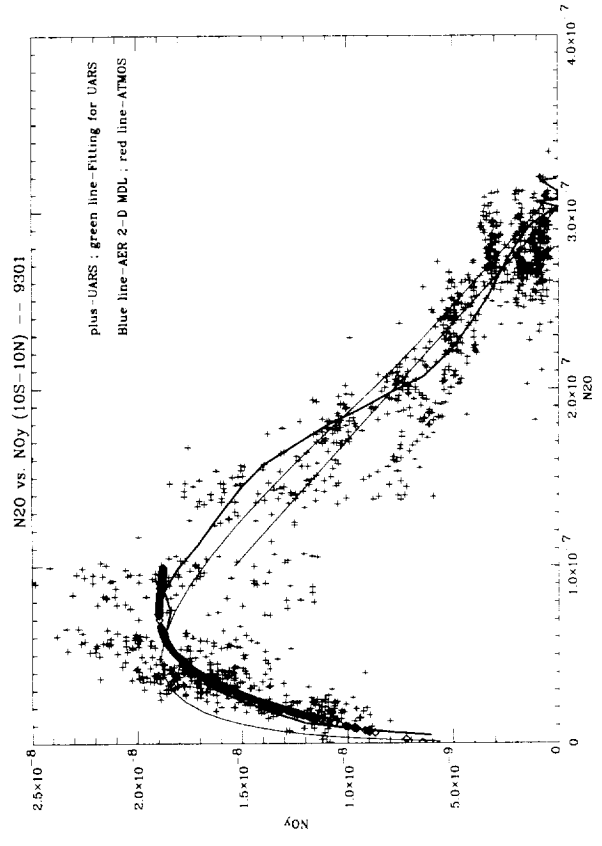
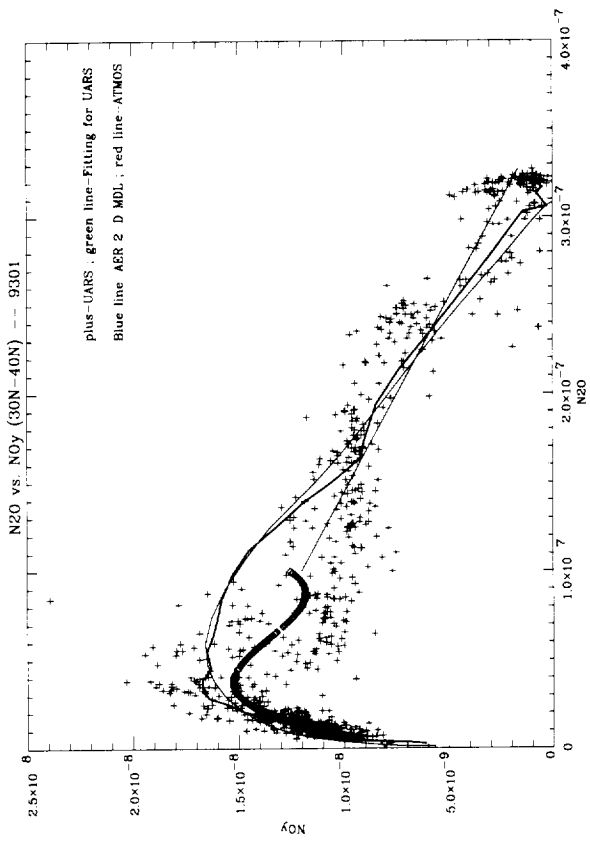


Figure II.8: N₂O vs. NO_y correlation from UARS measurements in January, at 30°N-40°N (a), 10°N-10°S (b), and 30°S-40°S (c) in comparison with ATMOS, and AER 2-D model output at 38°N (a), Equator (b) and 38°S (c) respectively.

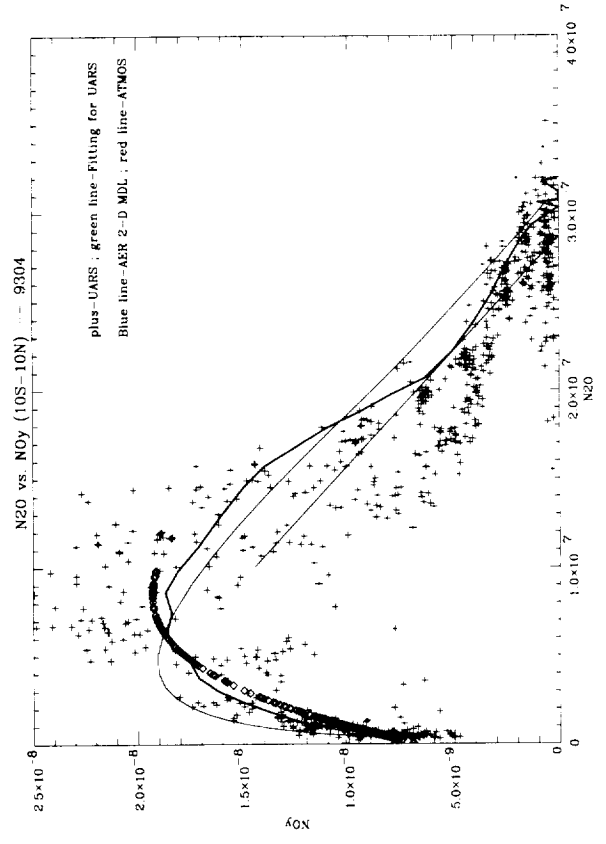
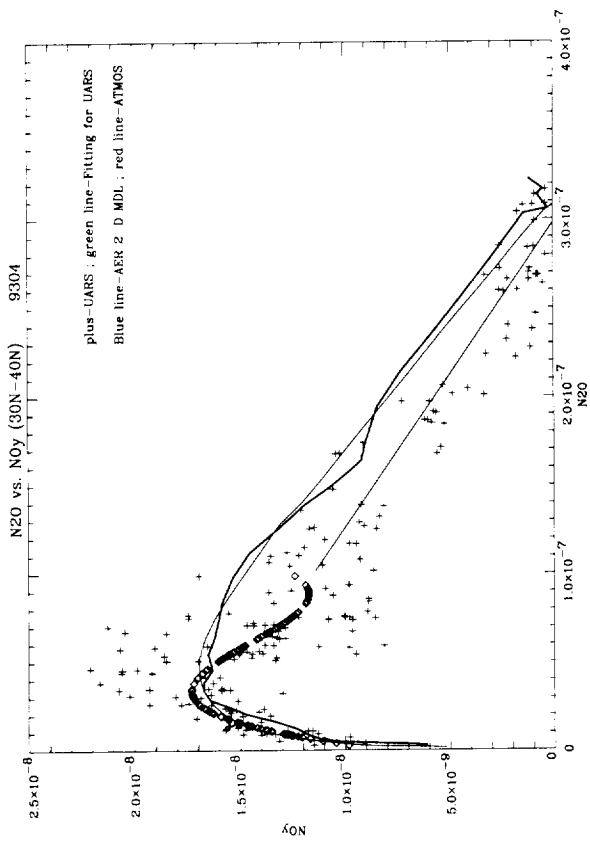


Figure II.9: N_2O vs. NO_y correlation from UARS measurements in April, at 30°N–40°N (a) and 10°N–10°S (b) in comparison with ATMOS, and AER 2-D model output at 38°N (a) and Equator (b) respectively.

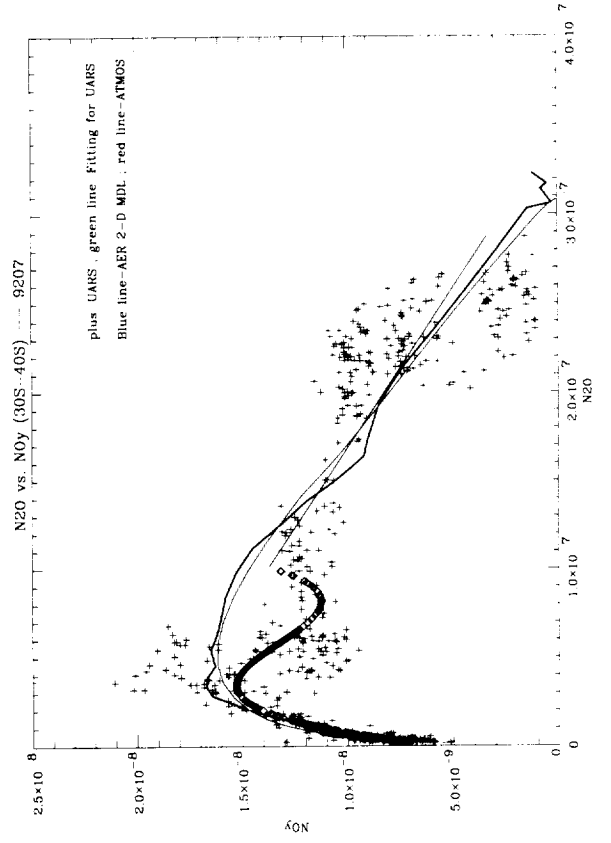
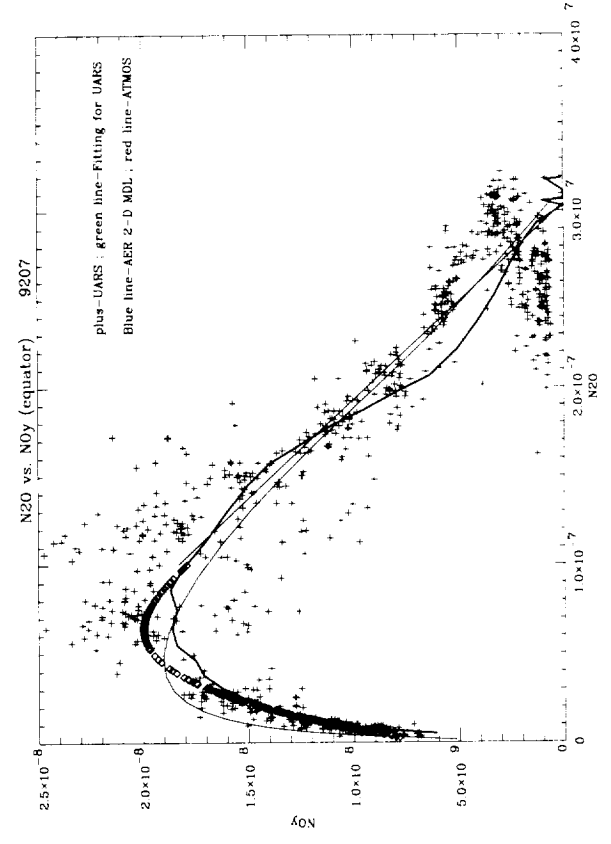
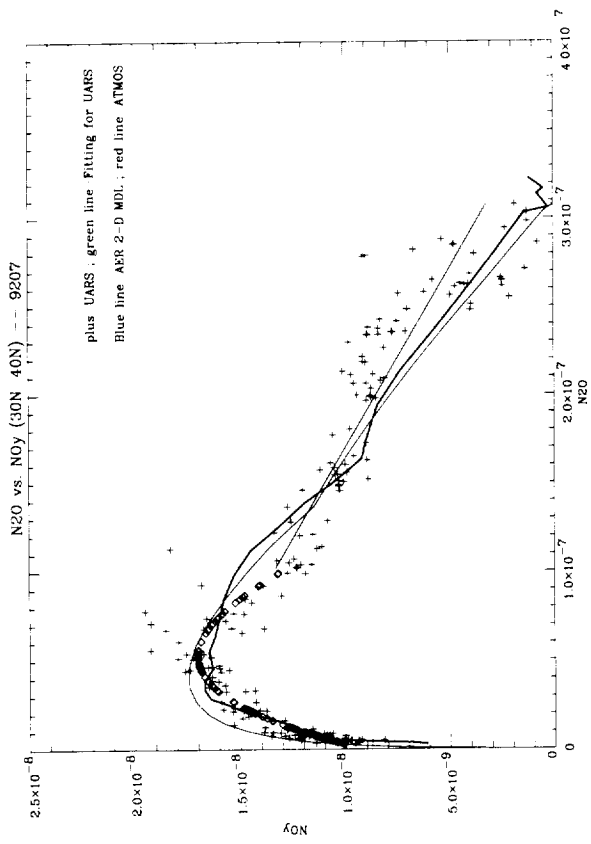


Figure II.10: N₂O vs. NO_y correlation from UARS measurements in July, at 30°N-40°N (a), 10°N-10°S (b), and 30°S-40°S (c) in comparison with ATMOS, and AER 2-D model output at 38°N (a), Equator (b) and 38°S (c) respectively.

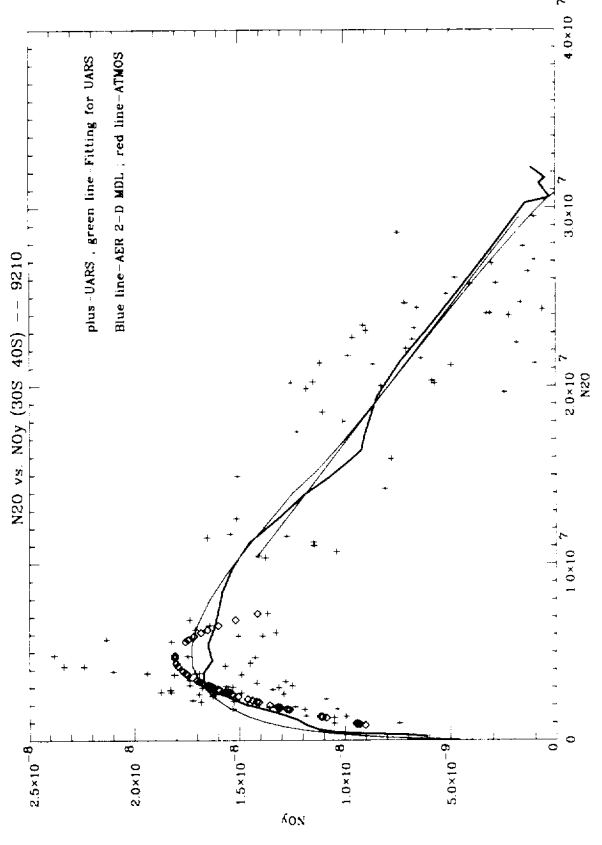
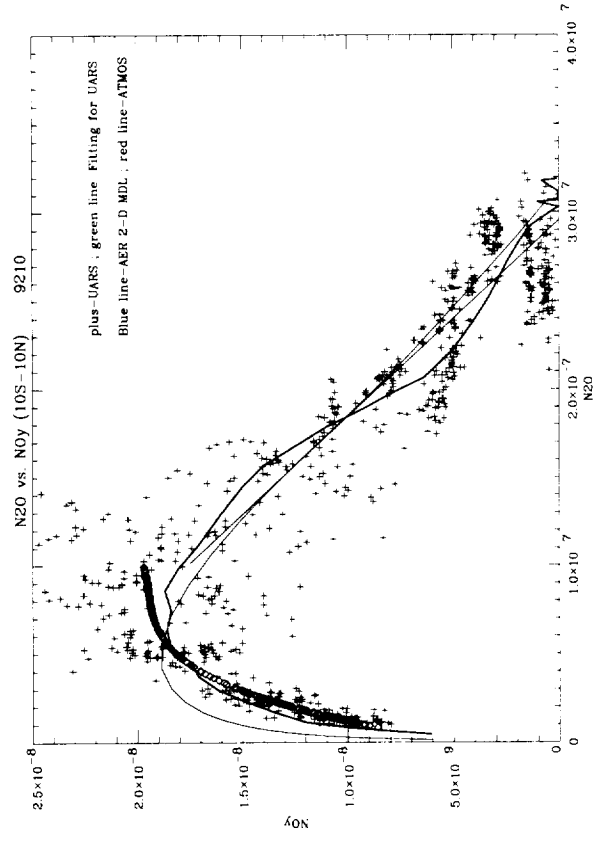
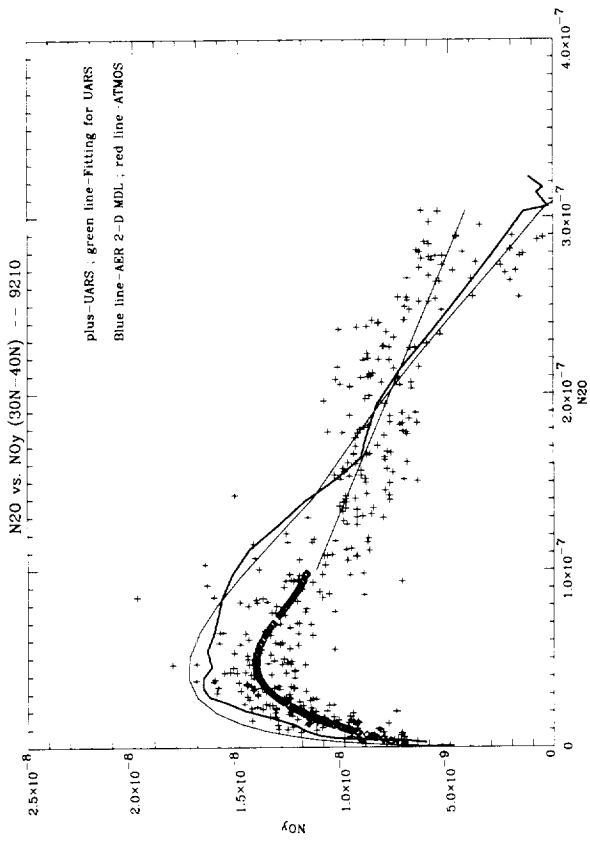


Figure II.11: N₂O vs. NO_y correlation from UARS measurements in October, at 30°N-40°N (a), 10°N-10°S (b), and 30°S-40°S (c) in comparison with ATMOS, and AER 2-D model output at 38°N (a), Equator (b) and 38°S (c) respectively.

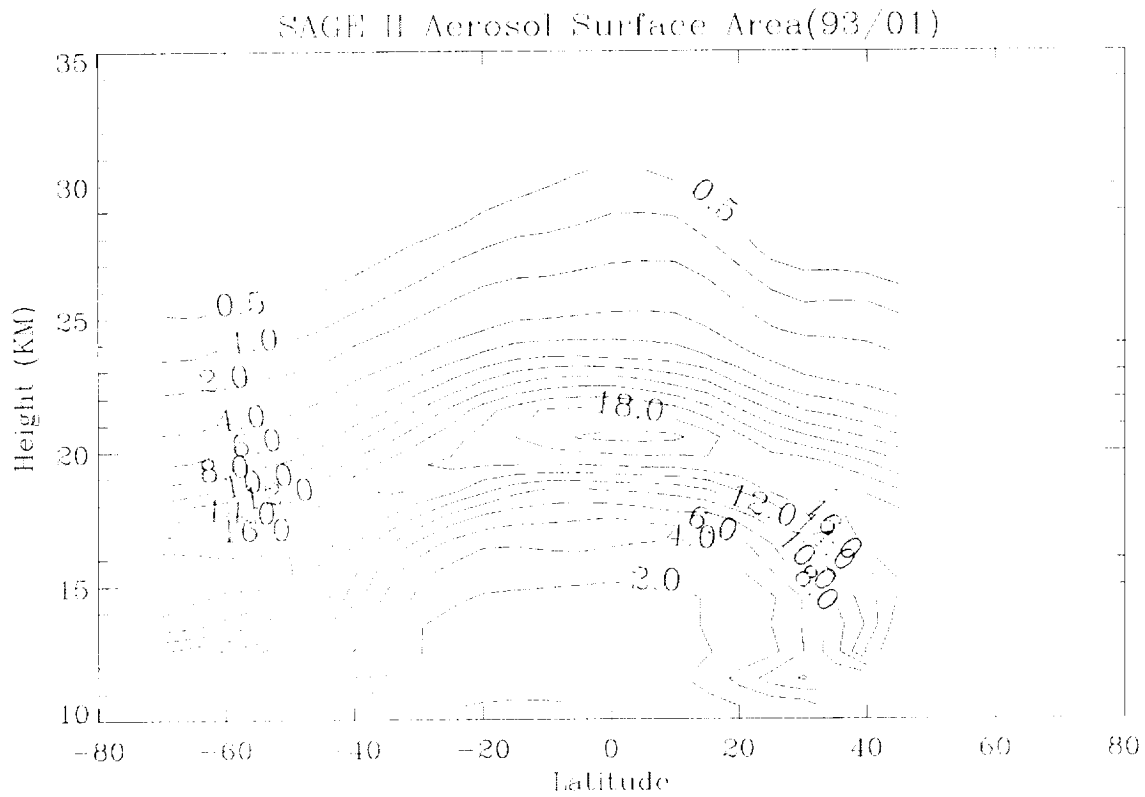
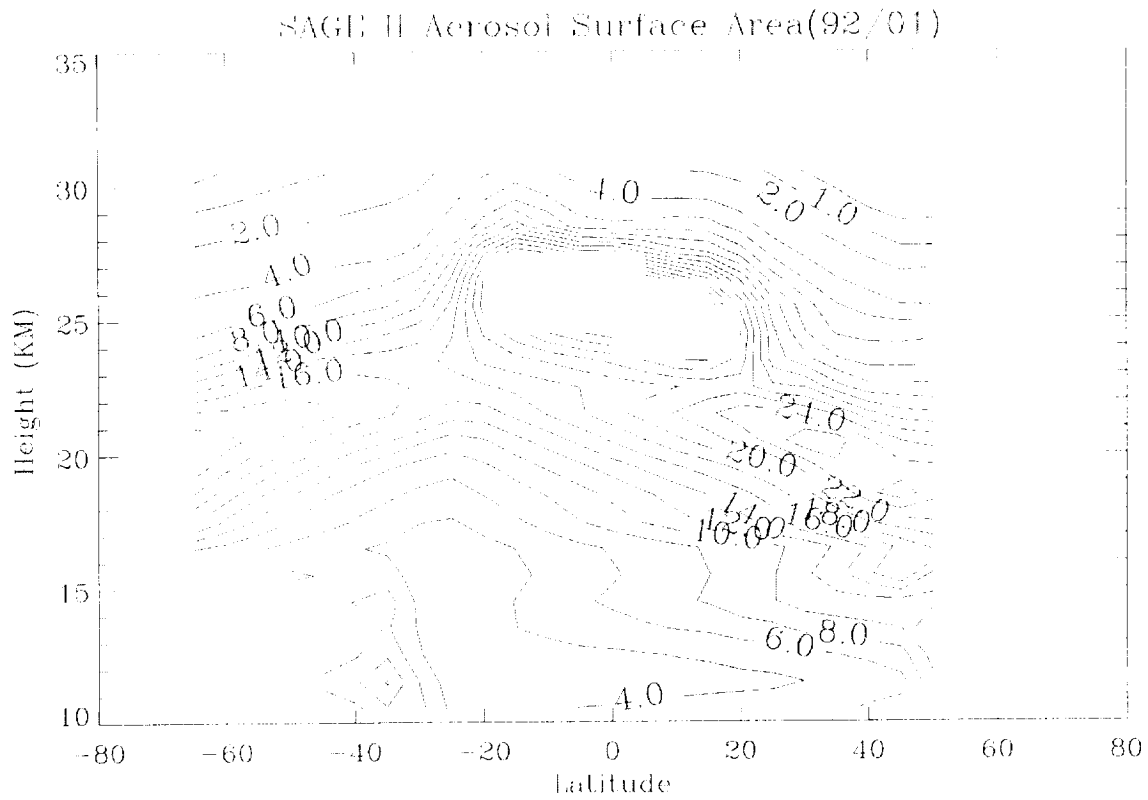


Figure III.1. Zonal mean aerosol SAD (in $\mu\text{m}^2/\text{cm}^3$) according to the SAGE II measurements in January 1992 (top) and January 1993 (bottom).

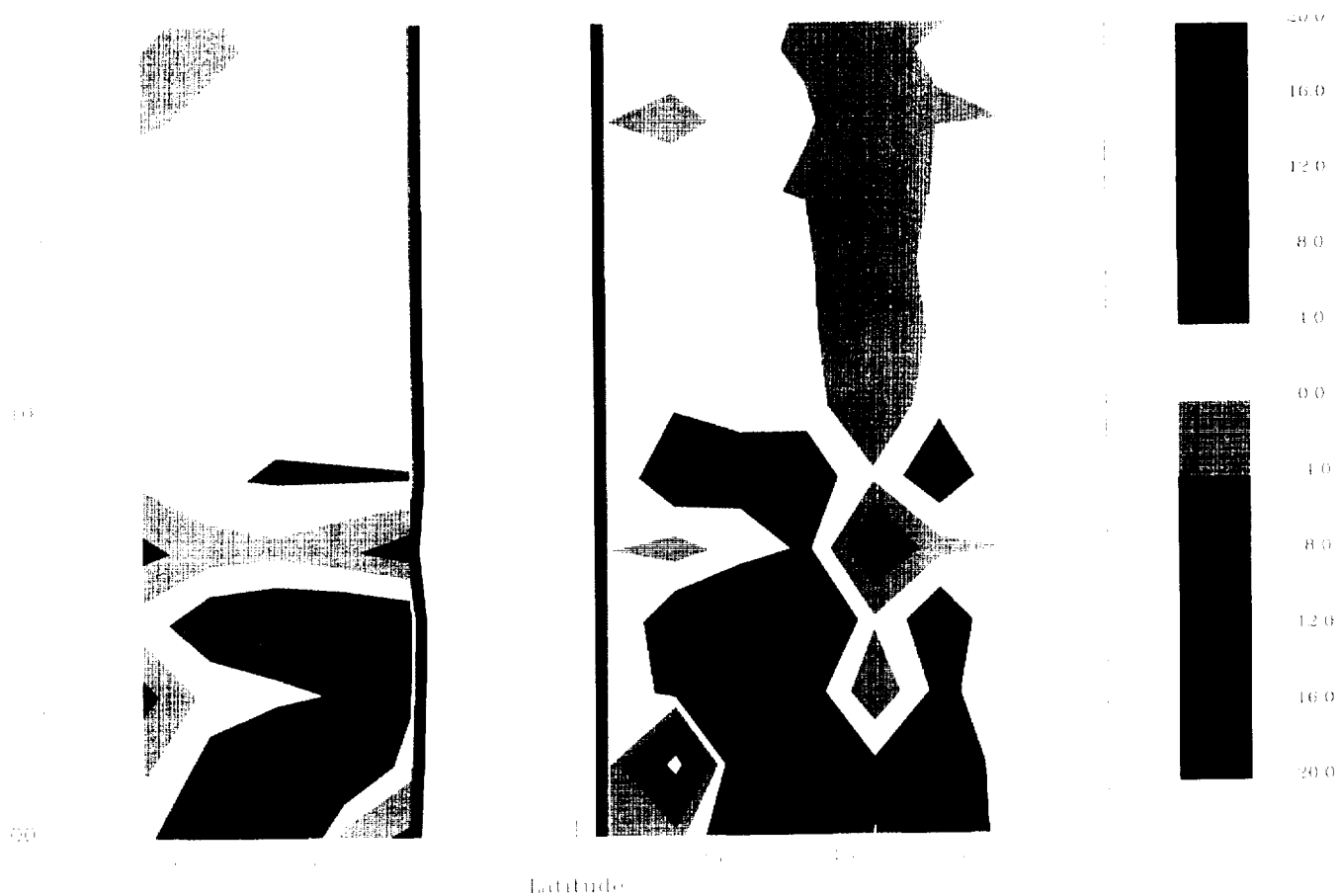


Figure III.2. Difference (in %) between model NO_x/NO_y calculated for monthly zonally averaged UARS data and for daily UARS data averaged over month and longitude. The CH_4 approach to initialize model runs has been used. A gap between 25° and 5°N is due to the geometry of HALOE measurements in February 1993 (sunrise and sunset measurements in the southern and northern hemisphere, respectively).

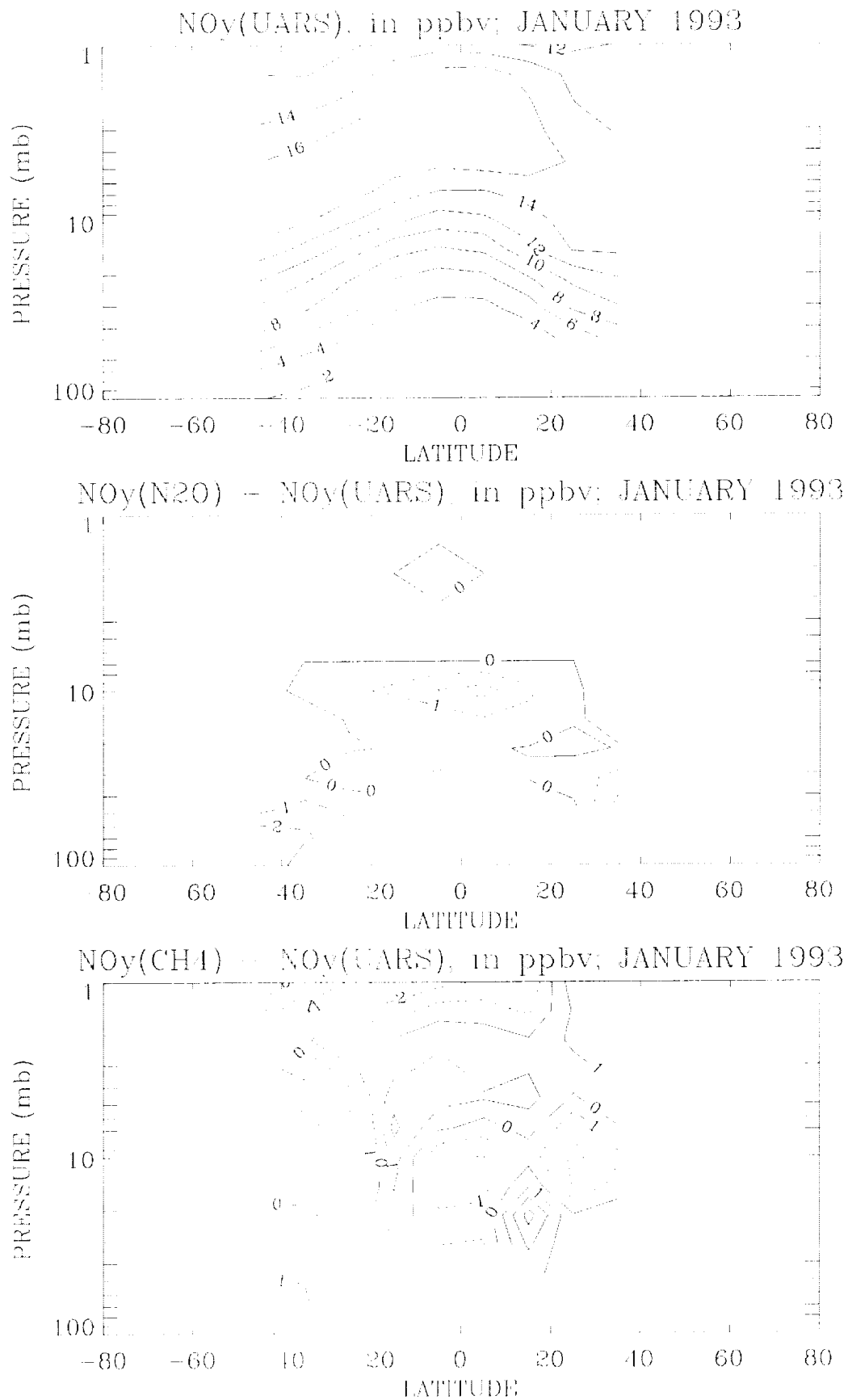


Figure III.3. Distribution of NO_y (in ppbv, top panel) in January 1993 using the UARS initialization (see Table III.2). The middle and bottom panels show the difference between NO_yUARS and NO_y as inferred from the correlations with CLAES zonal monthly averaged <N₂O_c and HALOE <CH₄>, respectively (see text for details).

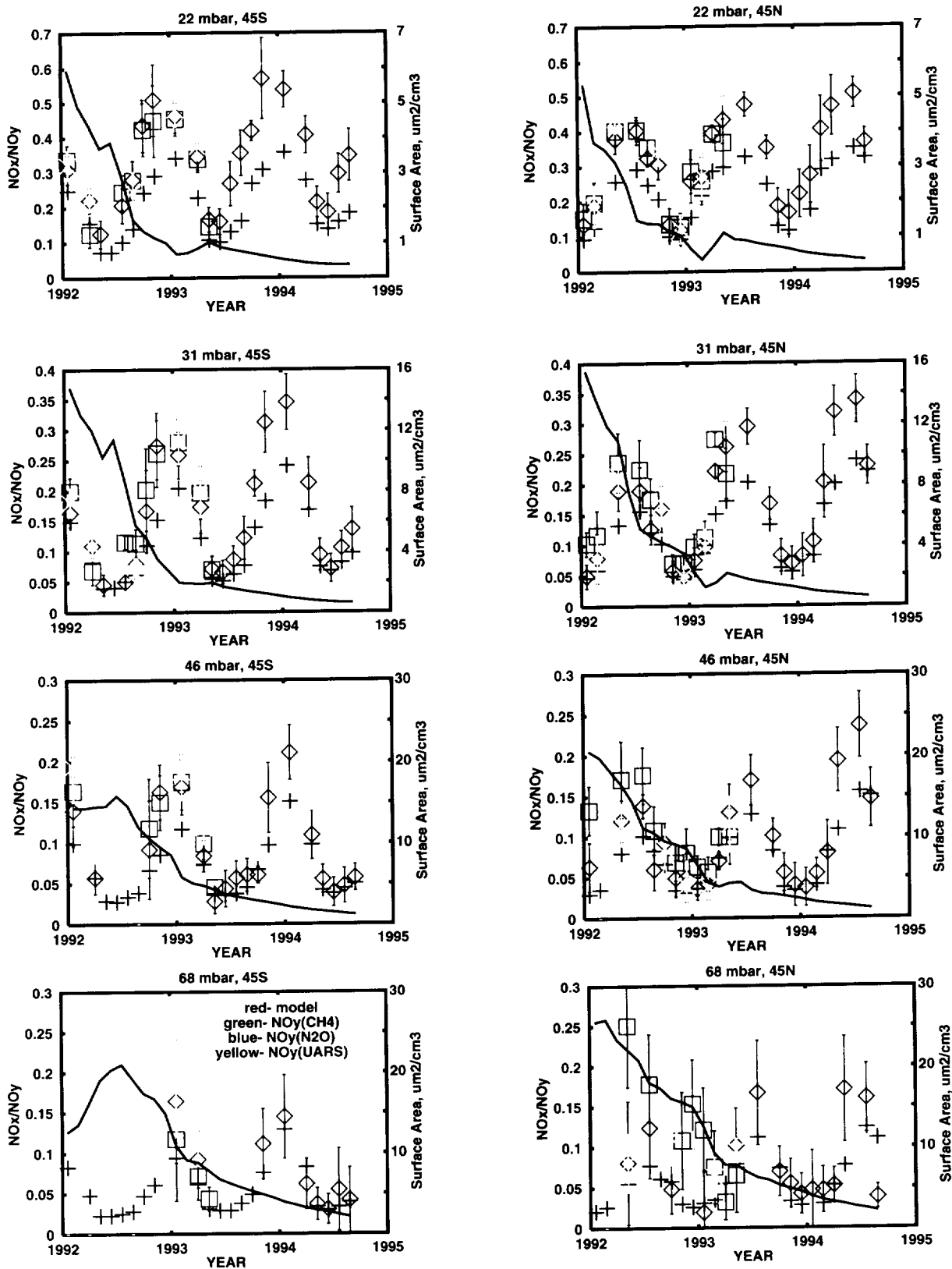


Figure III.4. Temporal evolution of the sunset NO_x/NO_y ratio from January 1992 to September 1994 at 45°S (left column) and 45°N (right column) at the 68, 46, 32, and 22 mbar levels. Green, yellow, and blue symbols with errorbars correspond to the UARS data with NO_y according to the CH_4 , UARS, and N_2O initializations, respectively; red crosses to box model calculations. The N_2O and UARS approaches can provide NO_y data only until May 1993 because of the CLAES lifetime. The black lines show behavior of aerosol surface area density (right vertical axis, in $\mu\text{m}^2/\text{cm}^3$).

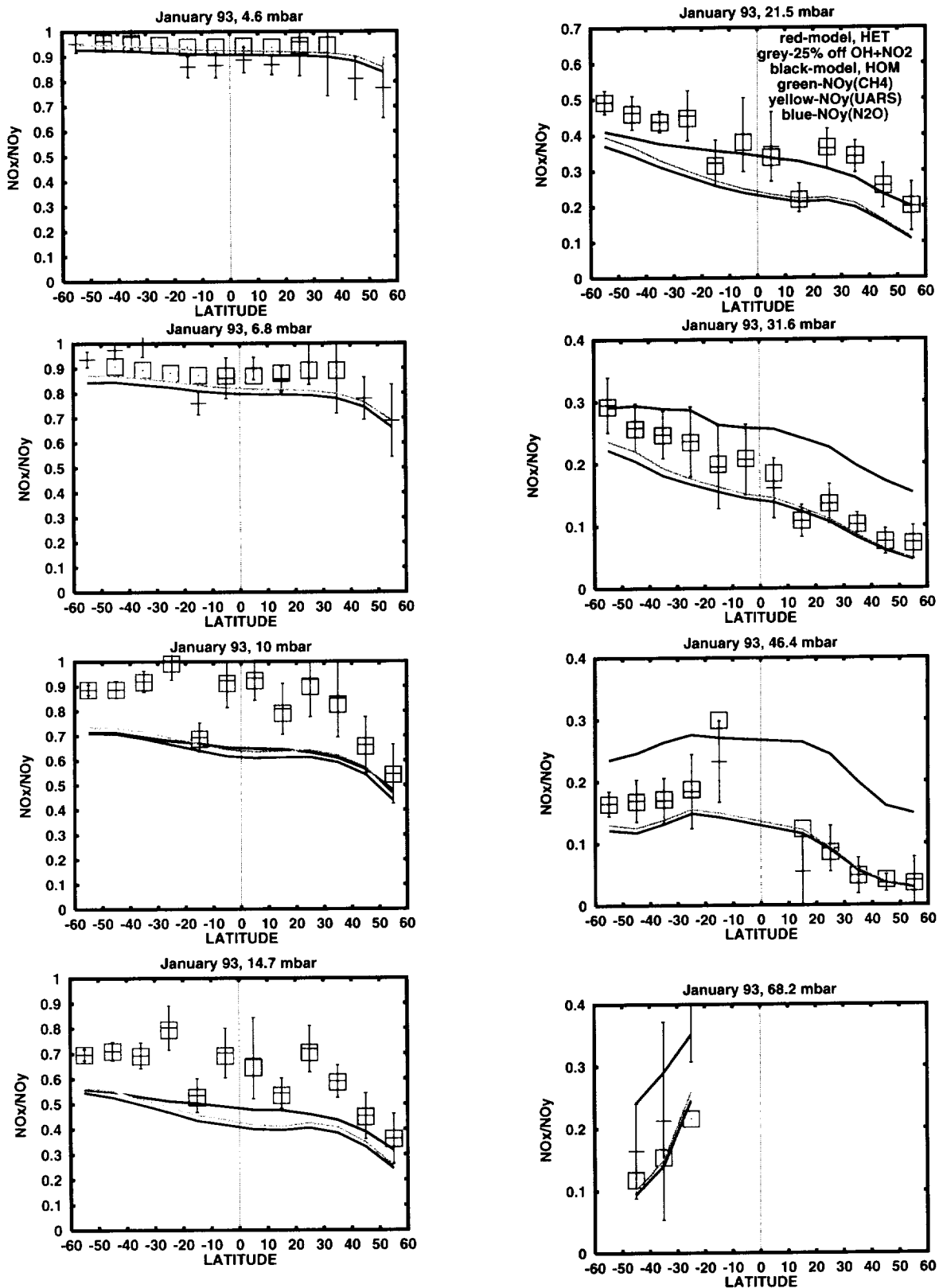


Figure III.5. Latitudinal dependence of the sunset NO_x/NO_y ratio in January 1993 at the levels shown between 68.2 and 4.6 mbar. Model results with and without heterogeneous reactions on sulfate aerosol are shown by red and black lines, respectively. Model results with heterogeneous chemistry and with reduced by 25% reaction rate of $\text{OH} + \text{NO}_2 + \text{M} \rightarrow \text{HNO}_3 + \text{M}$ are shown by grey lines. At the 4.6 and 6.8 mbar levels, the model NO_x/NO_y ratio is the same for calculations with and without heterogeneous reactions. The UARS values are shown by symbols for the three methods of NO_y initialization: yellow for $\text{NO}_y(\text{UARS})$, green for $\text{NO}_y(\text{CH}_4)$, and blue for $\text{NO}_y(\text{N}_2\text{O})$.

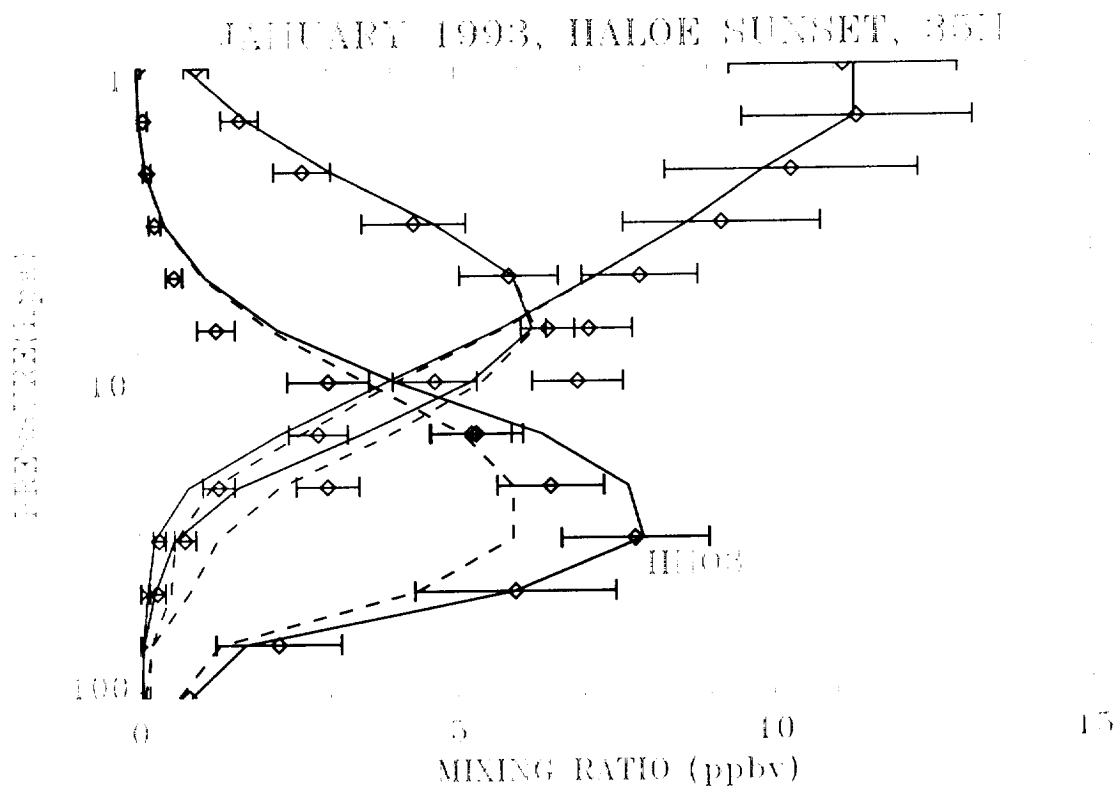
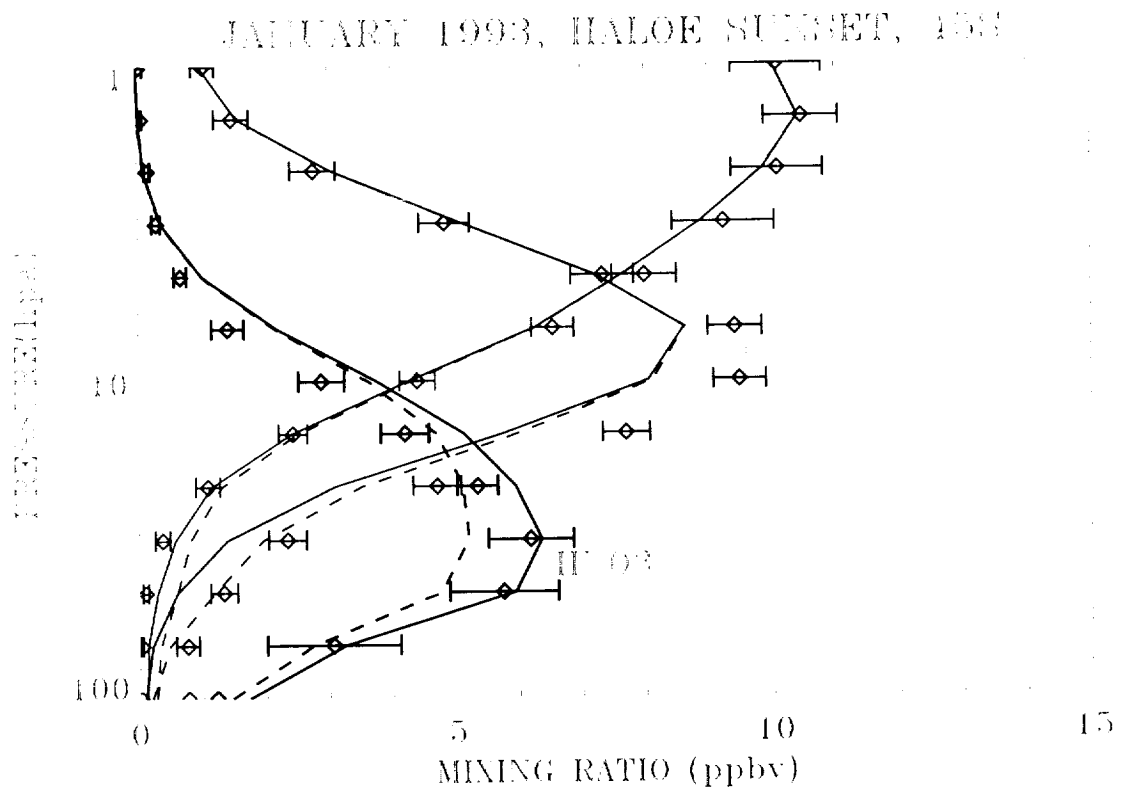


Figure III.6. Vertical profiles of NO (blue), NO₂ (cyan), and HNO₃ (red) in January 1993 at 45°S (top panel) and 35°N (bottom panel) at sunset. UARS data are shown by symbols with errorbars, model results are shown by solid (with heterogeneous reactions) and dashed (without heterogeneous reactions) lines according to the UARS initialization.

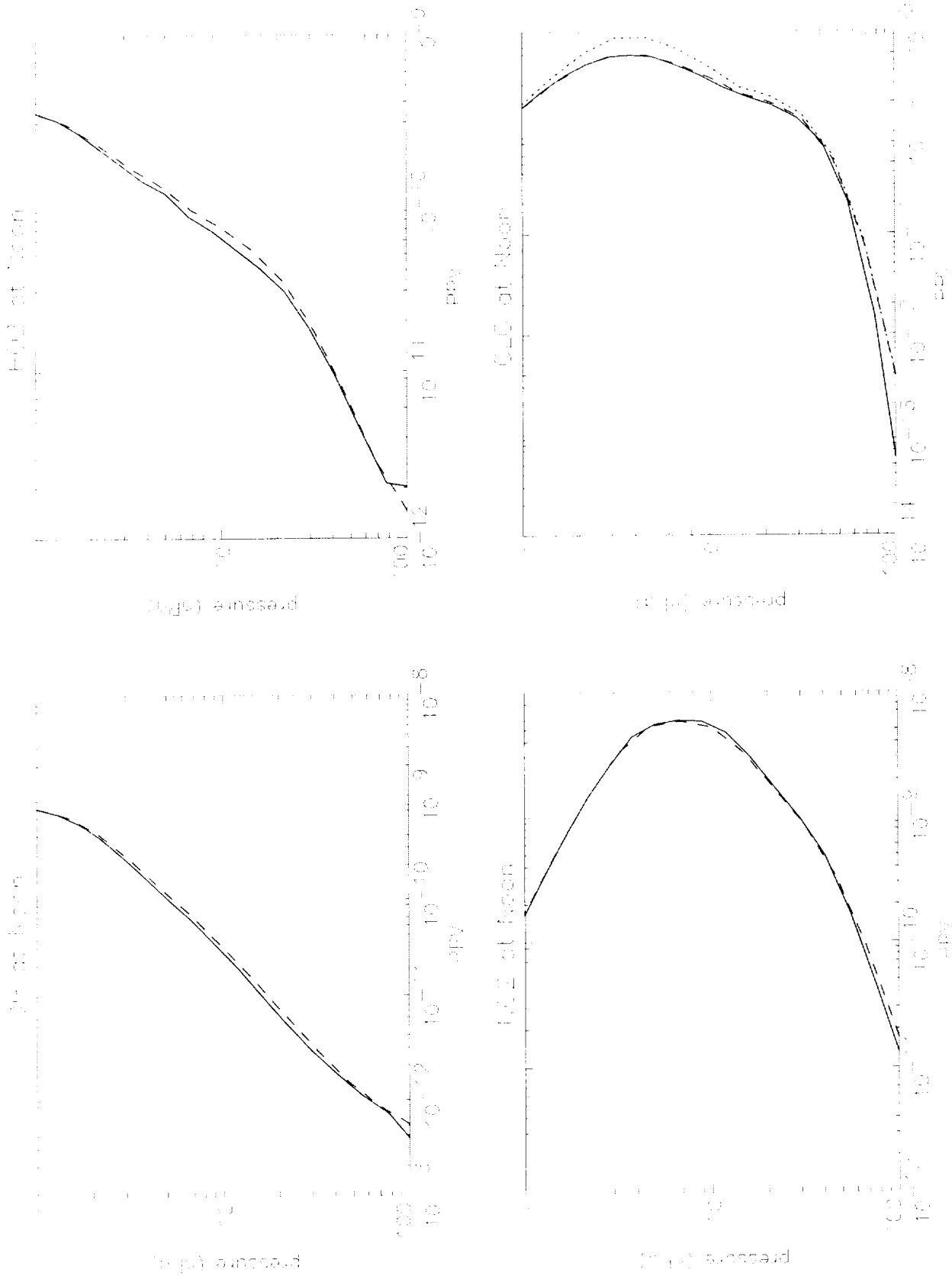


Figure IV.1: The profiles of OH, HO₂, ClO and NO₂ at noon time from box model (dash line) and Osterman's output rescaled by the observations of *in-situ* balloons (solid line) (Osterman et al. 1997).

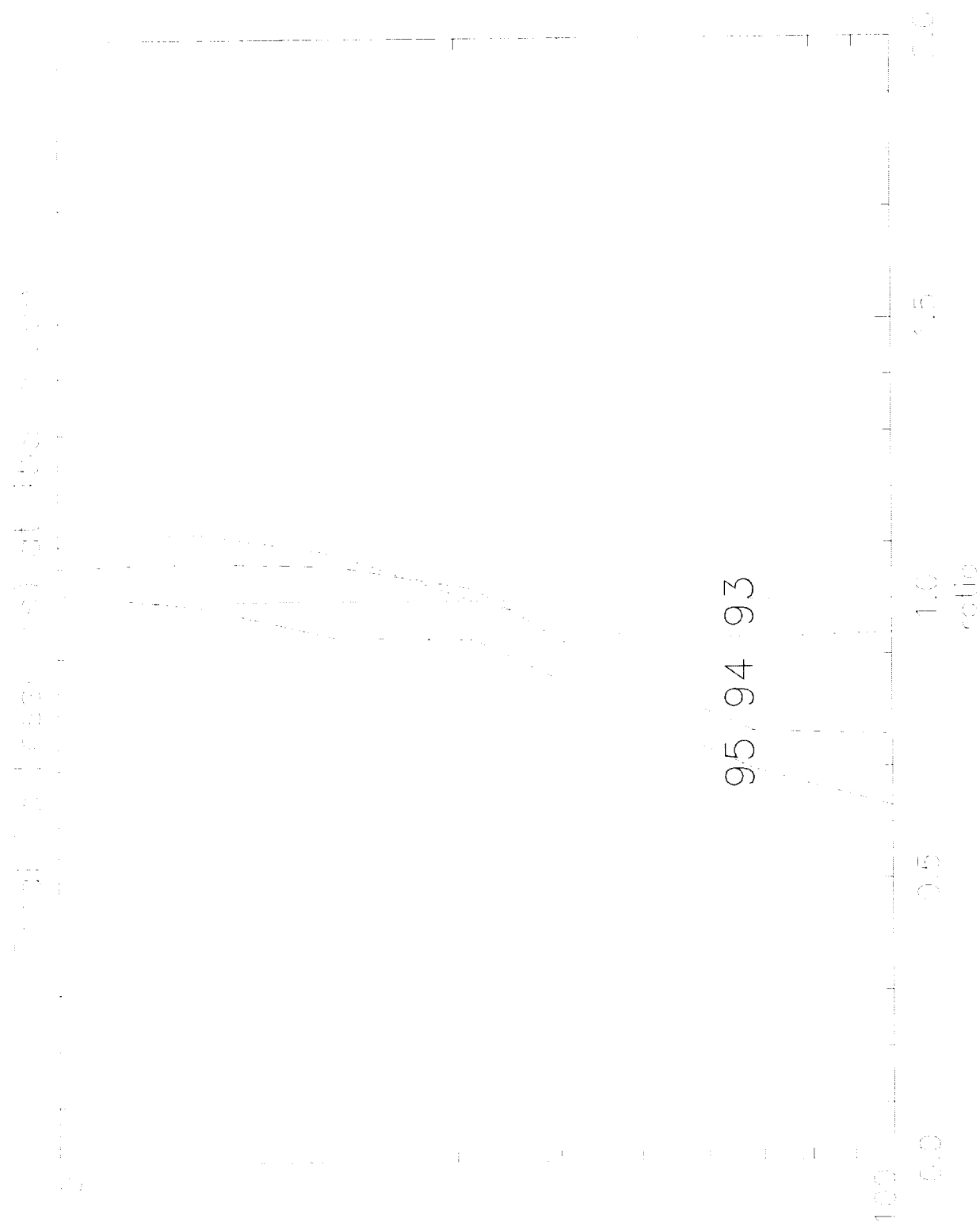


Figure IV.2: The total ozone loss calculated by box model at 45°S in January of 1993, 1994, 1995 vs. January 1992. The solid, dotted, dashed, and dotted-dashed lines are January 1992, 1993, 1994, 1995 data respectively. Ozone loss are loss frequency is shown relative to the January 1992 conditions.

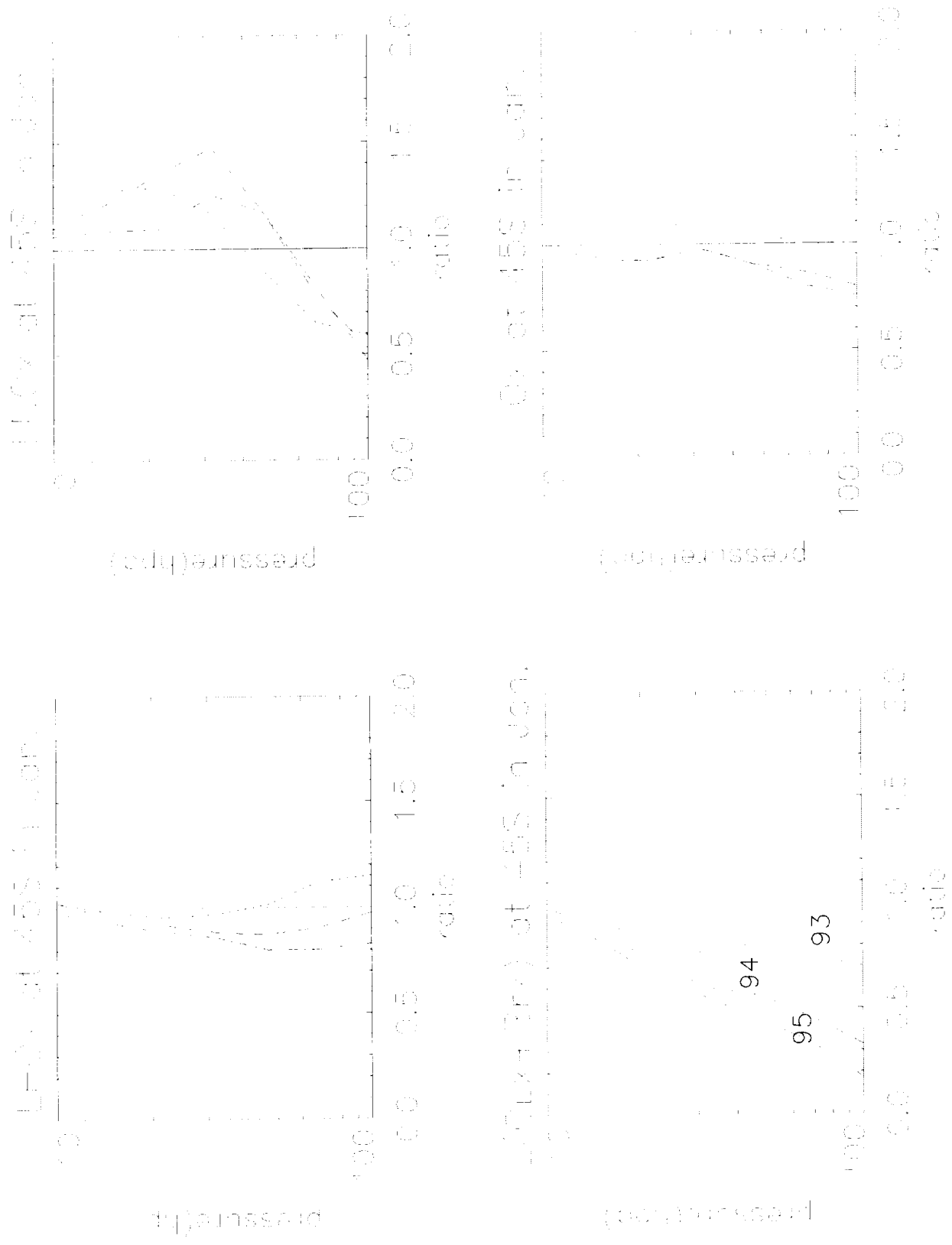


Figure IV.3a: The ozone loss rates contributed from hydrogen (HO_x), nitrogen (NO_x), halogen (Cl_x+Br_x) and odd oxygen (O_x) cycles at 45°S in January of 1993, 1994, 1995 vs. January 1992. The solid, dotted, dashed, and dotted-dashed lines are January 1992, 1993, 1994, 1995 data, respectively. Ozone loss frequency is shown relative to January 1992 conditions.

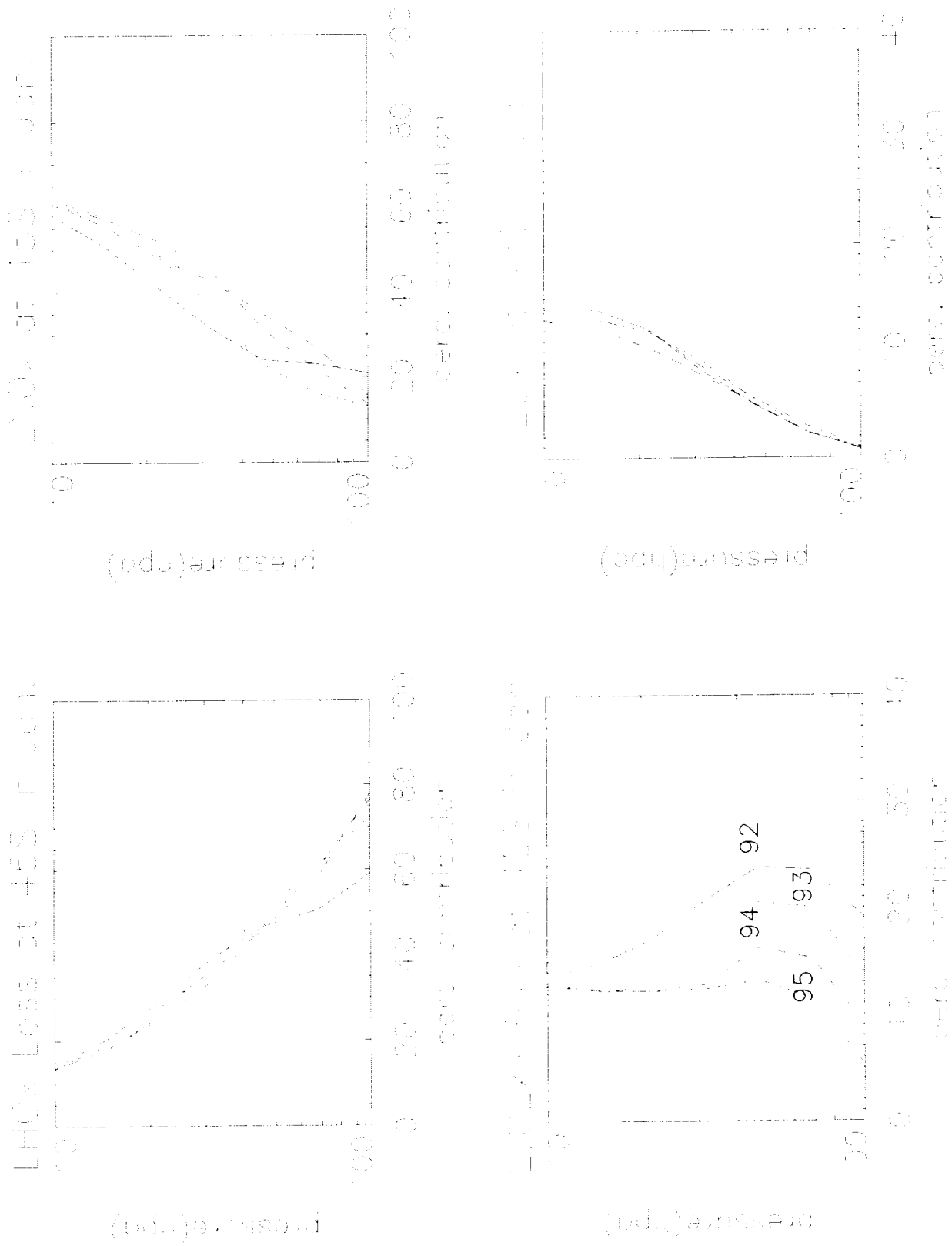


Figure IV.3b: The relative contributions to ozone loss rates from hydrogen (HO_x), nitrogen (NO_x), halogen (Cl_x+Br_x) and odd oxygen (O_3) cycles at 45°S in January of 1993, 1994, 1995 vs. January 1992. The solid, dotted, dashed, and dotted-dashed lines are January 1992, 1993, 1994, 1995 data, respectively. Ozone loss frequency is shown relative to January 1992 conditions.

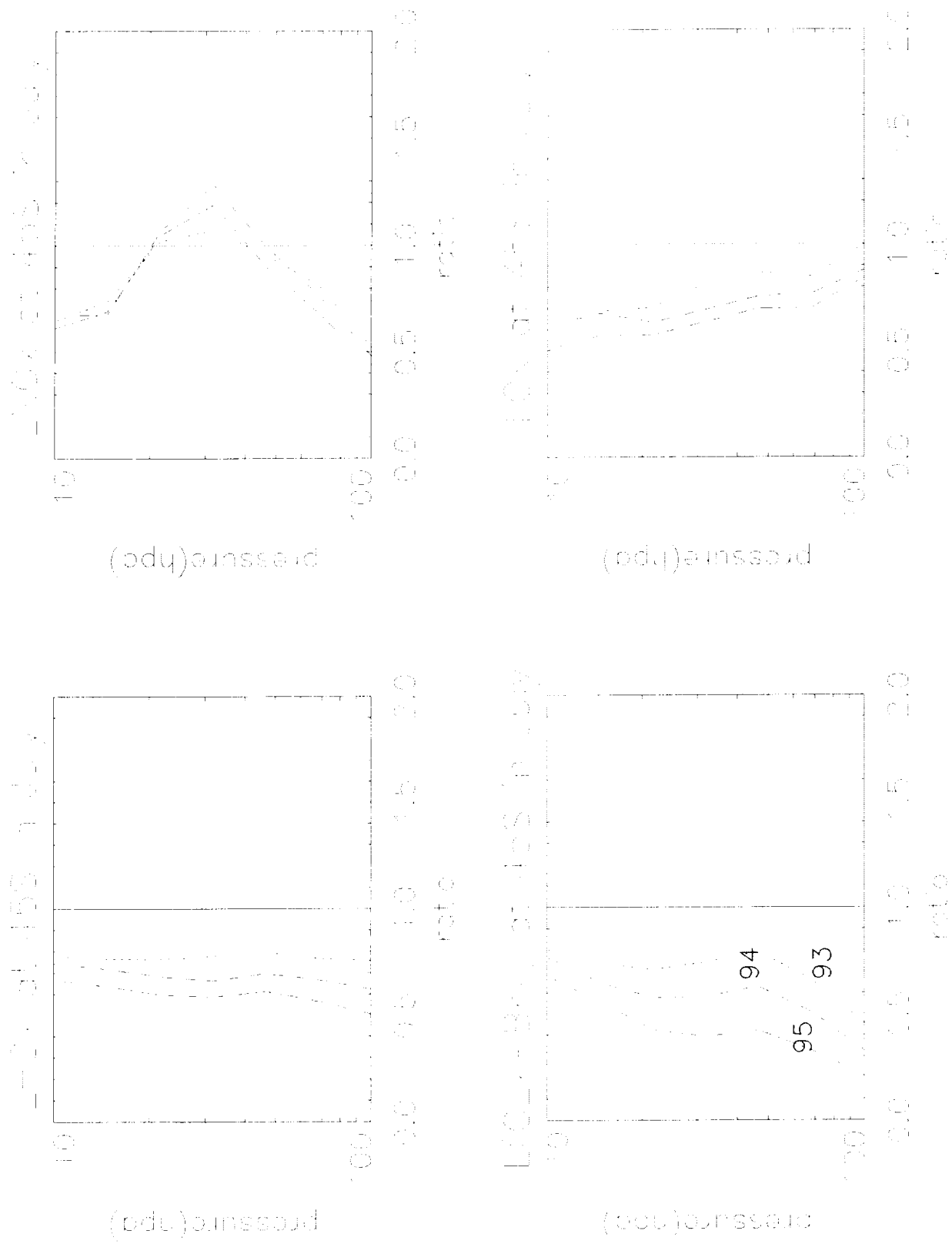


Figure IV.4a: The ozone loss rates contributed from hydrogen (HO_x), nitrogen (NO_x), halogen ($\text{Cl}_x + \text{Br}_x$) and odd oxygen (O_x) cycles at 45°S in July of 1993, 1994, 1995 vs. July 1992. The solid, dotted, dashed, and dotted-dashed lines are July 1992, 1993, 1994, 1995 data respectively. Ozone loss frequency is shown relative to July 1992.

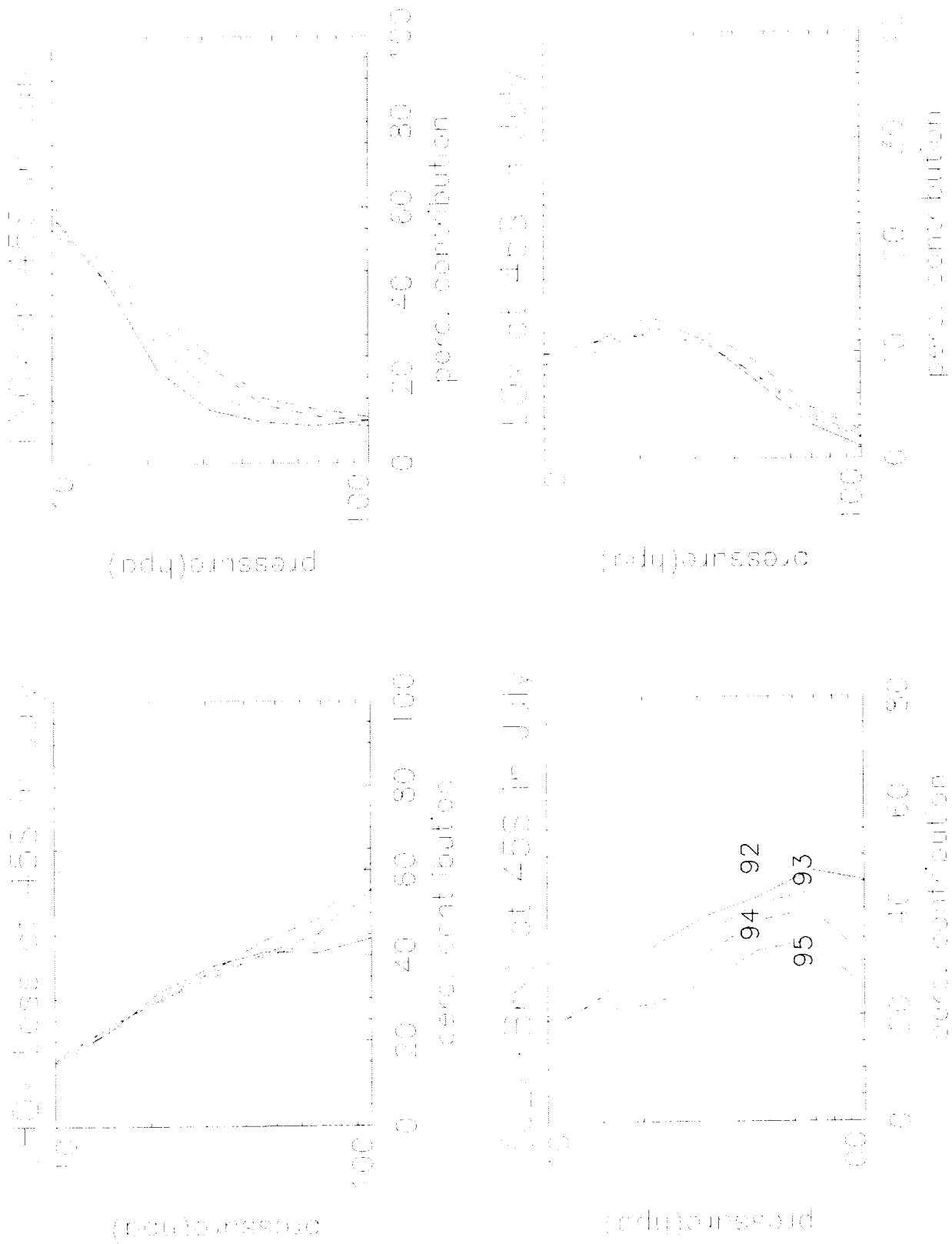


Figure IV.4b: The relative contributions to ozone loss rates contributed from hydrogen (HO_x), nitrogen (NO_x), halogen (Cl_x+Br_x) and odd oxygen (O_x) cycles at 45°S in July of 1993, 1994, 1995 vs. July 1992. The solid, dotted, dashed, and dot-dashed lines are July 1992, 1993, 1994, 1995 data respectively.

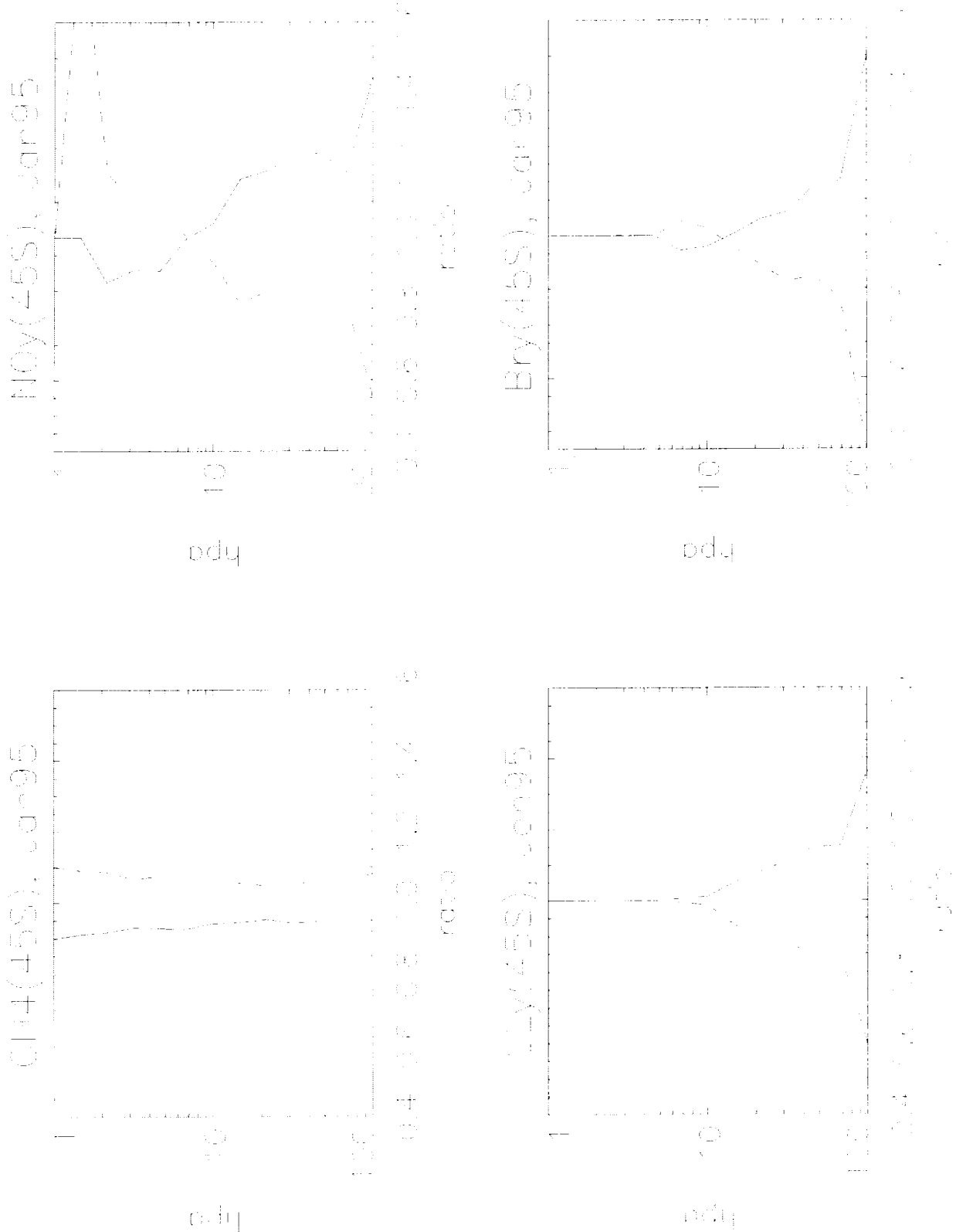


Figure IV.5a: The effects of -1σ change of CH₄ profile on NO_y, Cl_y and Br_y values. The solid line represents -1σ change. The dashed line represents $+1\sigma$ change.

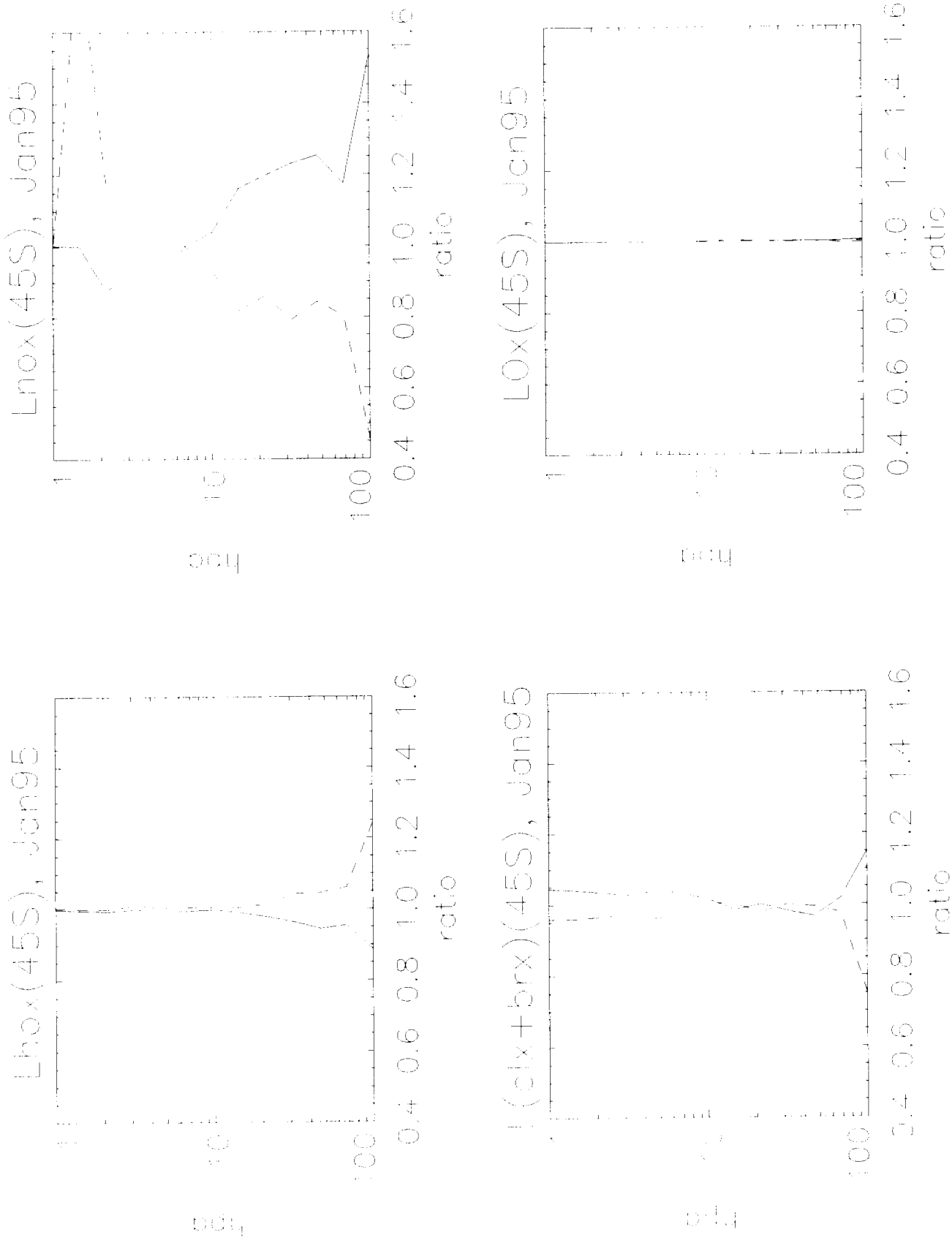


Figure IV.5b: The effects of 1σ change of CH_4 profile on ozone loss frequency by each catalytic cycle. The solid line represents $+1\sigma$ change. The dashed line represents -1σ change.

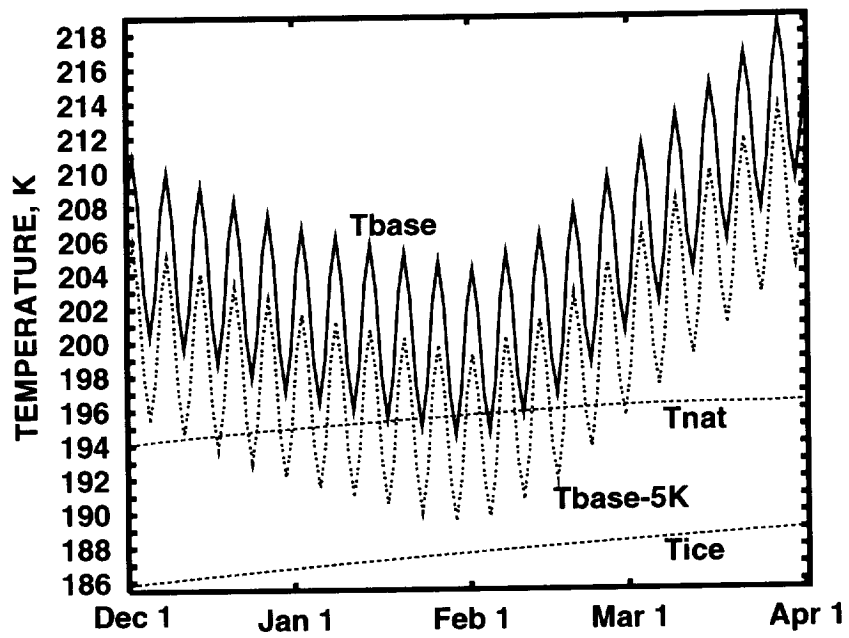


Figure V.1. The temperature history adopted for the model runs.

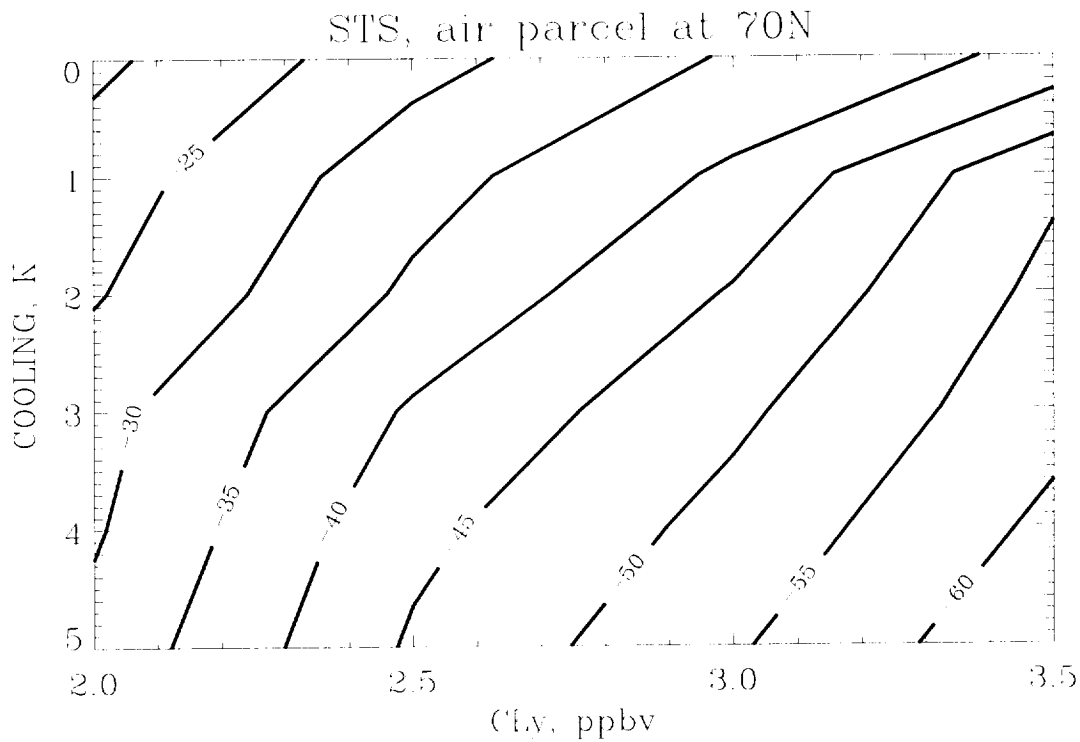
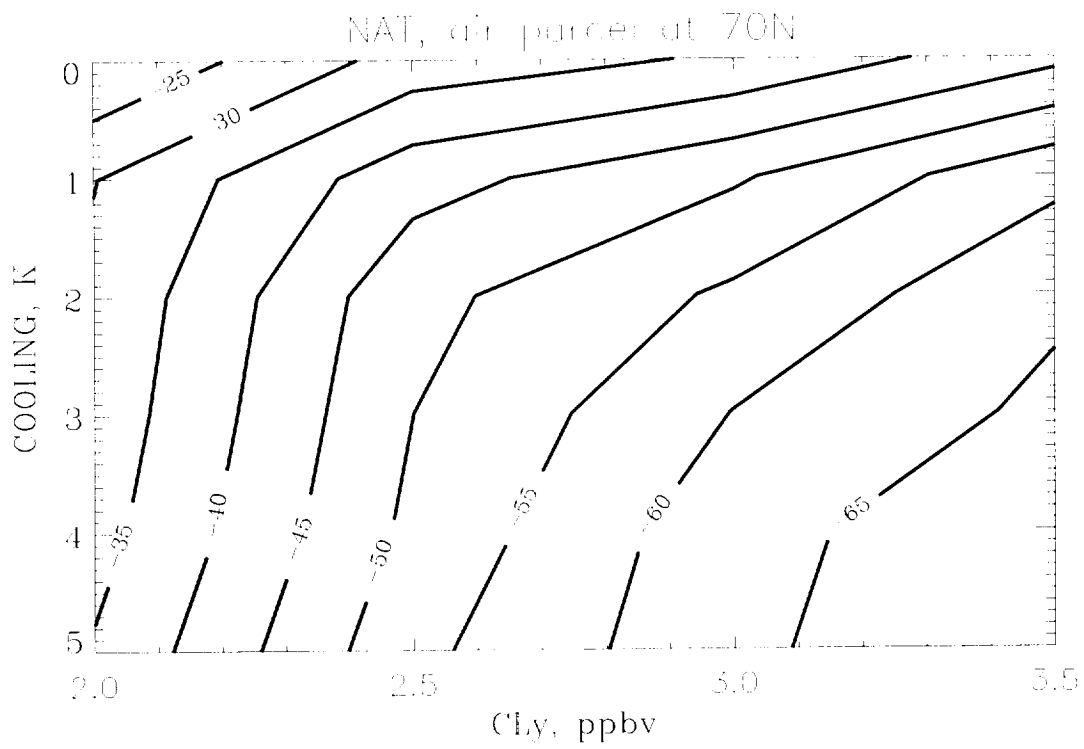


Figure V.2 Isolines of ozone change in the air parcel on April 1 (in% of 3.6 ppmv) as a function of chlorine loading and stratospheric cooling at 20 km for the NAT (top) and STS (bottom) schemes. Zero cooling corresponds to T_{base} and 5K cooling to $T_{\text{base}}-5\text{K}$ in Figure V.1.

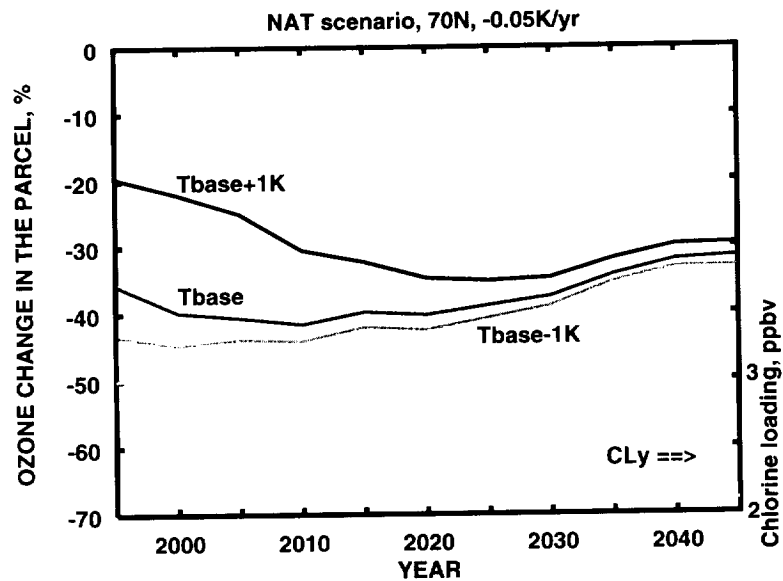
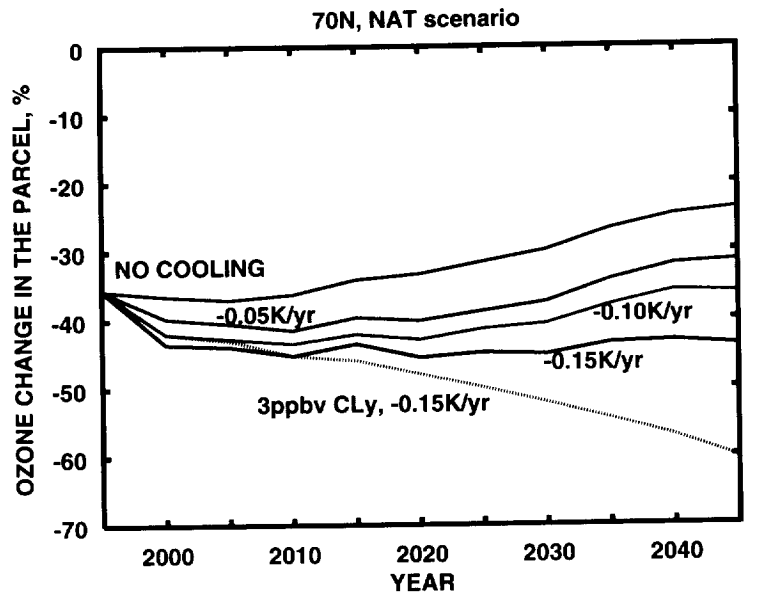


Figure V.3. Ozone depletion as function of year for the projected chlorine loading and different temperature trends. Ozone behavior for the different choice of T_{base} and adopted Cl_y at 32hPa are shown in the bottom panel for the temperature trend of $-0.05K/yr$.

Asynoptic map of CLAES N₂O at 800K (09/09/92-09/10/92)

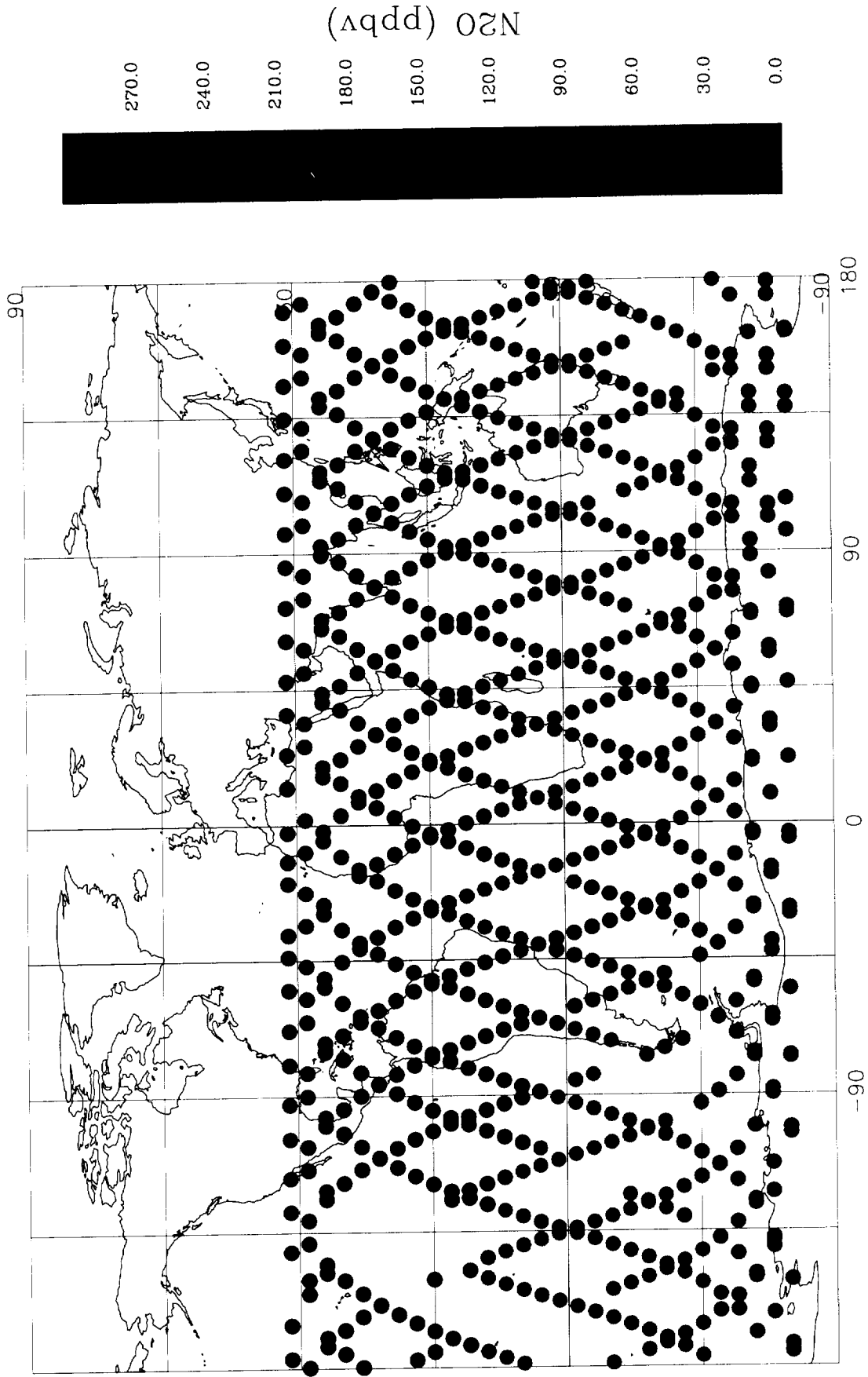


Figure VI.1a: Asynoptic map of CLAES N₂O at 800K isentropic surface measured during 00UT, 9/9/92 to 00UT, 9/10/92.

Synoptic map of CLAES N₂O at 800K (09/09/92 at 12UT) --AER

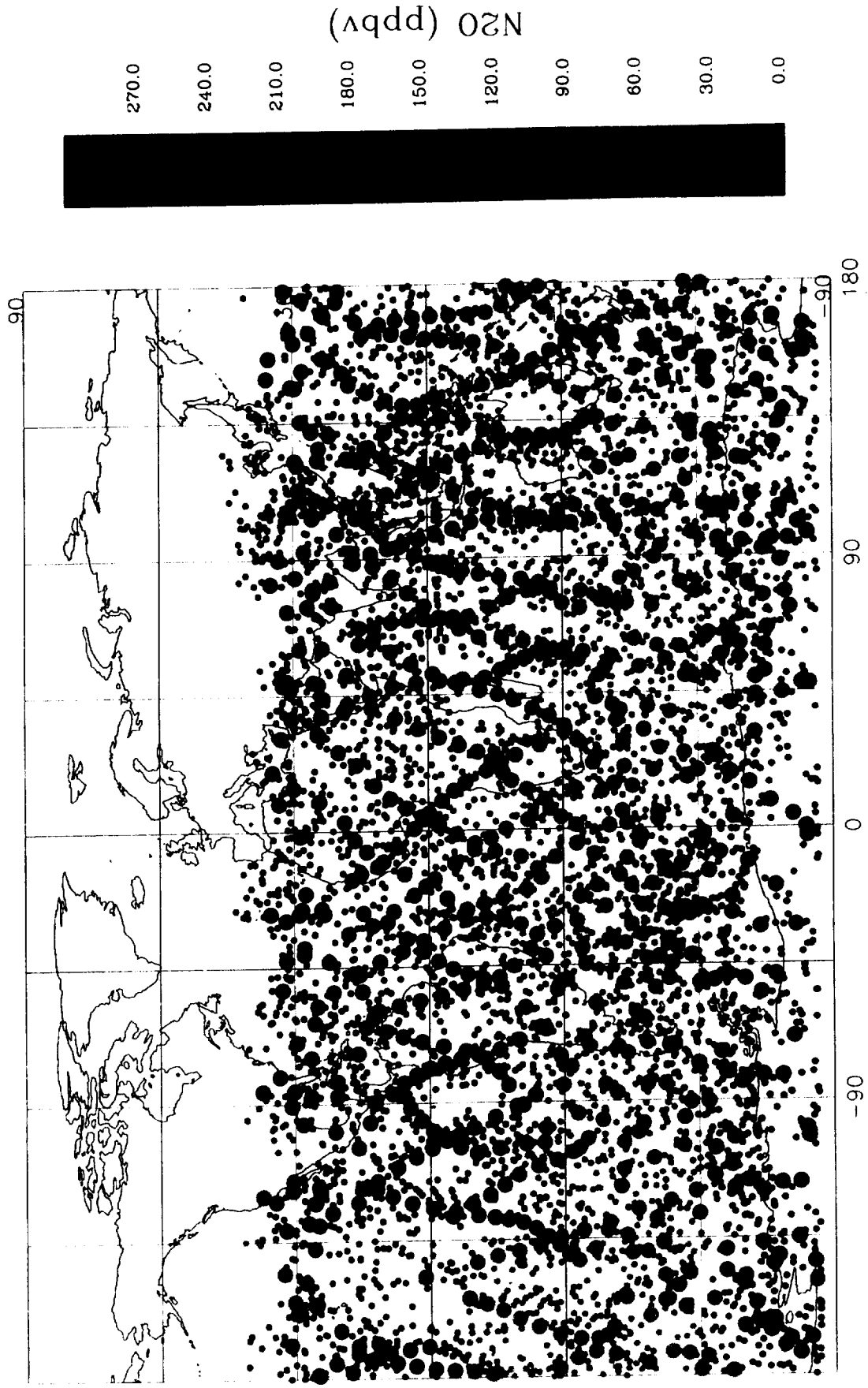


Figure VI.1b: Synoptic map of CLAES N₂O at 800K isentropic surface at 12UT on 09/09/92 from trajectory filling techniques using AER trajectory model. Data period is from 09/06/92 to 09/13/92.

Synoptic map of CLAES N₂O at 800K (09/09/92 at 1200UT) — Morris

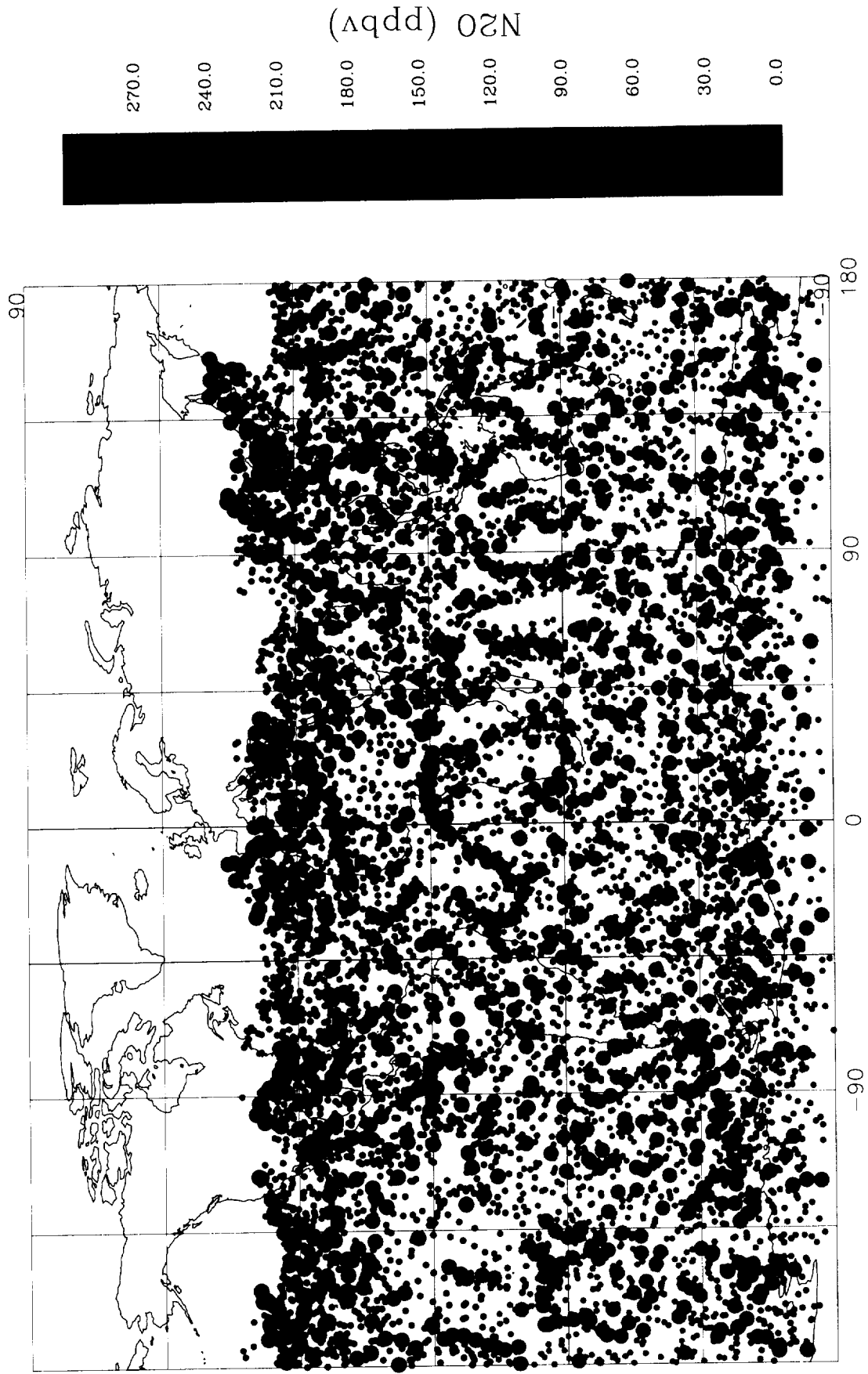


Figure VI.1c: Synoptic map of CLAES N₂O at 800K isentropic surface at 12UT on 09/09/92 using trajectory filling techniques from Morris et al. (1995). Data period is from 09/06/92 to 09/13/92.

Barnes--CLAES N₂O Trajectory Map at 800K (09/09/92 at 1200UT) (AER)
90

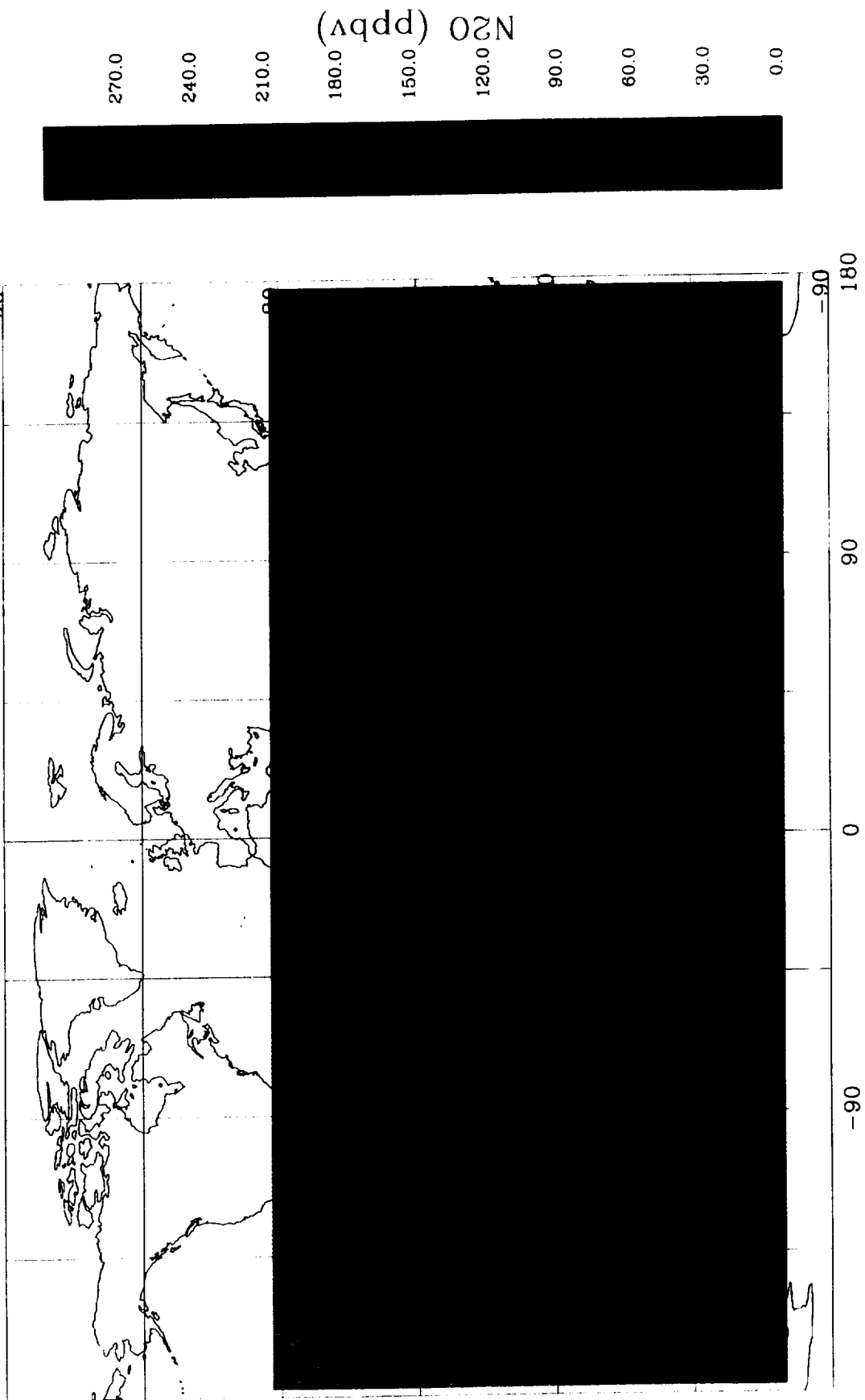


Figure VI.2: Gridded synoptic map of CLAES N₂O at 800 K isentropic surface at 12UT on 09/09/92 from AER. Barnes scheme is used to interpolated data to the gridded points. Data period is from 09/06/92 to 09/13/92.

NMC Ertel PV at 800K (09/09/92 at 00UT)

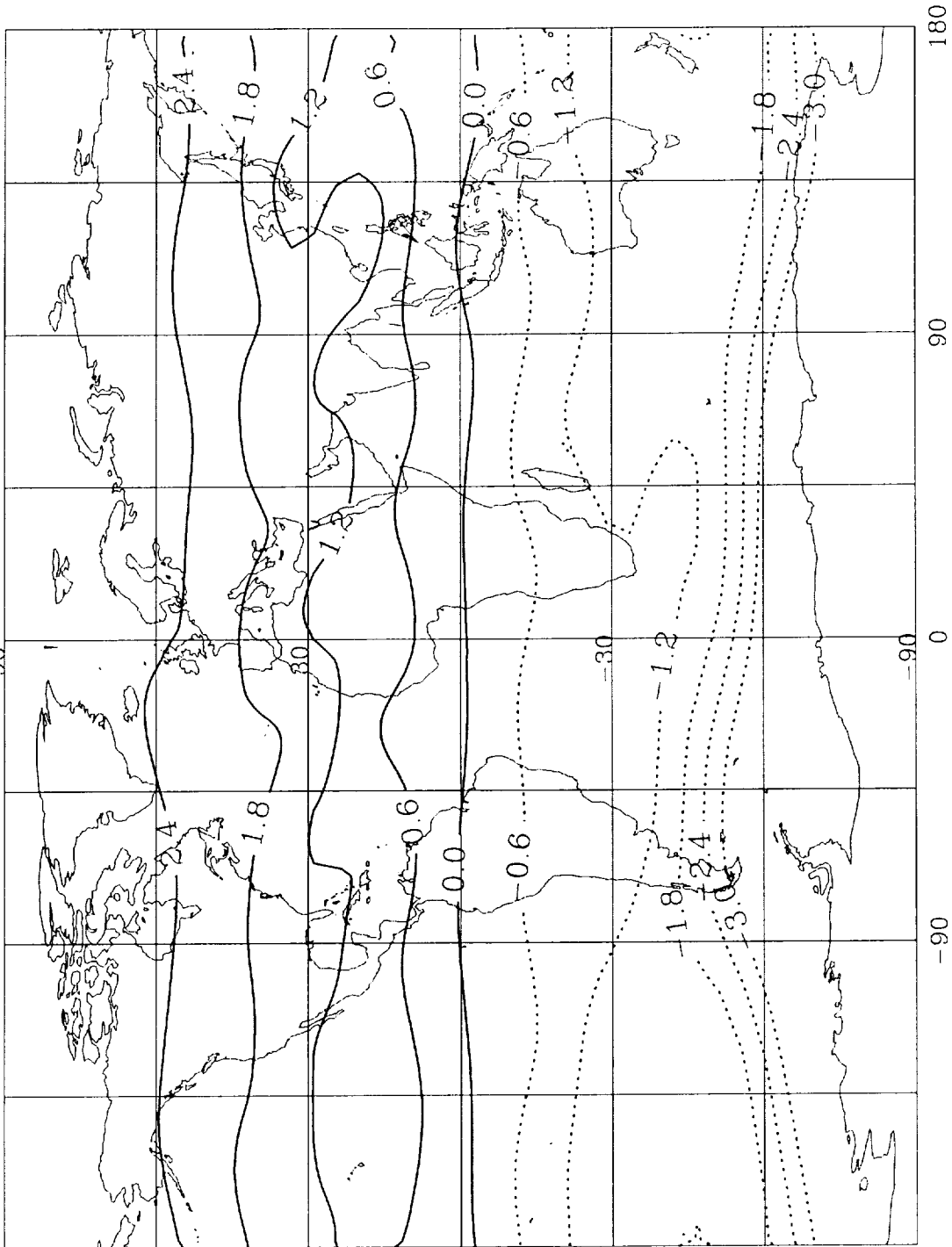


Figure VI.3: NMC Ertel PV in $10^{-4} \frac{K \times m^2}{kg \times s}$ at 800K at 00UT, 9/9/92.

MLS H₂O at 800K -- AER

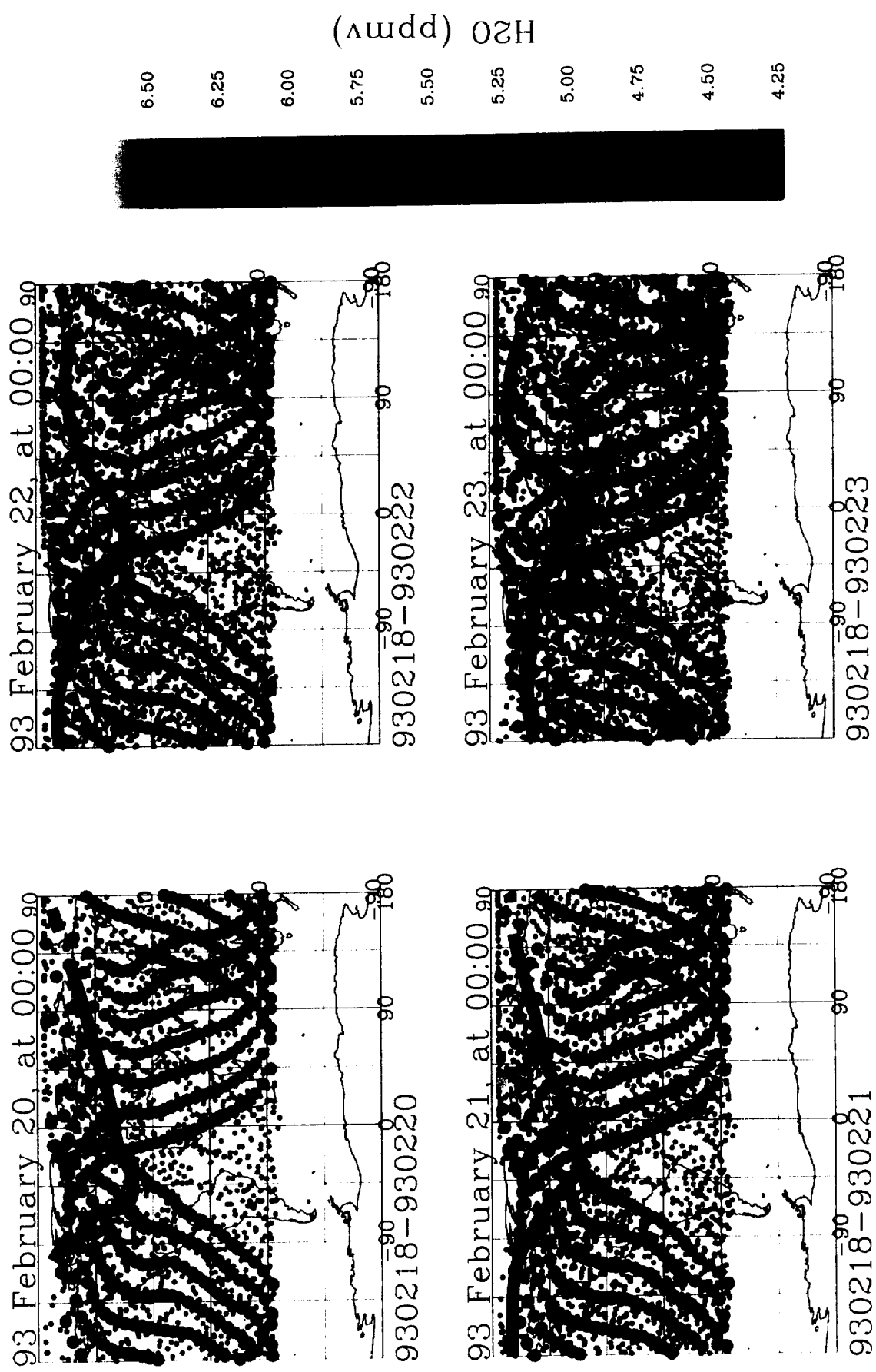


Figure VI.4a: Synoptic maps of MLS H₂O at 800 K isentropic surface from trajectory filling technique using AER trajectory model. Data period is from 02/20/92 to 02/23/92. The dark line is $3 \times 10^{-4} \frac{K \times m^2}{kg \times s}$ NMC PV contour.

MLS H₂O at 800K -- Morris

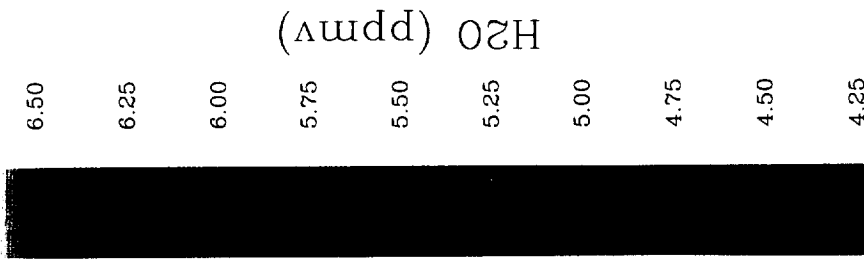
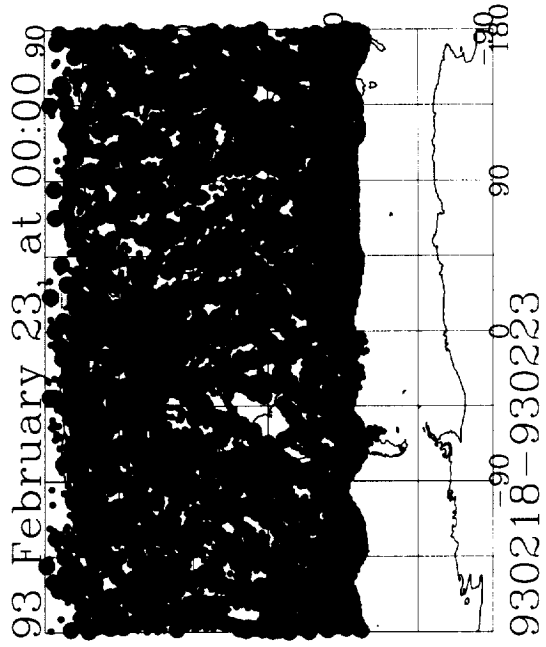
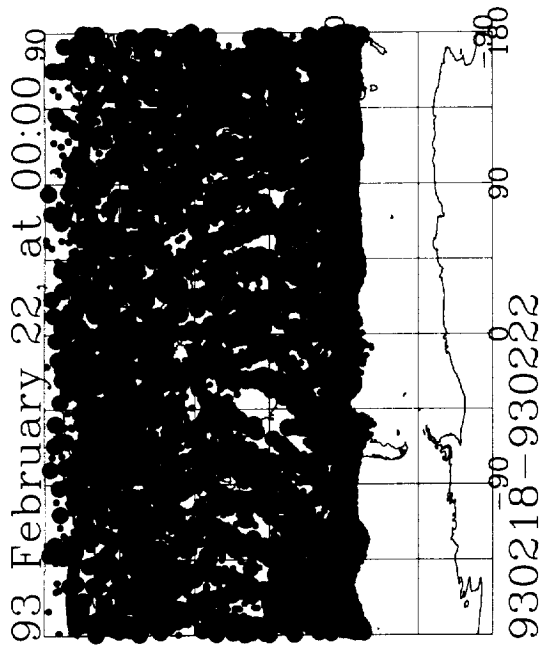
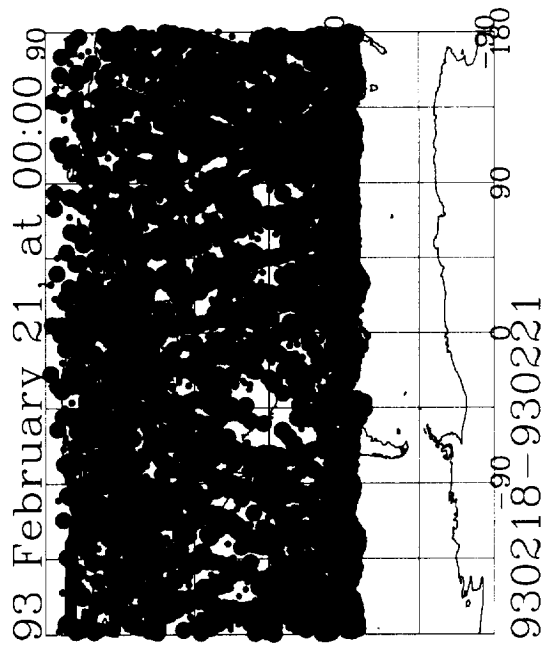
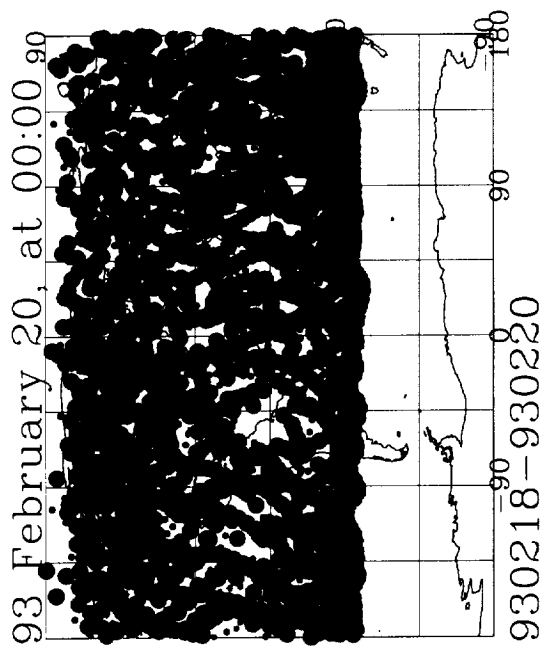


Figure VI.4b: Synoptic maps of MLS H₂O at 800K isentropic surface from Morris' trajectory model. Data period is from 02/20/92 to 02/23/92. The dark line is $3 \times 10^{-4} \frac{K \times m^2}{kg \times s}$ NMC PV contour.

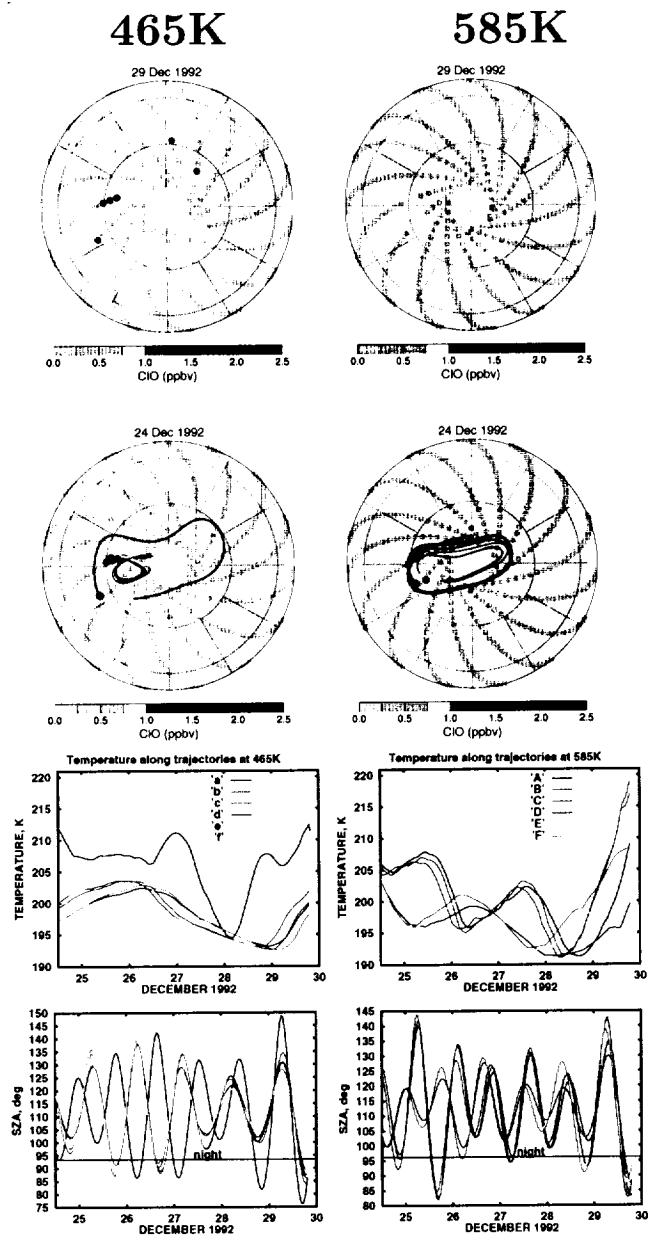


Figure VII.1: MLS v.4 ClO measurements (in ppbv) at 465 K (left column) and 585 K (right column) on Dec 29 (top row) and Dec 24, 1992 (second row). Six air parcels sampled twice are shown in the second row with thick dots (final points) corresponding to the locations of MLS measurements on Dec 29, 1992 showing high ClO content above Canada (red dots at 465 K and yellow dots at 585 K). Evolutions of temperature (third row) and SZA (low row) along these parcels are also shown by the same colors as the parcels.

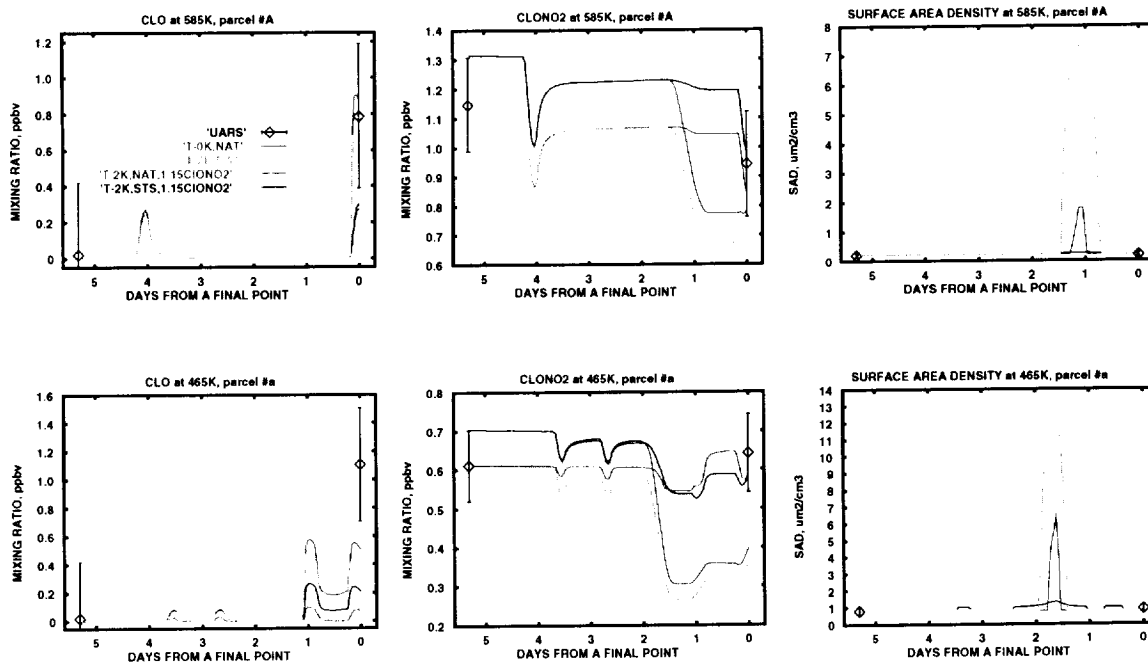
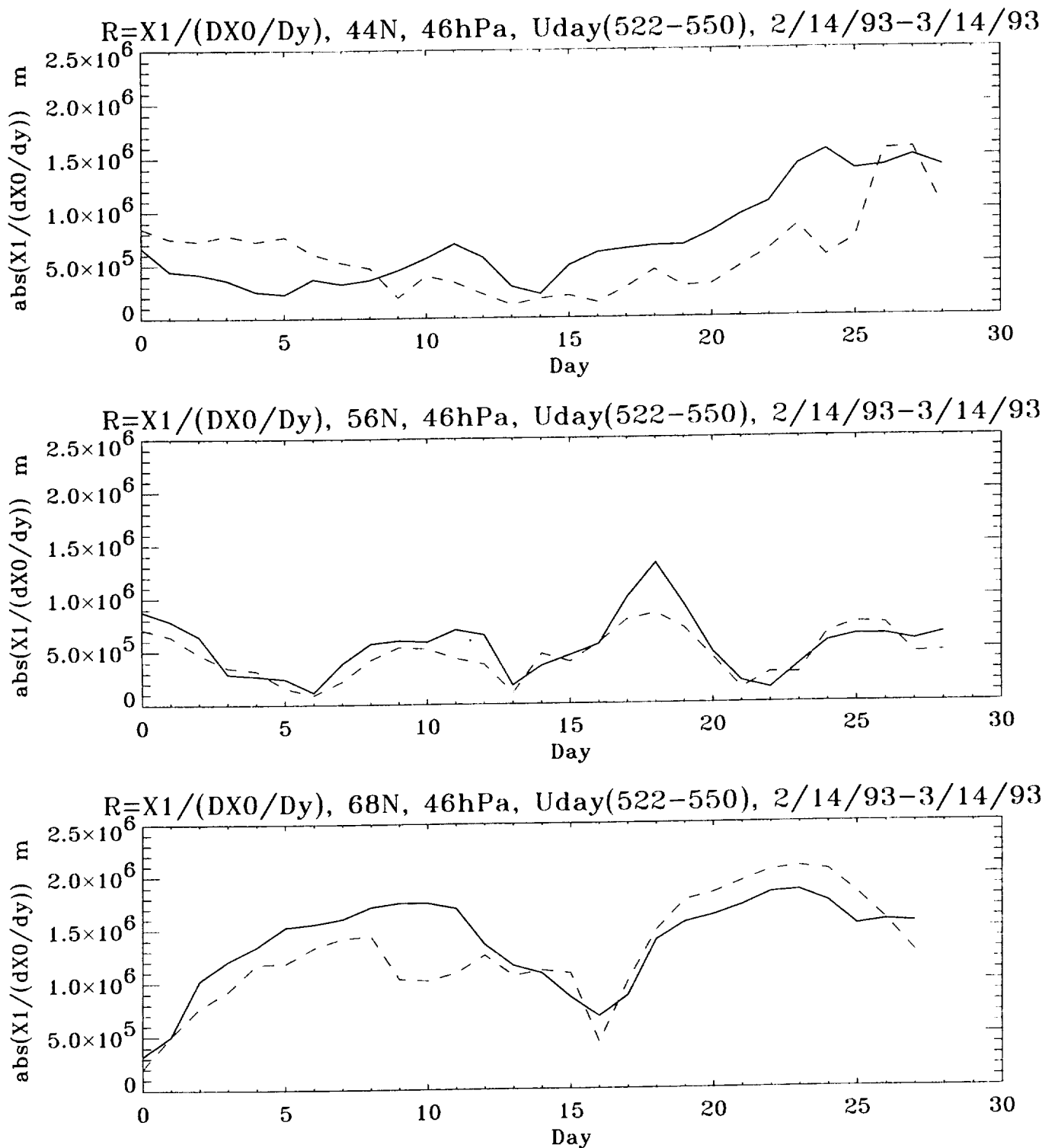
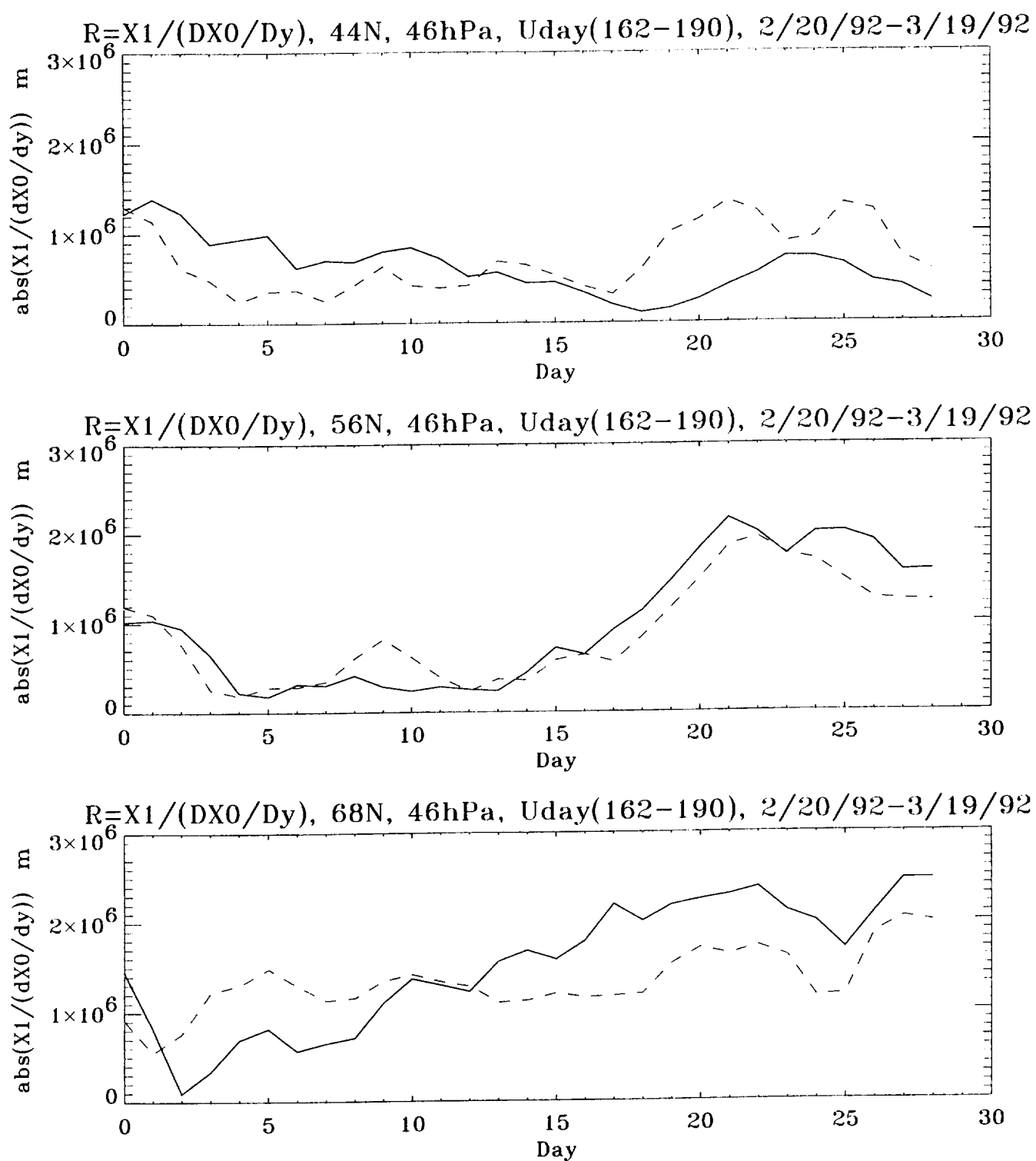


Figure VII.2: Comparison of MLS v.4 CIO and CLAES v.8 CIONO₂ and aerosol (converted from the 780 cm⁻¹ extinction to SAD) measurements (black symbols) at 465 K (bottom line) and 585 K (top line) with AER model calculations for the parcels #a and #A (i.e. shown by red lines in Figure 1). Blue lines: NAT scheme, UKMO temperature; grey lines: NAT scheme, UKMO temperature lowered by 2 K; green and red lines: UKMO temperature lowered by 2K, initial CIONO₂ equals to , NAT and STS schemes, respectively. The grey and green lines coincide at the SAD plot.



N₂O-Red CH₄-Blue

Figure VIII.1. Wave amplitudes of wave number 1 for N₂O and CH₄, at 46 hPa from Feb. 14 to Mar. 14, 1993, at (a) 44° N., (b) 56° N. and (c) 68° N. The plotted amplitudes are the values from UARS/CLAES 3B data divided by the corresponding latitudinal gradients (for N₂O or CH₄).



N2O-Red CH4-Blue

Figure VIII.2. Wave amplitudes of wave number 1 for N₂O and CH₄, at 46 hPa from Feb. 20 to Mar. 19, 1992, at (a) 44° N., (b) 56° N. and (c) 68° N. The plotted amplitudes are the values from UARS/CLAES 3B data divided by the corresponding latitudinal gradients (for N₂O or CH₄).

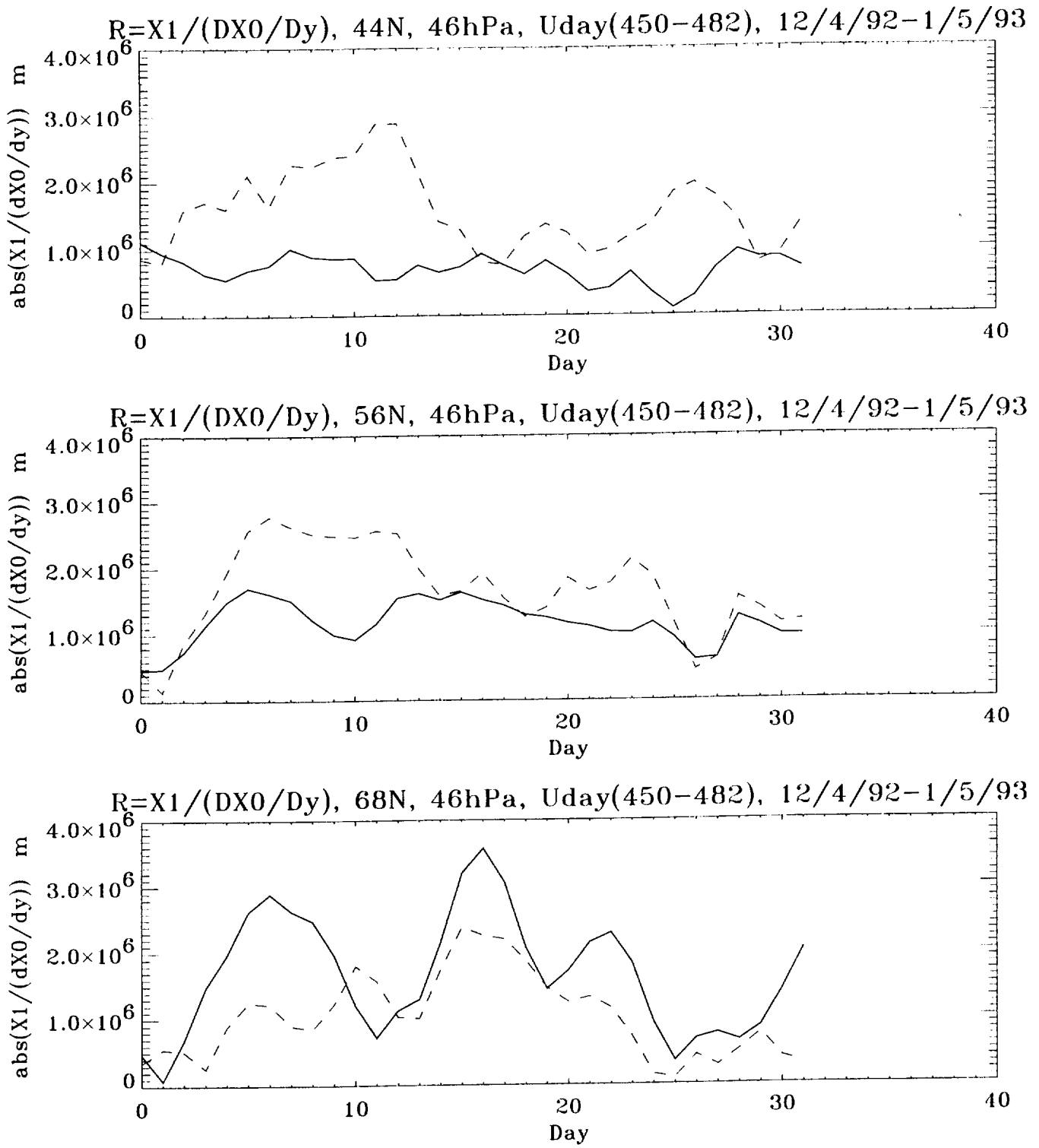


Figure VIII.3. Wave amplitudes of wave number 1 for N₂O and CH₄, at 46 hPa from Dec. 4, 1992 to January 5, 1993, at (a) 44° N., (b) 56° N. and (c) 68° N. The plotted amplitudes are the values from UARS/CLAES 3B data divided by the corresponding latitudinal gradients (for N₂O or CH₄).

